

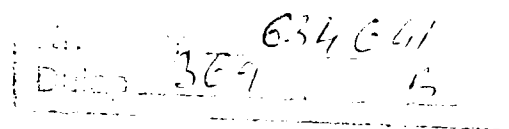
Nr. Inv.: **634.641**  
Dulap: **369** Lit: **B**

"POLITEHNICA" UNIVERSITY OF TIMIȘOARA  
MECHANICAL ENGINEERING FACULTY

Eng. **SEBASTIAN MUNTEAN**

**NUMERICAL METHODS FOR  
THE ANALYSIS OF THE THREE-DIMENSIONAL  
FLOW IN FRANCIS TURBINE RUNNERS**

**Doctoral thesis**



Prof. **IOAN ANTON**, rapporteur  
Prof. **FRANÇOIS AVELLAN**, corapporteur  
Prof. **VIORREL CÂMPIAN**, corapporteur  
Prof. **VLADIMIR CREȚU**, corapporteur  
Prof. **ROMEO SUSAN-RESIGA**, corapporteur

Timișoara  
**2002**



Knowledge of the fluid flow through the hydraulic passages of the turbomachines is the starting point in design, optimisation and operation processes. Since performing measurements inside the hydraulic machine, particularly for the runner, is a difficult task, we practically quantify only the global characteristics (i.e. cavitation and energetic performances). Although, these characteristics are useful for operation process, they provide few data for optimisation process.

For the past two decades, the numerical experiment has been increasingly used for computing the fluid flow in turbomachines. This was possible due to improved numerical algorithms and simulation techniques. As a result, the numerical simulation becomes able to fulfil two main objectives: computing the flow on the whole turbomachine (from the inlet to the outlet) and computing the three-dimensional turbulent flow.

The present thesis adheres to the modern trends of complementing (if not replacing) the physical experiment with numerical experiments in design and optimisation processes of the hydraulic turbines. The main topic is the computation of both energetic and cavitation performances for a Francis turbine runner for the whole operating range.

By its nature, the present thesis required a multidisciplinary approach, starting with a deep understanding of the physics of turbomachinery flow, then adding a solid knowledge of fluid mechanics, algorithms and numerical methods, modern computer programming techniques. In this endeavour, my efforts were encouraged and supported by the experience of several colleagues from the Hydraulic Machinery Department, National Center for Engineering of Systems with Complex Fluids, Computer Sciences Department from "Politehnica" University Timișoara and Center of Advance Research in Engineering Sciences from Romanian Academy – Timișoara Branch.

First at all I would like to express my warmest thanks to my magister, Professor Ioan Anton, for his invaluable ideas, advice and confidence in me during this research. It is hard to say in just a few words how much I have learned from his lifetime dedicated work on cavitation and hydraulic turbine research, but I am proud to consider myself among his disciples.

Many thanks are due to Professor Victor Ancușă, who was my first teacher on Fluid Mechanics and Viscous Fluid Mechanics. Our many hours of fruitful debates on turbomachine hydrodynamics disclosed many subtleties of the flow.

In particular I must thank Professor Romeo Susan-Resiga, who introduced me in the wonderful world of Computational Fluid Dynamics. His continuous support and guidance on understanding and using the numerical algorithms, as well as on using the appropriate numerical tools to get the best possible results given our computing capabilities, left a distinctive mark on each chapter of the thesis.

I would also like to thank Professor François Avellan for accepting to be a referee for my thesis. I am in debt to him and his research team for the experimental results I have used throughout the work to validate my numerical simulation. I am especially grateful to Dr. Eng. Gabriel Dan Ciocan for his invaluable help in gathering scientific papers and experimental data relevant for my work, as well as for his first hand advice on the experimental facility.

Finally, my parents Gheorghe and Eva Muntean deserve my deepest gratitude for their unselfish support and encouragement throughout my life.



## Table of Contents

1.	State of the art of the Turbomachinery Flow Research. Motivation of the Present Study.....	3
2.	Numerical Simulation of the Incompressible Flows.....	5
3.	GAMM Francis Turbine Test Case.....	9
4.	Numerical Simulation of the 3D Euler Incompressible Flow through GAMM Francis Turbine Distributor at the Best Efficiency Point (BEP).....	13
5.	Euler Numerical Simulation of the 3D Incompressible Flow through GAMM Francis turbine Runner at the Best Efficiency Point (BEP) .....	19
6.	Euler Numerical Simulation of the 3D Incompressible Flow through GAMM Francis Turbine Distributor at Off-Design Operating Conditions .....	31
7.	Euler Numerical Simulation of the 3D Incompressible Flow through GAMM Francis Turbine Runner at Off-Design Operating Conditions.....	37
8.	Theoretical Determination of the Energetic and Cavitation Characteristics for Francis Turbines .....	49
	Hydraulic efficiency .....	49
	Cavitation inception .....	51
9.	Conclusions .....	57
10.	Bibliography .....	59



## Chapter 1

## 1. State of the art of the Turbomachinery Flow Research. Motivation of the Present Study.

The successful development of efficient hydraulic turbomachines requires an understanding of flow conditions, which are exceedingly complex. Appreciation of this factor, together with a concerted effort to harness the flow efficiently, has offered one of the most exciting problems faced by any design engineer. In attempting to control the design parameters involved, many of which are as yet little understood, the design engineer requires both sophisticated software (for the prediction of flow processes) and hardware (for testing of components).

Fierce competition to produce more efficient and cheaper hydraulic machines has led to large technical advances in their major components and, in particular, the hydraulic turbines. The cost of manufacturing and testing these components in the development of new turbines and the improvement of existing units is one of the largest problems facing designers and manufacturers in today's market.

Therefore, the chief goal consists in development and validation of some methodologies (i.e. experimental or/and numerical), which will be very powerful engineering tools for design and optimization processes. The steady improvement in the speed of computers and the memory since the 1950s led to the emergence of *computational fluid dynamics (CFD)*. This branch of fluid dynamics complements both experimental and theoretical fluid dynamics. New improvements in computer hardware and numerical algorithms have also brought a reduction in resources required to perform numerical flow simulation.

The main topic of this thesis is to make some steps toward estimating the performances for a complete hydraulic machine. In this context it is evident that, when determining the performance of a Francis runner, the distributor has to be included in the flow calculation. The advantage of doing this is that the boundary conditions at inlet of the stay vane ring can easily be derived from the global corresponding to discharge and head. The flow field can be assumed to be constant over the cross section of stay vane inlet despite the variation of the flow velocities in the circumferential direction according to measurements. This peripheral variation of the flow field depends on the geometry of the spiral casing and leads to secondary unsteady effects on the runner.

Another point is worth to be considered. For industrial applications it is important to work as economically as possible. In terms of economics such a method has to be as accurate as necessary and as simple as possible.

The present work is logically divided in two parts. The first part, chapter one and two contains a brief review of computational methods for hydraulic turbomachineries and a description of the numerical simulation techniques. In the second part, chapter three presents the GAMM Francis turbine and chapters four to eight contain numerical flow analysis in a Francis turbine at best efficiency point and off-design operating conditions as well as computation of the energetic and cavitation performances. The conclusion of this work is presented in chapter nine. In addition, a brief outline of possible future extensions of this work is included.





## Chapter 2

## 2. Numerical Simulation of the Incompressible Flows

Computational fluid dynamics requires a multidisciplinary education of the engineer in conjunction with abilities to combine the coherent and efficient technical skills.

Generally, the numerical algorithm admitted today for technical problems comprises the following components: *phenomenon analysis* → *building the mathematical model (admitting the approximations level)* → *establishing the numerical scheme for discretizing the governing equations* → *implementation of the numerical algorithm* → *computation and analysis the numerical solution* → *validation and comparison against experimental data*. The simulation strategies and numerical techniques are coupled with the physical phenomenon. As a result, the numerical simulation still requires a high degree of user expertise.

Consequently, we propose a block approach that allows a more clear and flexible treatment of the numerical simulation. This block approach divides the numerical simulation in three modules, Figure 1:

*Pre-Processor* – first module contains the geometry and grid generation;

*Processor* – this module solves the problem, for that matter it includes the mathematical model together with the approximations level admitted as well as the numerical scheme established; the key ingredient here is the choice of appropriate boundary conditions, in agreement with the flow conditions;

*Post-Processor* - last module comprises the data visualization and results analysis;

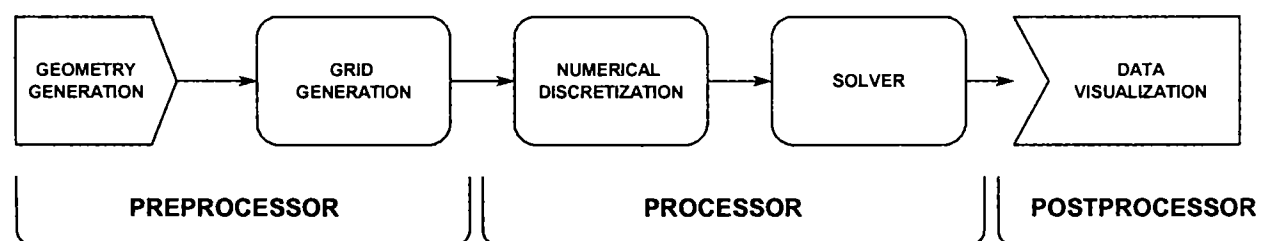


Figure 1. Numerical simulation block approach.

The first part of this chapter presents the main elements needed in building the mathematical model as well as the considerations for choosing the numerical scheme. Computational methods for hydraulic turbomachinery can be arranged according to the approximation level of the governing equations. This may include assumptions about spatial, dynamic and temporal characteristics of the solution.

The *spatial approximation* consists of replacing of the three variable (3D) used to describe the fluid flow with one variable (mono-dimensional flow 1D), two variables (bi-dimensional flow 2D, Vavra (1960)) or a combination (quasi-bi-dimensional Q2D and quasi-three-dimensional Q3D, Wu (1952), Wu (1959), Vavra (1960)). Developments in computer software and hardware made possible the computation of three-dimensional flows (3D) in turbomachines, Sottas & Ryhming (1993).

Computing the real flow (viscous and turbulent) through a hydraulic turbine still requires large computer memory and CPU time. As a result, a simplified simulation technique must be employed to obtain useful results for turbine design and/or analysis, using currently available computing resources. Based on the *dynamic approximation* different models can be considered: Reynolds Averaged Navier-Stokes equations (RANS), turbulence models, Thin Layer Navier-Stokes equations (TLNS), Parabolized Navier-Stokes equations (PNS), Euler equations (inviscid flow), irrotational flow and so on.

The turbomachine flow is essentially unsteady due to the rotor-stator interaction. Using the *temporal approximation* we compute the steady-state flow. On the other hand, rigorously speaking, the geometrical periodicity of the stator/rotor blade rows cannot be used since there are differences in flow from one interblade channel to another. However, with carefully chosen and experimentally validated assumptions, one can devise a methodology for computing the turbine flow, such that very good and engineering useful results are obtained. This thesis presents such some methodologies for computing the

three-dimensional, inviscid and steady-state flow through the Francis turbine and validates the numerical results with experimental data for the GAMM Francis turbine model, Sottas & Ryhming (1993), Parkinson (1995).

Currently, computational schemes based on the three-dimensional Euler equations are the most common design procedure. Two different mathematical methods are frequently used to solve the momentum and continuity equations based on coupling the velocity-pressure fields.

A possible way to determine the pressure field is the coupling of mass and momentum equations by the concept of artificial compressibility in analogy of the compressible flow, Rizzi & Eriksson (1984), Rizzi & Eriksson (1985). The *artificial compressibility method* (ACM) is used to solve for pressure with the additional assumption of steady flow. The original continuity equation is modified by adding an artificial time derivative of pressure representing the artificial compressibility, Chorin (1967). The pressure in a rigorous incompressible flow acts like a relaxation parameter to satisfy the continuity equation. Numerical results obtained with this method for steady incompressible flows through the Francis turbine were presented at a GAMM workshop in Lausanne in 1989, Sottas & Ryhming (1993).

An alternative way to solve the problem is formed by projection methods. In these methods first the pressure at the new level is estimated, for example by the old pressure, and then the momentum equations are solved yielding an intermediate velocity field. By projecting this velocity onto the space of divergence-free vector fields a new velocity and pressure may be computed. An important element of this class is the so-called *pressure-correction method* (PCM). This family include *Semi-Implicit Method for Pressure-Linked Equations* (SIMPLE) algorithm Patankar (1980), and its descendants (SIMPLER, SIMPLEC, SIMPLEST, PISO...), based on the segregation of momentum and continuity equations, Van Doormaal & Raithby (1984). In other words, the SIMPLE algorithm uses a relationship between velocity and pressure corrections to enforce mass conservation and to obtain the pressure field, Fletcher (1991), Ferziger & Peric (1996). A number of variants of the basic SIMPLE algorithm are available in FLUENT code, like SIMPLEC (SIMPLE-Consistent) algorithm and Pressure-Implicit with Splitting of Operators (PISO) algorithm, Fluent (1998).

The numerical scheme is determined by the mathematical and physical characteristics of the governing equations, Ferziger & Peric (1996), Hirsch (1988). An integral form of the governing equations is used by the finite volume technique, Fletcher (1991), Hirsch (1988). The basic principles of the finite volume are presented. The variables can be arranged in two ways on the grid. The choice of the staggered versus collocated arrangement depends on grid type. Staggered grids may be chosen because of their simplicity, but this arrangement requires, in general, orthogonal grid lines. Therefore, this approach may lead to unstable discretization. On collocated arrangement offers better accuracy but requires more memory. Nowadays, the collocated arrangement is preferred. The finite volume method consists of two steps: (1) interpolation is used to approximate the values on the cell faces and (2) integration of the governing equations on the individual control volumes to construct algebraic equations, Peric (1985), Fletcher (1991), Ferziger & Peric (1996), Hirsch (1988).

Next, the fundamental concepts about the computational domain generation and spatial discretization are discussed. Building the computational domain comprises the following stages: *establishing the typology of the computational domain* → *generating the 1D boundaries (curves)* → *generating the 2D boundaries (surfaces)* → *generating the computational domain*. Particularly, the turbomachines computational domains include a special type of boundaries called *foils* (in 2D) and *blades* (in 3D).

After a computational domain is built the spatial discretization is generated. The numerical solution accuracy and spatial discretization time depend on the choice of the mesh type (*structured, unstructured or hybrid*).

There is a large group of literature Thompson (1985), Soni (1985), Reymond (1992), Thompson (1996) and software Sorenson (1989), Soni (1992), Reymond (1995) which deals with structured meshing commonly referred to as "grid generation". Strictly speaking, a structured mesh can be recognized by all interior nodes of the mesh having an equal number of adjacent elements. For our purposes, the mesh generated by a structured grid generator is typically all quad or hexahedral. Algorithms employed generally involve complex iterative smoothing techniques that attempt to align elements with boundaries or physical domains. Where non-trivial boundaries are required, "block-structured" techniques can be employed which allow the user to break the domain up into topological blocks, Steinbrenner et. al. (1990). Structured grid generators are most commonly used within the CFD field, where strict alignment of elements can be required by the analysis code or necessary to capture physical phenomenon. Unstructured mesh generation, on the other hand, relaxes the node valence requirement, allowing any number of elements to meet at a single node, Weatherill (1996). Triangle and Tetrahedral meshes are

most commonly thought of when referring to unstructured meshing, although quadrilateral and hexahedral meshes can also be unstructured. While there is certainly some overlap between structured and unstructured mesh generation technologies, the main feature which distinguishes the two fields are the unique iterative smoothing algorithms employed by structured grid generators. Unstructured grids have the advantage of generality in that they can be made to conform to nearly any desired geometry. This generality, however, comes with a price. The grid generation process is not completely automatic and may require considerable user interaction to produce grids with acceptable degrees of local resolution while at the same time having a minimum of element distortion. Unstructured grids require more information to be stored and recovered than structured grids (e.g., the neighbor connectivity list), and changing element types and sizes can increase numerical approximation errors. However, mesh quality may be improved by local reconnection of elements (face and edge swapping) and by smoothing of point coordinates.

The main advantage of an unstructured mesh over the structured mesh is in the handling of complex geometrical domains. Because the 3D computational domains are strongly curved we employ unstructured meshes for Francis turbine parts (for distributor but specially the runner). Using the unstructured mesh we minimize the time for generating the spatial discretization which is a critical requirement.

Usually, the numerical simulation through the hydraulic machines involves the following boundary conditions: inflow velocity on the inlet section, outflow pressure on the outlet section, periodic velocity and pressure conditions on the periodical surfaces and zero normal velocity on the wall. When neither velocity nor pressure is known, special flow conditions may allow one to prescribe a relationship velocity-pressure as outflow condition. If this is not possible, then the computational domain must be extended up to a section where appropriate boundary conditions can be specified.

In conclusion, this chapter presents fundamental concepts and development of computational schemes for computing the fluid flow in hydraulic machines. This theoretical background supports the work developed in the following chapters.



### 3. GAMM Francis Turbine Test Case

The GAMM Francis turbine is an experimental model used for research work and it was designed at the *Institut de Machines Hydrauliques et de Mécanique des Fluides* (IMHEF) at the *École Polytechnique Fédérale de Lausanne* (EPFL). The test model corresponds to a Francis turbine of medium/high specific speed  $v=0.5$  ( $n_q=76$ ). The model was used as a test case back in 1989 GAMM Workshop, where all the geometrical information, including stay vanes, guide vanes, runner and draft tube, and measurements for the best efficiency operating point were available. The runner was also used as a test case in the annual ERCOFTAC Seminar and Workshop on Turbomachinery Flow Predictions.

A Piguet type spiral casing was designed to give a constant meridian velocity distribution. A fillet is added on both sides of the stay ring inlet in order to ensure well-defined inflow conditions. The stay ring consists of 24 stay vanes and the distributor of 24 guide vanes. The runner has 13 blades and has an external diameter of 0.4 m.

Flow surveys were conducted at both inlet and outlet sections of the runner for various operating conditions, as well as on the distributor inlet section and draft tube inlet section. Pressure transducers installed on both pressure and suction sides of the runner blades provide the pressure distribution on the blade. Flow measurements were obtained with a 5-hole pressure probe. Runner static pressure was measured at three different blade sections. Full description of the measurements is available in Sottas & Ryhming (1993) and Parkinson (1995). The four flow surveys axes are presented in Figure 2.

A detailed presentation of the test case Francis turbine geometry and of the flow survey performed at IMHEF are given in Proceedings of the GAMM Workshop entitled "3D-Computation of Incompressible Internal Flows" held at Lausanne in 1989, Sottas & Ryhming (1993).

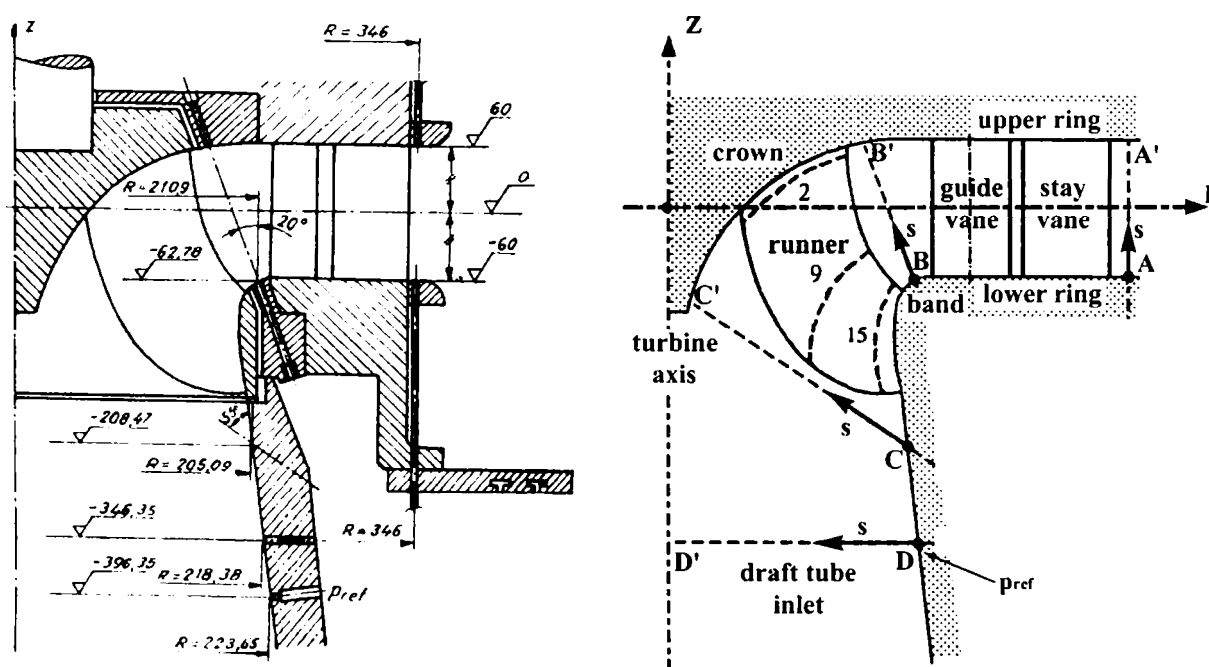


Figure 2. GAMM Francis turbine model, Sottas & Ryhming (1993).

Figure 2 shows the turbine meridian view with the actual main dimensions. The four survey axes used to investigate the velocity and pressure fields are shown in the right picture. The first axis, AA' corresponds to the distributor inlet (spiral case outlet). The BB' axis conventionally marks the distributor outlet and runner inlet. The next survey axis CC' is located right after the runner blades. Only velocity data are available on this axis. The last survey axis DD' conventionally marks the draft tube inlet.

For the GAMM workshop, detailed measurements at the best efficiency point (BEP) (discharge coefficient  $\phi=0.286$ , energy coefficient  $\psi=1.07$ , and efficiency  $\eta=0.92$ ) were available. The database

comprised integral properties of the flow; such as torque coefficient  $t=0.25577$  and global volume flow rate  $Q=0.372 \text{ m}^3/\text{s}$ . The pressure and velocity distribution measurements were made at the inlet of the distributor, at the inlet of the runner, just after the runner blades, at the inlet of the draft tube and at the outlet of the draft tube. The runner blade has been equipped with 28 pressure transducers (17 on the suction side and 11 on the pressure side) arranged along the "streamlines" S2, S9 and S15, Parkinson (1995), as shown in Figure 3. The pressure on the blade was measured because it is relevant for evaluating the cavitation behaviour.

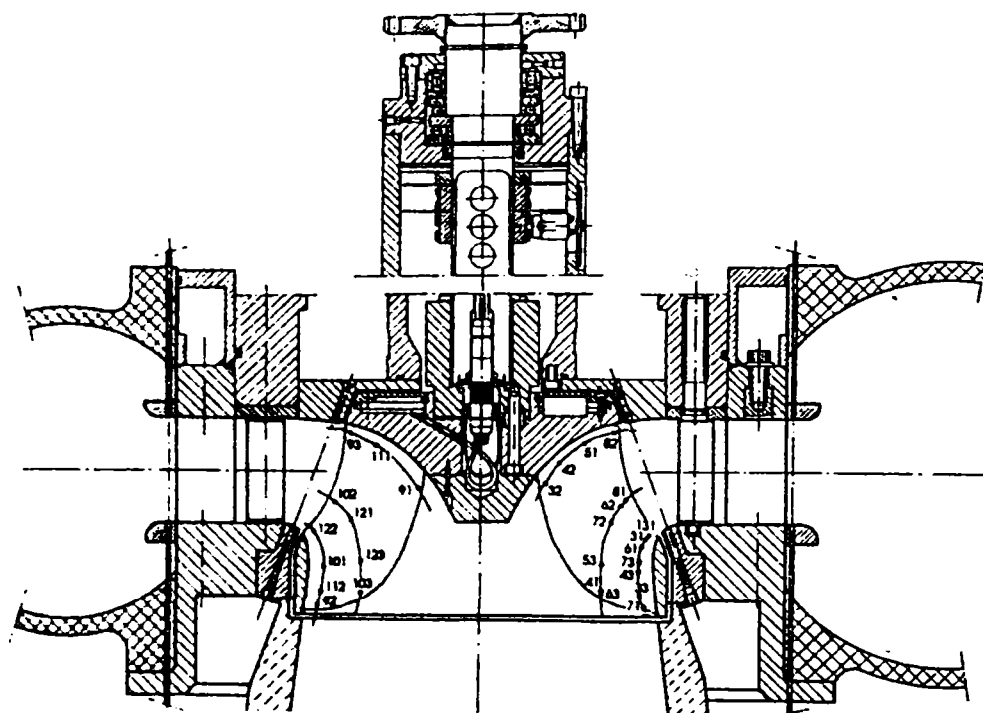


Figure 3. Instrumented runner for GAMM Francis turbine, Sottas & Ryhming (1993).

Figure 4 shows the measured hill charts for the GAMM Francis turbine. Figure 4 top corresponds to the standard IEC procedure, i.e. by taking into consideration the draft tube as well. Because of the poor draft tube design and performance, there are two peaks of maximum efficiency. As a result, a new hill chart was computed by considering the outflow section at the draft tube inlet, Figure 4 bottom. This particular hill chart has a single maximum efficiency point, 2% higher than the standard hill chart. The difference in efficiency between the two hill charts allows one to estimate the draft tube efficiency.



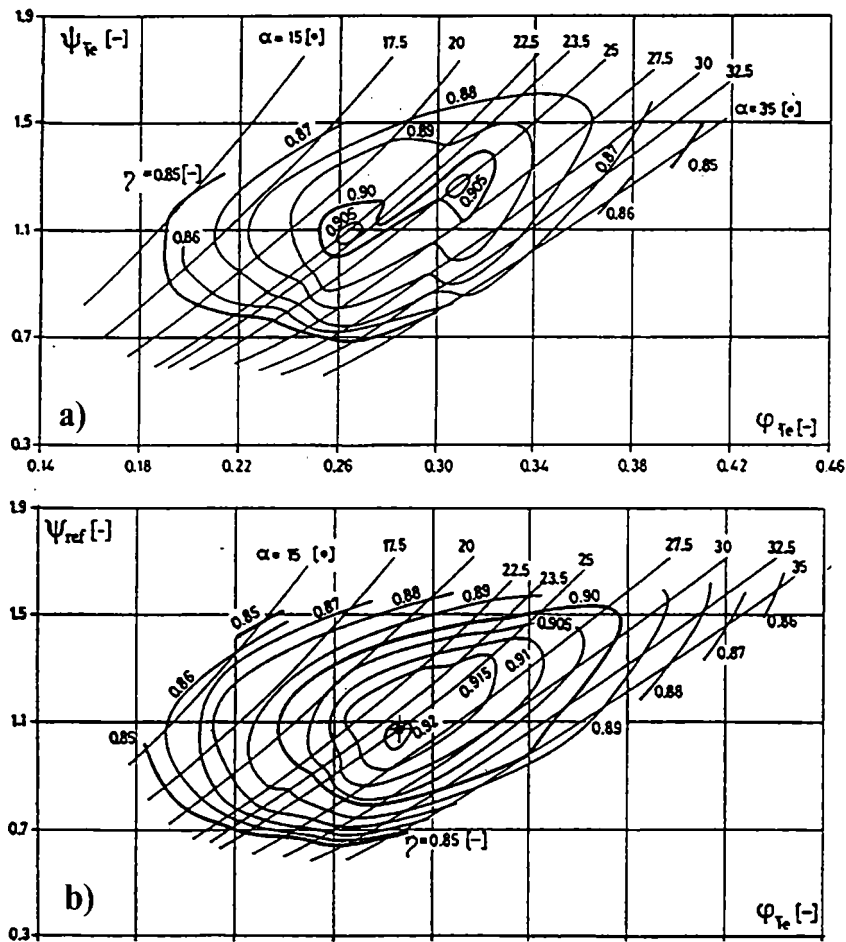


Figure 4. Standard and modified reference hill charts for GAMM Francis turbine, Sottas & Ryhming (1993).

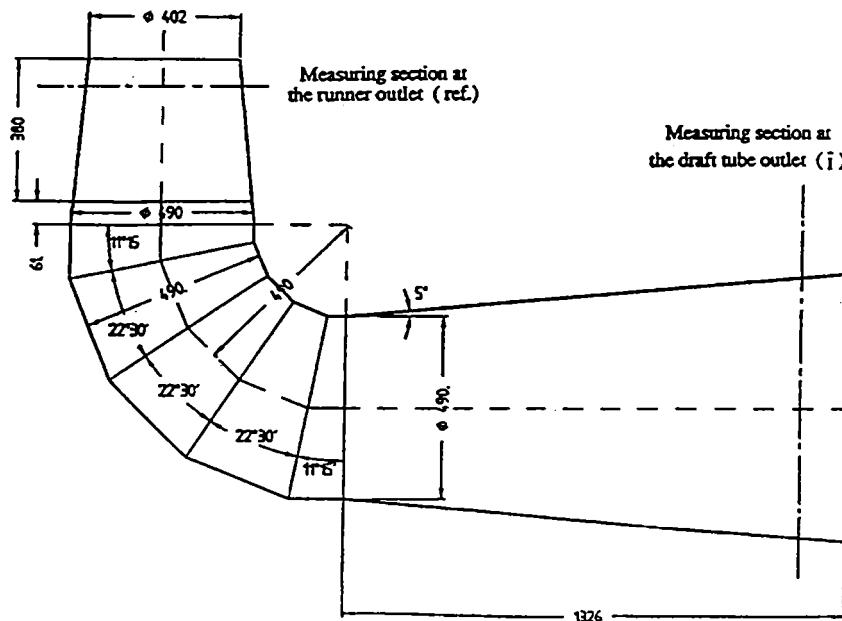


Figure 5. Draft tube geometry of GAMM Francis turbine, Sottas & Ryhming (1993).

Figure 5 shows the actual design of the GAMM turbine draft tube. The draft tube geometry is used in the present work to compute its efficiency using the Figure 4 hill charts, but we are not investigating the draft tube flow. Instead, we are employing the Kubota et al. (1996) theory to evaluate the draft tube hydraulic loss coefficient, and further to compute the turbine cavitation coefficient.





## Chapter 4

#### 4. Numerical Simulation of the 3D Euler Incompressible Flow through GAMM Francis Turbine Distributor at the Best Efficiency Point (BEP)

This chapter presents the methodology employed for computing the three-dimensional flow in the turbine distributor. First we define the 3D computational domain and its discretization, then we discuss the boundary conditions and present three sets of conditions further used in computations. Finally, we compare our numerical results against experimental data and other numerical results from literature. The best results are obtained for the **D2** (see below) boundary conditions set; only these results are presented here.

The flow is assumed to be cyclic around the distributor in steady-state conditions, so that the computational domain contains only one blade passage. Accordingly, the distributor blades (stay vanes and guide vanes) are enclosed in the computational domain and periodical surfaces delimit the blade passage, Figure 6. The inflow/outflow sections for the distributor domain are revolution surfaces generated by the AA' and BB' axes, and the upper/lower rings, respectively.

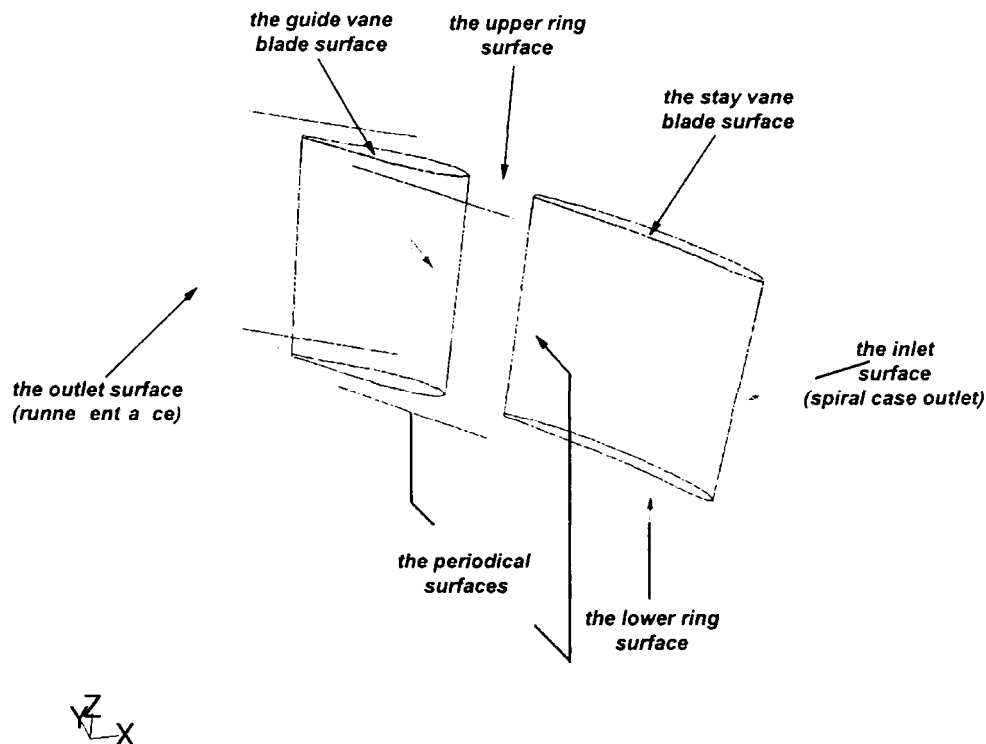


Figure 6. Three-dimensional computational domain for the Francis turbine distributor.

The three-dimensional domain of the GAMM Francis turbine distributor is discretized using an unstructured mesh with tetrahedral cells, Figure 7. The mesh has been generated using the FLUENT pre-processor, Gambit (1998).

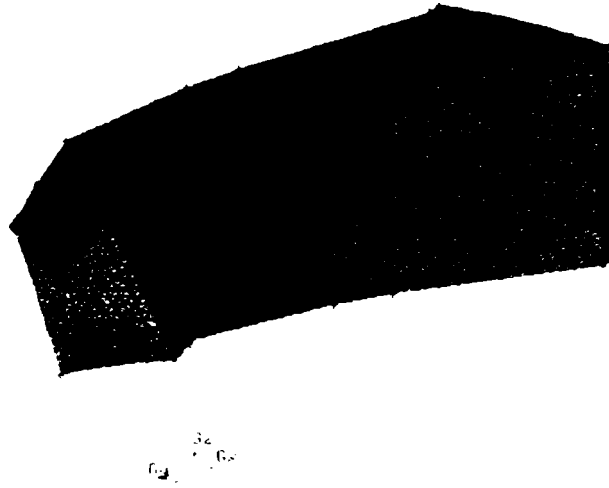


Figure 7. Unstructured mesh for Francis turbine distributor domain. (60892 cells, 14514 nodes)

Several options have been considered for specifying the boundary conditions:

- **velocity field** is prescribed on *the inflow section*;
  - *uniform velocity distribution*: The advantage of imposing the boundary conditions at the stay vane inlet is that it can be easily derived from the global data corresponding to the water flow rate. The flow field is considered to be constant over the whole cylindrical distributor inlet section, corresponding to an ideal spiral casing. As a result, the distributor inlet velocity components are computed such that the correct discharge value ( $Q=0.372 \text{ m}^3/\text{s}$ ) is preserved and the flow angle ( $\gamma^{\text{sv}}=34^\circ$ ), Goede (1993) corresponds to the stay vane incidence;
  - *measured velocity distribution*: Data corresponding to the flow survey at the stay ring inlet is measured at three angular positions of the probe axis  $\theta^{\text{sv}} = 175^\circ, 265^\circ$  and  $355^\circ$ , respectively. These detailed measurements at the stay ring inlet show non-uniformities in the flow conditions around the circumference at the inlet of the distributor. These non-uniformities are undoubtedly caused by an imperfect design of the spiral casing and cause a series of problems related to proper definition of flow conditions at the entrance of the distributor for calculation, Sottas & Ryhming (1993). In this case, the boundary condition on the distributor inlet surface consists of experimental flow field at the angular position  $\theta^{\text{sv}} = 265^\circ$  together with periodical assumption;
- **pressure distribution** is imposed on *the outlet section*;
  - *constant pressure distribution*: The constant pressure repartition is considered only as a first guess for numerical computation. The numerical value represents the arithmetical mean value,  $p_{\text{med}}=133460 \text{ Pa}$  ( $c_{p, \text{med}}=0.67$ ) computed with experimental data. We mention once again that this value is unknown a priori;
  - *measured pressure distribution*: Using this condition we impose the measured pressure distribution, Sottas & Ryhming (1993);
- **periodic conditions** are imposed on *the periodic boundaries*:
 
$$\vec{V}(r, \theta, z) = \vec{V}\left(r, \theta + \frac{2\pi}{Z}, z\right) \text{ si } p(r, \theta, z) = p\left(r, \theta + \frac{2\pi}{Z}, z\right)$$
- **wall conditions** (i.e. zero normal velocity) are imposed on the *stay and guide blades*, as well as on the distributor *upper and lower rings*, respectively.

Three different series of computations have been performed for the GAMM Francis distributor:

- first computation, denoted **D1**, consists in prescribing the uniform velocity distribution on the inflow section and the constant pressure distribution on the distributor outflow section;
- second calculation, labelled **D2**, is different with respect to the first case by prescribing the measured pressure distribution on the outflow section;
- last computation, marked **D3**, uses the measured velocity distribution on the inflow section and the measured pressure on the distributor outflow surface.

The inviscid and incompressible flow (Euler model) is computed using the FLUENT 5.7 code. The following figures present the comparison of computed velocity component profiles, flow angle and pressure distribution against the measurement data for GAMM Francis distributor at the best efficiency point. The velocity components are normalized with  $(\sqrt{2E})$  and the angles are given in degree. The dots represent measured values while the lines are numerical results. The normalized abscissa,  $s$ , is defined as the distance from the band along the measurement axis, normalized by the reference radius  $R_{ref}$ . The following dimensionless quantities are employed in the present work:

$$c_r = v_r / \sqrt{2E} \text{ - normalized absolute radial velocity}$$

$$c_u = v_u / \sqrt{2E} \text{ - normalized absolute tangential velocity}$$

$$c_z = v_z / \sqrt{2E} \text{ - normalized absolute axial velocity}$$

$$c_p = (p - p_{ref}) / (\rho E) \text{ - normalized pressure coefficient}$$

$$\alpha = \arctg\left(\frac{c_m}{c_u}\right) \text{ - absolute flow angle}$$

This abstract presents only numerical results for the **D2** set of boundary conditions, i.e. constant inlet velocity components and measured outlet pressure.

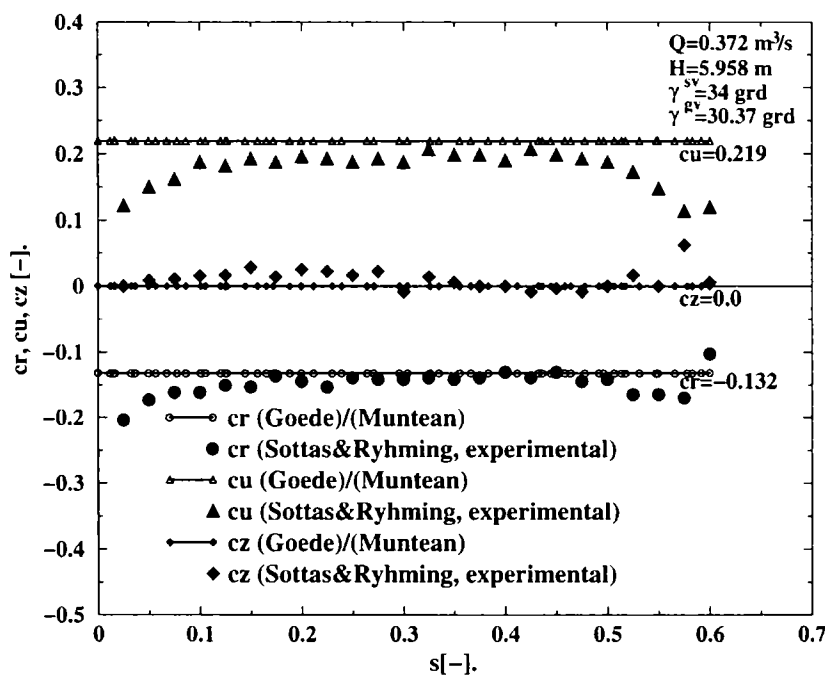


Figure 8. Velocity components on the distributor inlet axis AA'. Imposed values and comparison with the experimental data Sottas & Ryhming (1993), Muntean (D2 case —) and Goede (1993) (---).

The velocity field on the distributor inlet section is presented in Figure 8. Constant velocity profiles are considered for numerical simulation, although viscous effects and spiral case design leads to a certain variation near the upper/lower rings. The velocity component values, see Figure 8, were chosen such that  $c_r$  insures the global discharge measured value,  $c_z=0$  insures a plane flow and  $c_u$  corresponds to the ideal flow angle of attack on the stay vane. No circumferential variation of the velocity is assumed. These conditions are met by an ideal spiral case. The same inlet conditions were used by Goede and other groups.

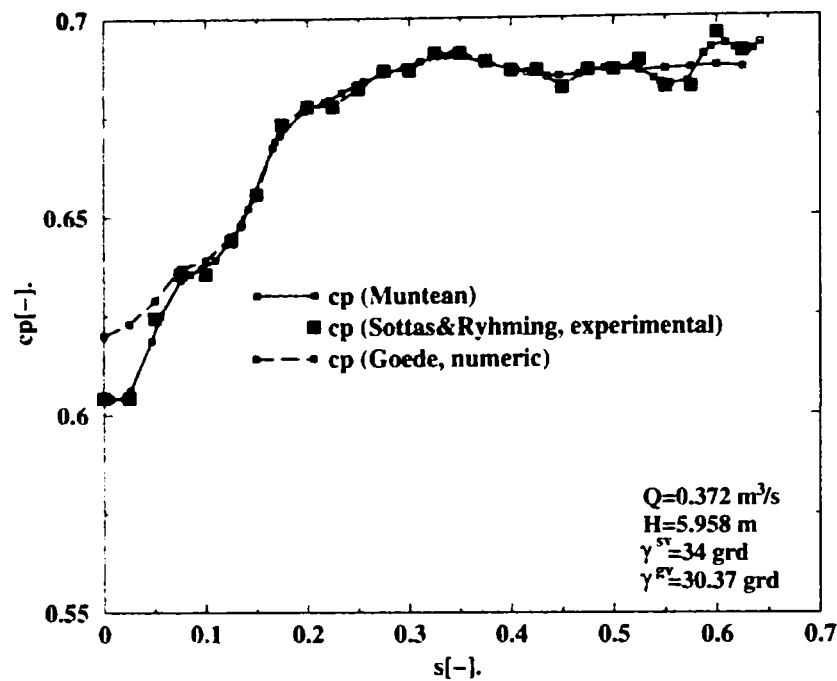


Figure 9. Pressure coefficient on the distributor outlet axis BB'. Comparison between the experimental data Sottas & Ryhming (1993), imposed value Muntean (D2 case ———) and computed results Goede (1993) (-----).

Figure 9 presents the measured pressure distribution prescribed on the distributor outlet axis BB'. Our boundary condition exactly follows the experimental points, and it is very close to the computed pressure distribution obtained by Goede.

The computed pressure coefficient on the distributor inlet axis AA' is shown in Figure 10. The pressure distribution practically matches the experimental data. However, one would expect that the inviscid flow model predicts a slightly smaller numerical value, since the hydraulic losses are not taken into account.

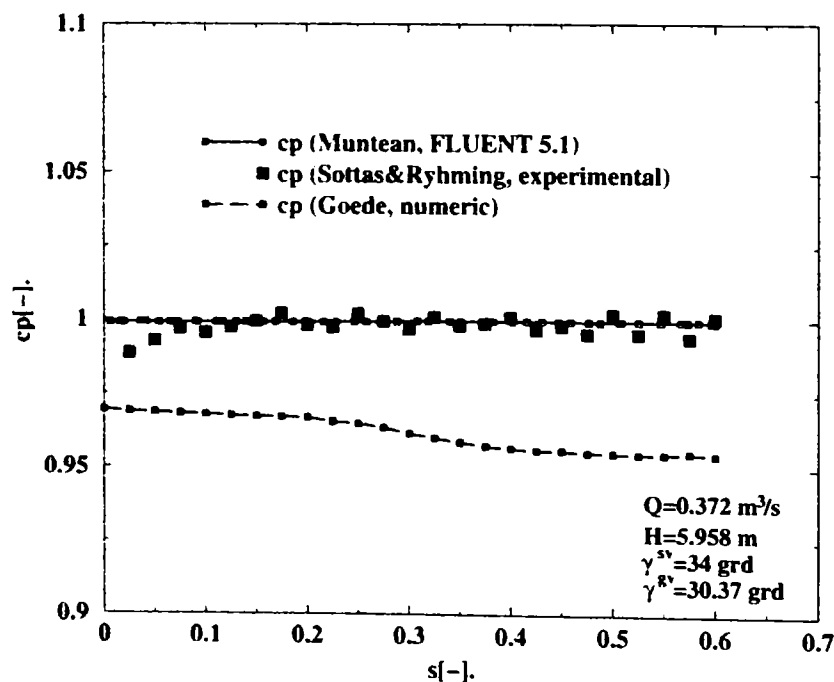


Figure 10. Pressure coefficient on the distributor inlet AA'. Comparison between the experimental data Sottas & Ryhming (1993) and computed results, Muntean (D2 case ———) and Goede (1993) (-----).

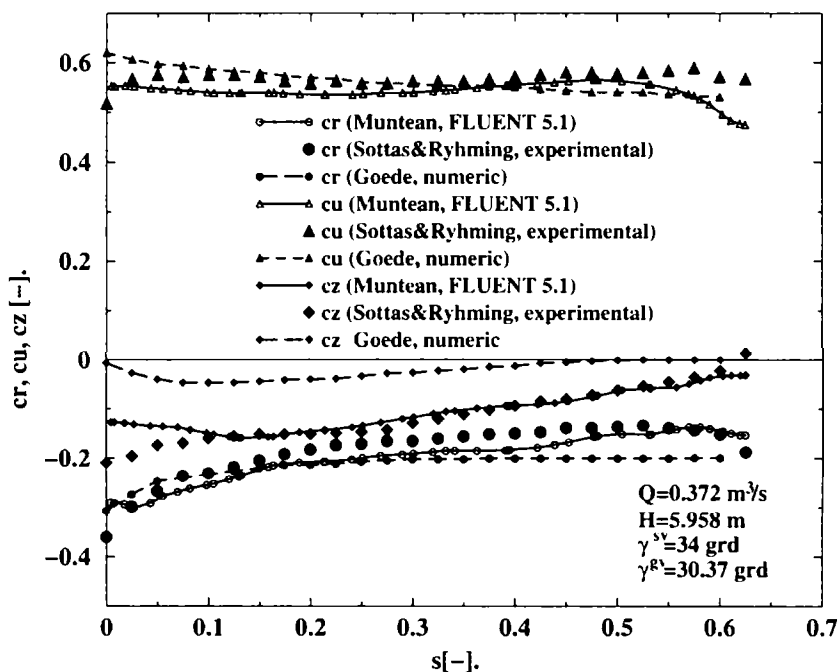


Figure 11. Velocity components on the distributor outlet axis **BB'**. Comparison between the experimental data Sottas & Ryhming (1993) and computed results, Muntean (D2 case —) and Goede (1993) (-----).

Figure 11 shows the velocity profile computed on the outlet axis **BB'**. A very good agreement between our numerical results and experimental data is obtained except the upper/lower ring neighborhood. We appreciate that our results are more accurate compared to Goede's numerical results. The radial velocity coefficient agrees with the experiment along the whole survey axis, with our results displaying a slightly larger magnitude. One can see that Goede's  $c_r$  magnitude is larger by 25% in the upper ring neighbourhood (large  $s$ ). As far as the axial velocity coefficient is concerned, we obtain an excellent agreement with the measured values for  $s > 0.15$ . The departure of our  $c_z$  values from experiment for  $s < 0.15$  (i.e. the lower ring neighborhood) can be explained by the abrupt flow turning in this region. Note that Goede's  $c_z$  magnitude is much smaller than experimental data on the whole **BB'** survey axis. Our tangential velocity coefficient  $c_u$  displays the same variation on the survey axis as the experimental data, while Goede's numerical results monotonically decrease from the upper to the lower ring. However, our numerical results predict a smaller  $c_u$  value near the upper ring.

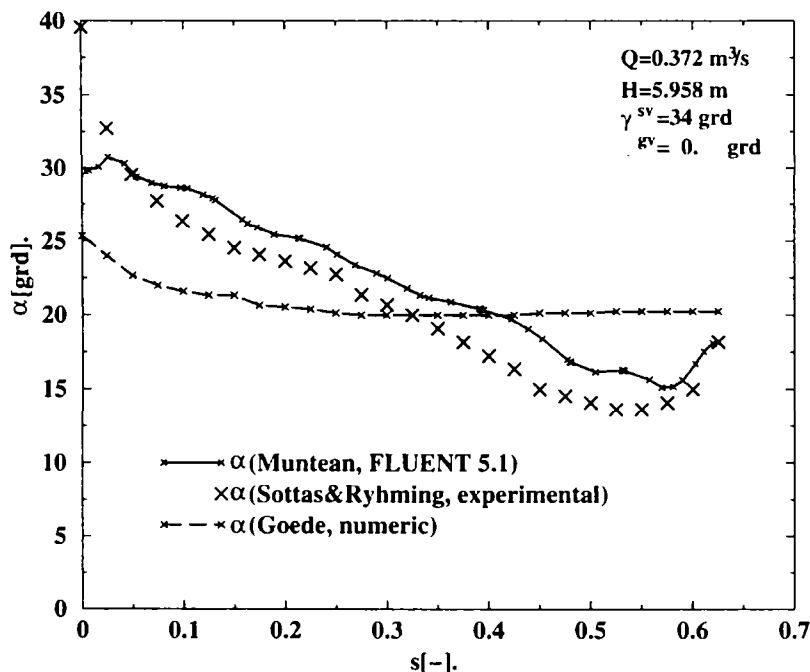


Figure 12. Flow angle on the distributor outlet axis **BB'**. Comparison between the experimental data Sottas & Ryhming (1993) and computed results, Muntean (D2 case —) and Goede (1993) (-----).

Probably more important than predicting the individual velocity components distribution on the BB' survey axis is the flow angle  $\alpha$  at the runner inflow, presented in Figure 12. Our computed values are slightly larger than experimental data, but have the correct behavior from lower to upper ring. In contrast, Goede's results fail to predict the actual flow direction. Naturally, the following question arises: why is the inviscid absolute angle flow larger than the viscous absolute angle flow? In a previous study we have shown that, when taking into account the viscous effects, the viscous flow displays a detachment on the blade suction side, Figure 13. As a result, the viscous flow turning angle is smaller than its inviscid counterpart and this is the reason why our inviscid model predicts an angle larger with 2 degrees (on average) than the real values.

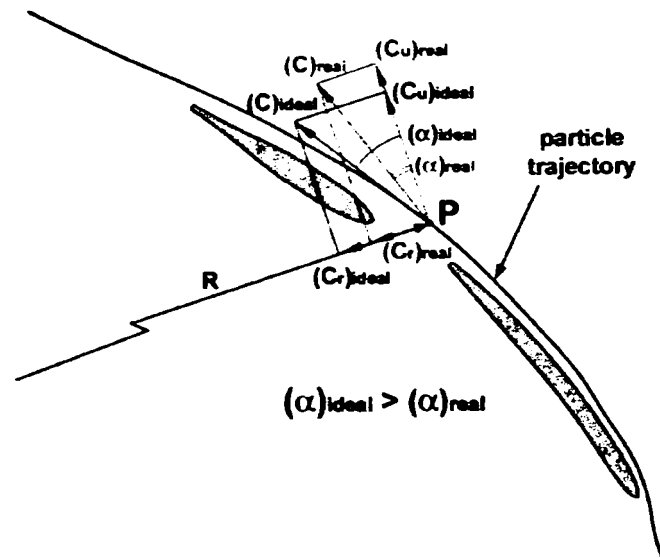


Figure 13. Inviscid versus viscous absolute angle flow.

In conclusion, this chapter presents a methodology for computing the three-dimensional inviscid, incompressible flow in the Francis turbine distributor. The 3D computational domain corresponds to the actual turbine geometry, and an unstructured discretization (tetrahedral) is employed. The investigation is focused on the inflow/outflow boundary conditions. It is shown that for practical applications one can assume constant velocity components on the inflow section, with zero axial velocity. However, it is important that the radial component preserve the correct discharge, while the tangential component preserve the correct angle of attack on the stay vanes. On the other hand, the outflow pressure distribution should match the experimental data in order to obtain the correct overall velocity and pressure fields. As a result, even when the flow is considered inviscid, the computed inlet pressure and outlet velocity agree reasonable well with experimental data. More important, the flow direction at the runner inlet is predicted correctly, but with a slightly larger turning angle ( $2^\circ$  on average) due to the lack of viscous effects. The present results correspond to the best efficiency operating point.

## Chapter 5

## 5. Euler Numerical Simulation of the 3D Incompressible Flow through GAMM Francis turbine Runner at the Best Efficiency Point (BEP)

The fifth chapter presents the methodology developed for computing the three-dimensional flow in the Francis turbine runner. First, we define the 3D computational domain and its discretization, then we discuss the boundary conditions and present three sets of conditions further used in computations. Second, we compare our numerical results against experimental data and other numerical results from literature. The best results are obtained for the {1} (see below) set of boundary conditions. Finally, the numerical global parameters (e.g. runner torque coefficient) are computed and checked against experimental values.

The runner relative flow is assumed to be steady and cyclic around the runner, therefore we consider only one blade passage for the computational domain. Consequently, the runner blade is enclosed in the computational domain and periodical surfaces bound the blade passage. The runner blade geometry was defined using 17 sections, Figure 14. The ERCOFTAC runner blade description with a blunt trailing edge is used for the computations in this work. Detailed geometry files for the runner are available from the ERCOFTAC workshop.

The runner computational domain begins with the conical surface generated by the BB' axis and ends with the disc of radius DD', Figure 15. The BB' axis conventionally marks the runner inlet whilst the DD' axis corresponds to the draft tube inlet (the outlet section of the runner computational domain). This choice was motivated here by the availability of experimental data, Figure 2. The chief difficulty of the runner computational domain consists in building the strong curved three-dimensional runner blade surface. In addition, the camber surface of the runner blade is generated. Two copies of this surface define the periodical surfaces by rotating it with plus/minus half angular pitch from the actual position. As a result we obtain the three-dimensional solid domain of the blade passage, including the blade itself. Finally, the three-dimensional computational domain of the Francis runner is obtained by subtracting the runner blade solid from the blade passage solid.

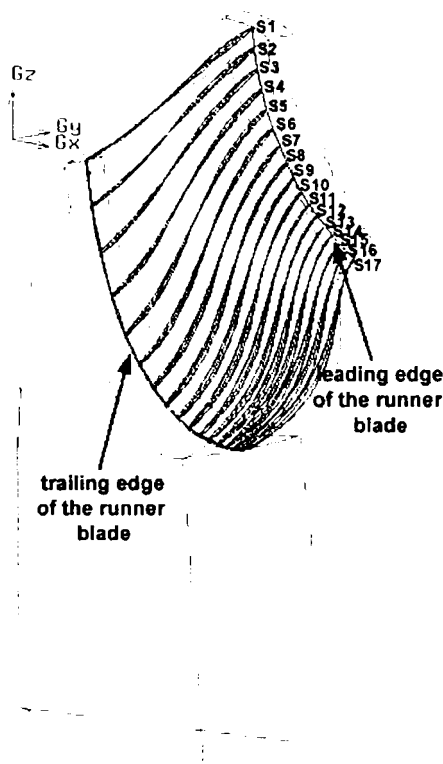


Figure 14. The 17 sections for the geometrical description of the Francis runner blade.



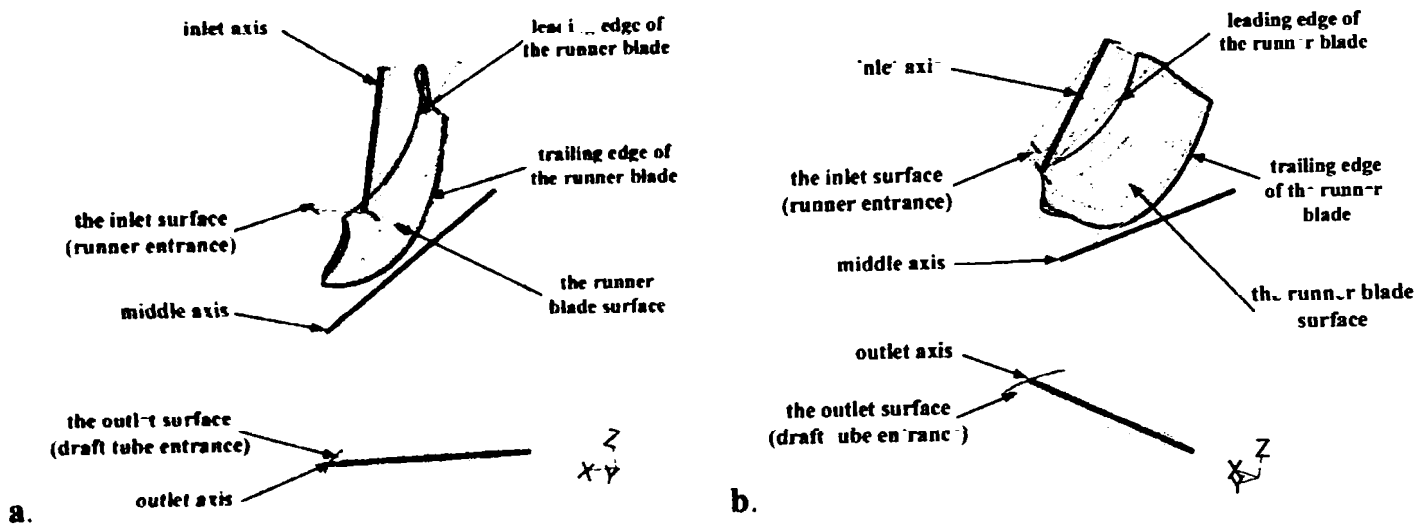


Figure 15. Three-dimensional computational domain for the GAMM Francis runner and the flow survey axes.

This three-dimensional computational domain is discretized using an unstructured mesh, Figure 16. The mesh has been generated using the FLUENT pre-processor, Gambit (1998).

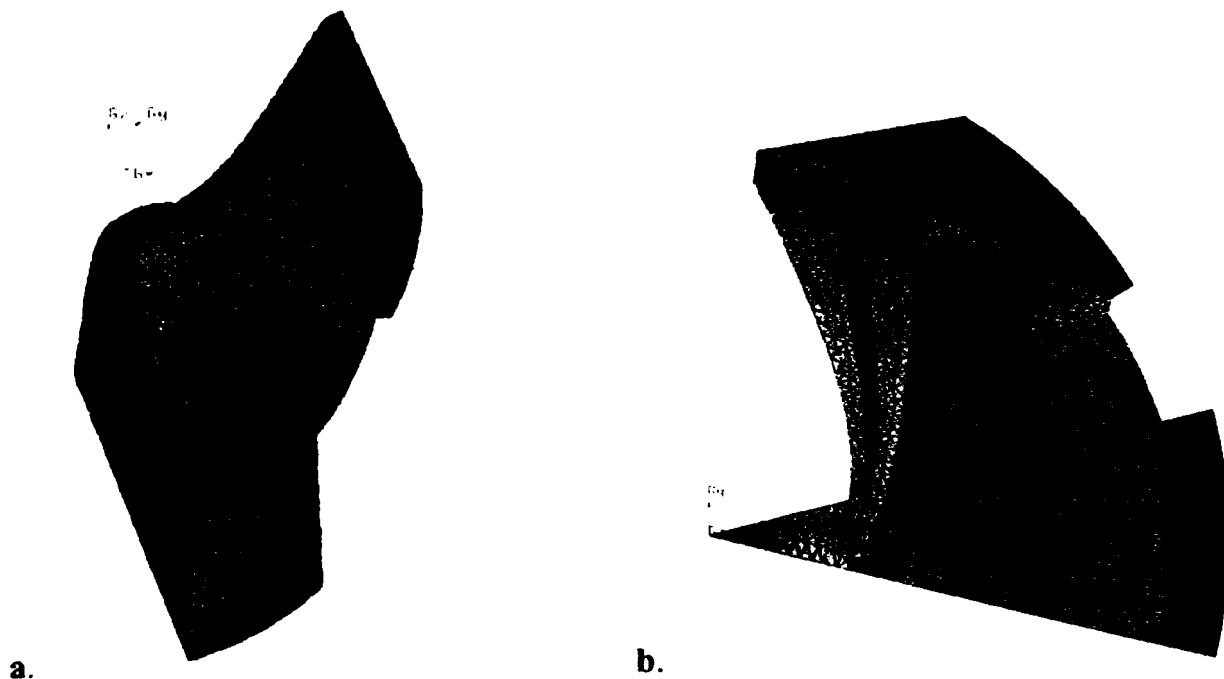


Figure 16. Unstructured mesh (tetrahedra) for the runner domain.

The following boundary conditions for the Francis runner are considered:

- **velocity field** is prescribed on *the inflow section* of the runner domain;
  - *measured velocity distribution*: Data corresponding to the actual velocity field measured at the runner inlet, Sottas & Ryhming (1993);
  - *corrected velocity distribution*: The discharge value obtained by integrating along an inlet survey axis differs from the discharge accurately measured by the flowmeter, mainly due to the non-axi-symmetric nature of the flow. For example, the discharge value obtained by integrating the measured velocity is  $0.339 \text{ m}^3/\text{s}$ , 8.9% smaller than the measured discharge  $0.372 \text{ m}^3/\text{s}$ , Sottas & Ryhming (1993). Therefore, the velocity profile on the runner inlet section is adjusted to match the measured flow rate. The adjustment is simply made by rescaling the absolute velocity components by a constant factor; by doing so, the relative flow angle  $\beta$  is slightly modified, Bottaro et al. (1993);



- **pressure distribution** is prescribed on the runner outlet section;
  - *measured pressure distribution*: In this case, on the draft tube inlet section the measured pressure distribution is imposed, Sottas & Ryhming (1993);
  - *radial equilibrium outlet condition*: One could employ a condition that is a velocity-pressure relationship. Such condition can be devised by assuming that in this section there is no radial flow, i.e.  $v_r = 0$  or negligible. The radial projection of the momentum equation yields,

$$\frac{\partial p}{\partial r} = \frac{\rho v_u^2}{r}$$

This is the so-called *radial equilibrium outlet condition*. However, this condition defines the pressure up to an additive constant. Therefore, a pressure value should be specified at  $r = 0$ . Numerical experiments have shown that enforcing a measured pressure distribution on the runner outlet produces spurious recirculation after the flow leaves the blades, in disagreement with the measured velocity field. On the other hand, from the engineering viewpoint, neither velocity nor pressure distributions are a priori known.

- **periodical conditions** are imposed on the periodic boundary;

$$\bar{W}(r, \theta, z) = \bar{W}\left(r, \theta + \frac{2\pi}{Z}, z\right) \text{ and } p(r, \theta, z) = p\left(r, \theta + \frac{2\pi}{Z}, z\right)$$

- **wall conditions** are imposed in the runner blades, as well as on the runner band and crown, respectively. The FLUENT code is able to compute the boundary conditions for the relative velocity, when the relative flow solver is employed. However, the conditions on the blade are homogeneous for the relative flow,  $\bar{w} \cdot \bar{n} = 0$ , but non-homogeneous for absolute flow,  $\vec{v} \cdot \bar{n} = (\vec{\omega} \times \vec{r}) \cdot \bar{n}$ . The FLUENT code chooses the suitable condition on the blade simply by specifying that this boundary should be of wall type.

Three different series of calculations have been performed for the Francis runner, as follows:

- first calculation, marked {1}, uses the corrected velocity distribution on the inflow section and the radial equilibrium condition on the outflow section;
- second computation, indicated by {2}, comprises the following couple of boundary conditions: measured velocity profile on the inlet surface and the radial equilibrium condition on the measured pressure on the outlet surface;
- third calculation, labeled {3}, uses the measured velocity profile on the inlet surface in conjunction with the measured pressure distribution on the outlet surface;

The inviscid and incompressible flow (Euler model) in the Francis runner is computed using the FLUENT 5.7 code as well. In addition to the previous chapter, the following dimensionless quantities are defined:

$$c_m = v_m / \sqrt{2E} = \sqrt{v_r^2 + v_z^2} / \sqrt{2E} \text{ - normalized meridian velocity}$$

$$\beta = \arctg\left(\frac{c_m}{u - c_u}\right) \text{ - relative flow angle}$$

We present here only the numerical results for the {1} set of boundary conditions, i.e. correction inlet velocity components corresponding to the measured discharge and radial equilibrium outlet condition. Also, a brief comparison between {1} and {3} velocity components on the draft tube inlet section is presented. For all figures the computed results are presented by lines ({1} case with solid line and {3} case with dash line) while the experimental data are marked by points.

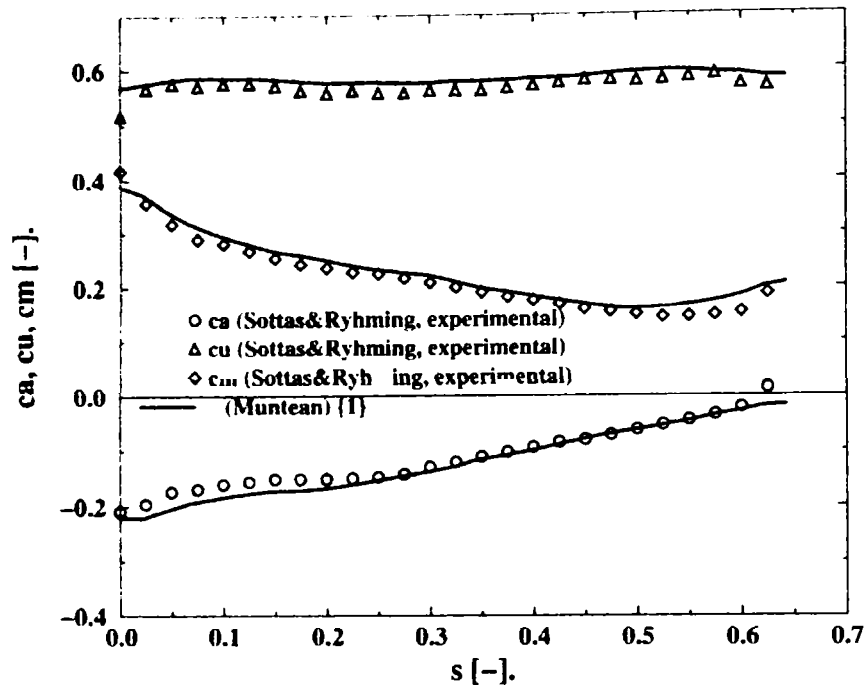


Figure 17. The corrected velocity coefficients on the runner inlet axis BB'. Comparison between the experimental data Sottas & Ryhming (1993) and imposed conditions, Muntean {1} (—).

Figure 17 shows the velocity distribution imposed on the runner inlet surface. The measured velocity components are corrected to ensure the measured discharge. In this case, the absolute velocity components are scaled whilst the normalized peripheral velocity remains unchanged. As a result, the flow velocity triangle is stretched, and although the absolute flow angle remains unchanged, the relative flow angle is modified as shown in Figure 18. Therefore, the interaction between the flow and the runner blade is changed and the runner torque is modified. In conclusion, it is important for the flow direction to be correctly specified on the runner inlet.

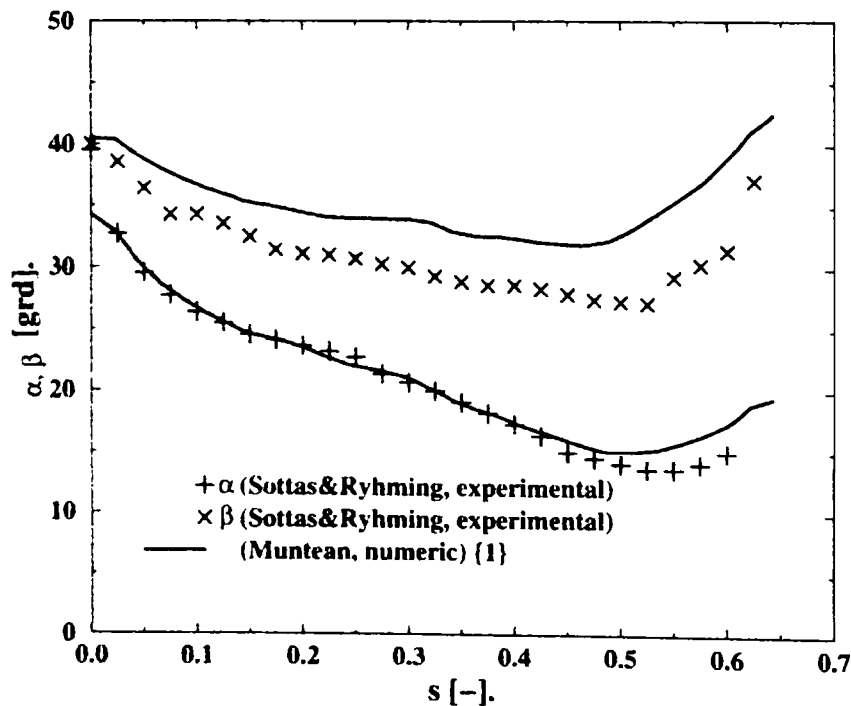


Figure 18. Flow angles on the runner inlet axis BB'. Comparison between the experimental data Sottas & Ryhming (1993) and imposed conditions, Muntean {1} (—).

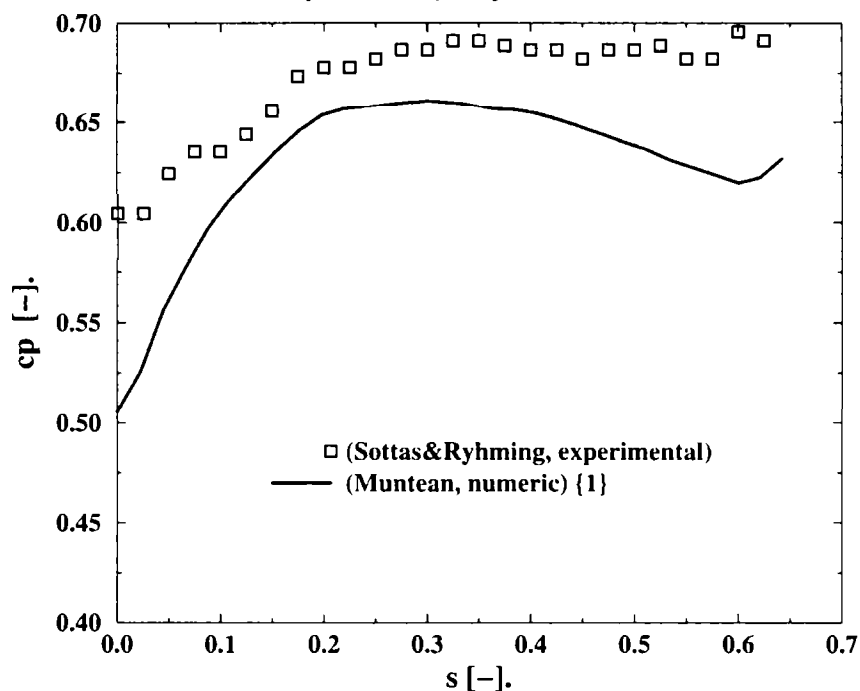


Figure 19. Pressure coefficient on the runner inlet axis BB'. Comparison between the experimental data Sottas & Ryhming (1993) and computed results, Muntean {1} (————).

The computed pressure coefficient on the BB' inlet axis is presented with solid line. As expected, the computed values are smaller than the experimental data since the hydraulic losses are not taken into account. The mean discrepancy is by 10% except the runner band and crown where it is larger because the viscous effects are neglected, Figure 19. Nevertheless, the computed pressure variation along the BB' survey axis matches the same behavior as the experimental one.

Figure 20 presents the velocity components on the runner outlet axis CC'. A good agreement between our numerical results and experimental data is obtained, except near to the crown (large s). The computed axial velocity coefficient  $c_a$  agrees with the experimental data along, but is 5% smaller on average to compensate for the difference near the crown. As far as the tangential velocity coefficient,  $c_u$ , is concerned, we obtain a very good compliance with the experiment along the whole runner CC' axis. Although, the volume flow rate was modified to match the measured discharge, the meridian velocity coefficient  $c_m$  is slightly smaller than the measurements.

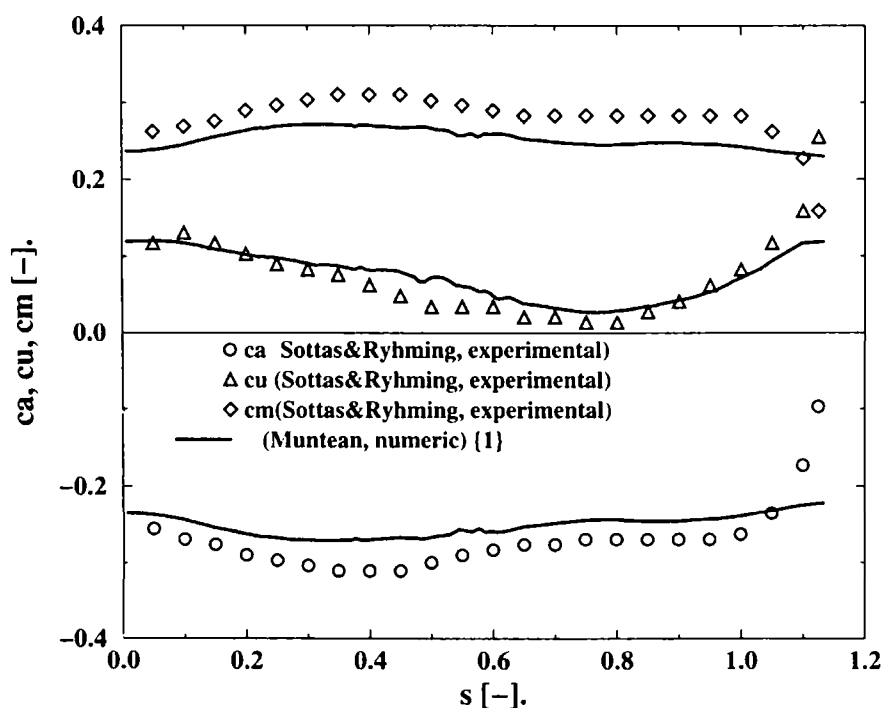


Figure 20. Velocity coefficients on the runner outlet axis CC'. Comparison between the experimental data Sottas & Ryhming (1993) and computed results, Muntean {1} (————).

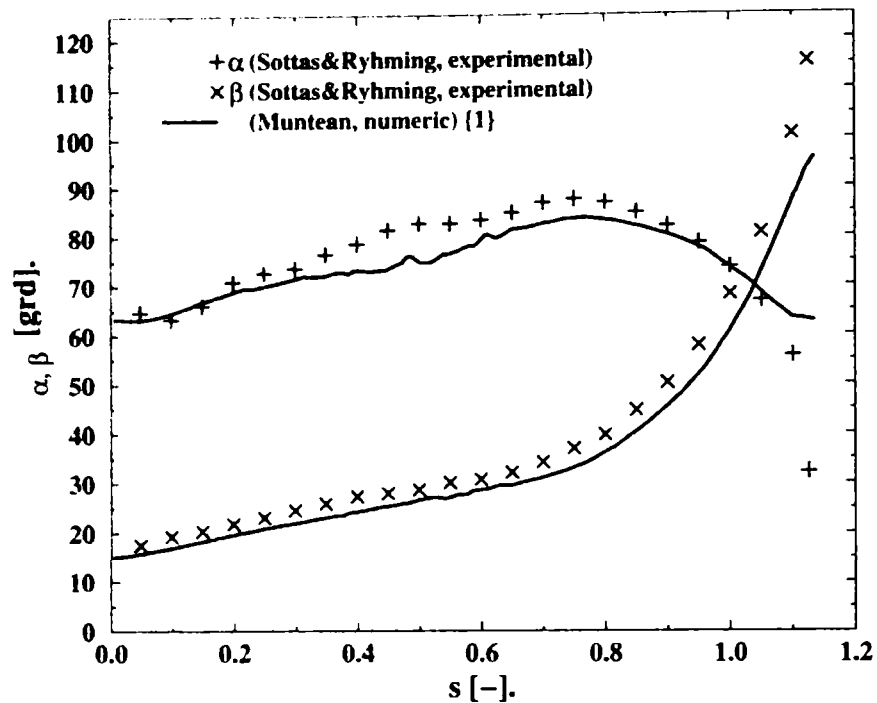


Figure 21. Flow angles on the runner outlet axis  $CC'$ . Comparison between the experimental data Sottas & Ryhming (1993) and computed results, Muntean {1} (—).

Because of the flow angles  $\alpha$  and  $\beta$  depends on the velocity coefficients, the same good concordance with the experimental data is obtained on the runner outlet axis  $CC'$ , Figure 21. One can observe that the absolute flow angle  $\alpha$  monotonically increases from the band to the crown whilst the relative flow angle  $\beta$  has a value of  $60^\circ$  near both the band and the crown, and a maximum value of  $85^\circ$  for  $s=0.75$ . Based on the good agreement computation-experiment shown in Figure 21, we can say that the flow direction right after the runner blades is correctly predicted.

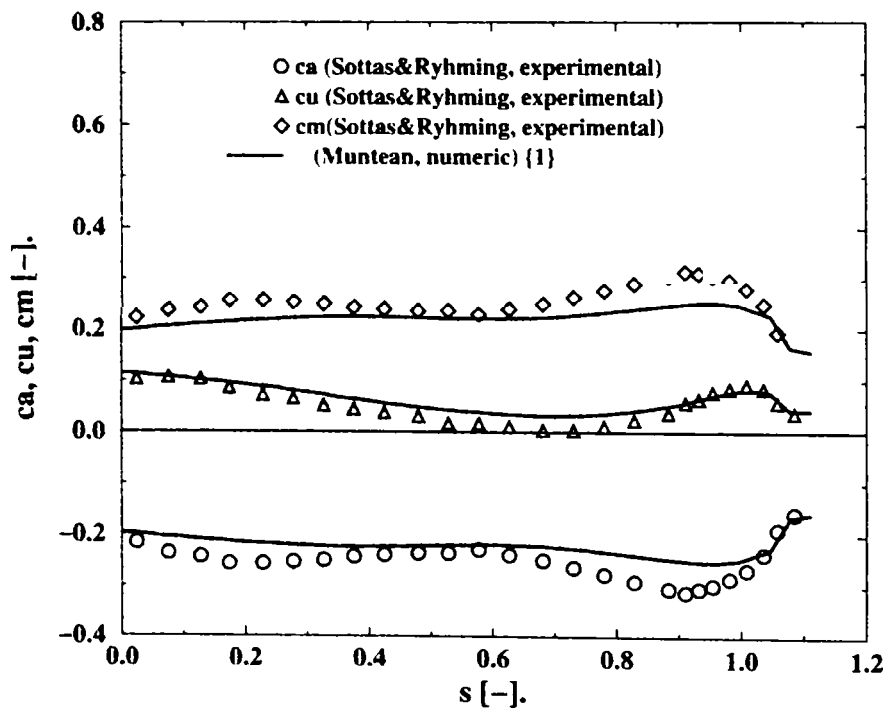


Figure 22. Velocity coefficients on the draft tube inlet axis  $DD'$ . Comparison between the experimental data Sottas & Ryhming (1993) and computed results, Muntean {1} (—).

The velocity components on the draft tube inlet axis  $DD'$  shows a good agreement with the experimental data, Figure 22. Since the radial velocity coefficient  $c_r$  is small, the axial velocity coefficient  $c_a$  approximately equals the meridian velocity coefficient  $c_m$ . The small  $c_r$  values validate the assumption on which the radial equilibrium condition is based, and is correctly predicted by our results.

The tangential velocity coefficient  $c_u$  presents an excellent agreement with the experimental data as well. Since the tangential velocity coefficient is not zero the flow on the draft tube inlet section, there is a swirl motion added to the main axial stream. As a result, not all the flow energy is transferred to the Francis runner even at the best efficiency operating point.

The flow direction, in terms of the absolute  $\alpha$  and relative  $\beta$  flow angles, on the draft tube inlet is shown in Figure 23. Although, the absolute flow angle is correctly predicted, the relative flow angle presents a mean offset of 10-12° to the experimental data. However, we can say that the absolute flow direction at the draft tube inlet is computed correctly.

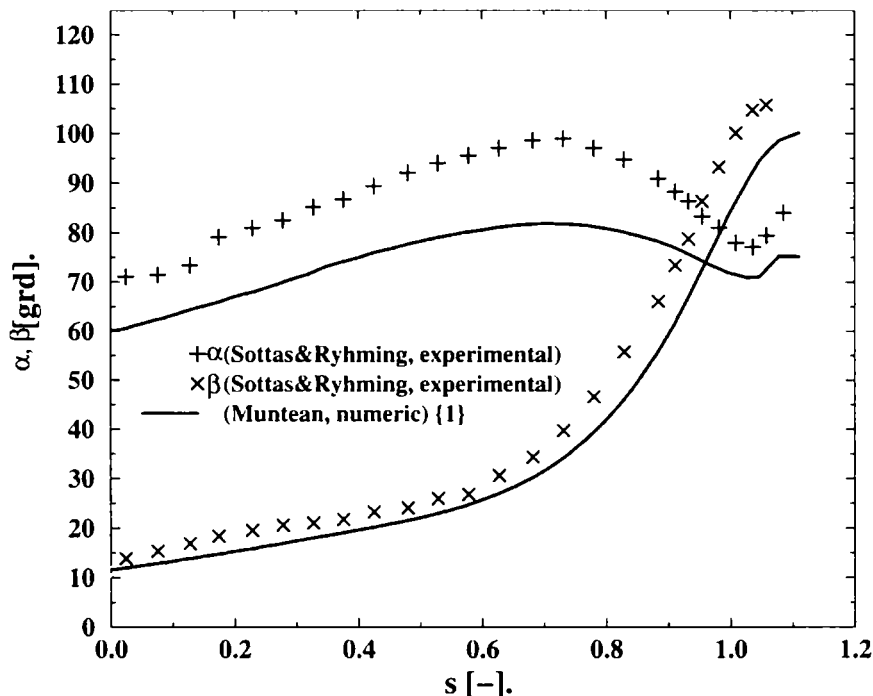


Figure 23. Flow angles on the draft tube inlet axis DD'. Comparison between the experimental data Sottas & Ryhming (1993) and computed results, Muntean {1} (—).

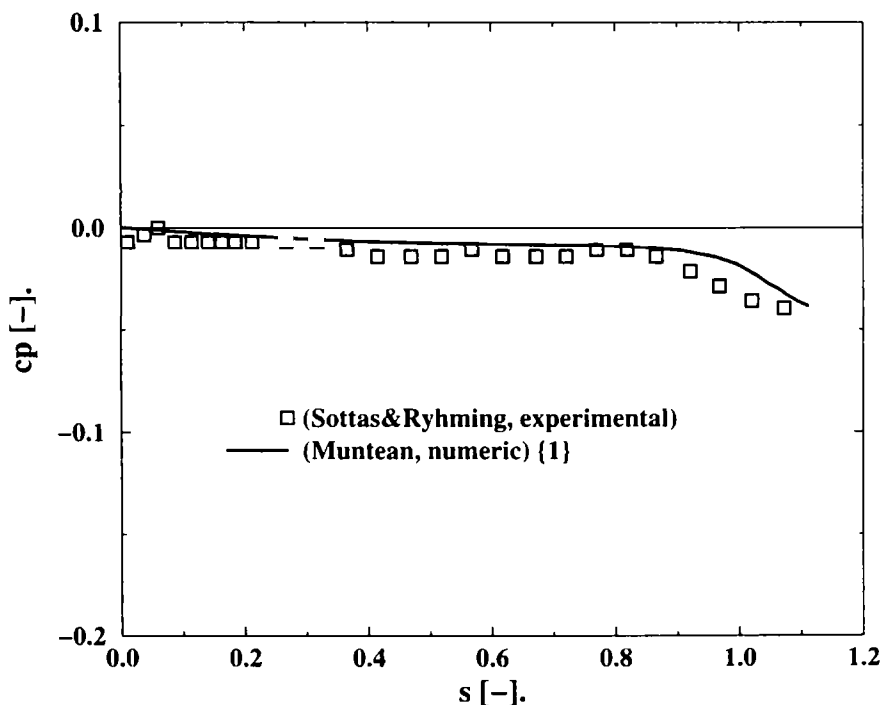


Figure 24. Pressure coefficient on the draft tube inlet axis DD'. Comparison between the experimental data Sottas & Ryhming (1993) and computed results, Muntean {1} (—).

The pressure coefficient computed on the draft tube inlet axis DD' is presented in Figure 24. As mentioned previously, we imposed the radial equilibrium condition on the draft tube inlet section. The excellent agreement between our numerical results and the experimental data confirms our assumption

(negligible radial flow) and validates the new boundary condition prescribed on the draft tube inlet section. The pressure coefficient vanishes for  $s=0$  (solid wall) since the pressure here coincides to the reference pressure. This is also the reason why there is no offset for the computed pressure coefficient on the DD' axis.

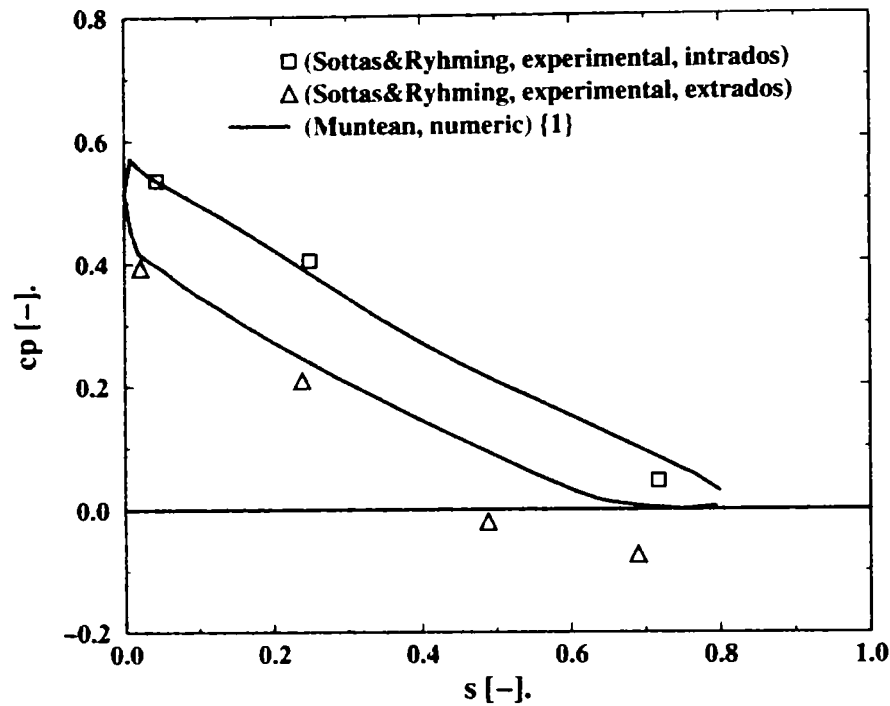


Figure 25. Pressure coefficient on the S2 section of the runner blade. Comparison between the experimental data Sottas & Ryhming (1993) and computed results, Muntean {1} (———).

Finally, we investigate the pressure distribution on the runner blade. Near the crown, section S2 from Figure 2, one can see in Figure 25 that the method gives reasonable results on the pressure side, but fails to predict the minimum pressure on the suction side, especially near to the trailing edge.

Figure 26 shows the pressure on the middle section S9 of the Francis runner blade. The same conclusion can be drawn from Figure 26, where the pressure coefficient is correctly computed on the pressure side as well as reasonable estimated in the neighborhood of the leading edge, but fails to match the minimum pressure on the suction side near to the trailing edge.

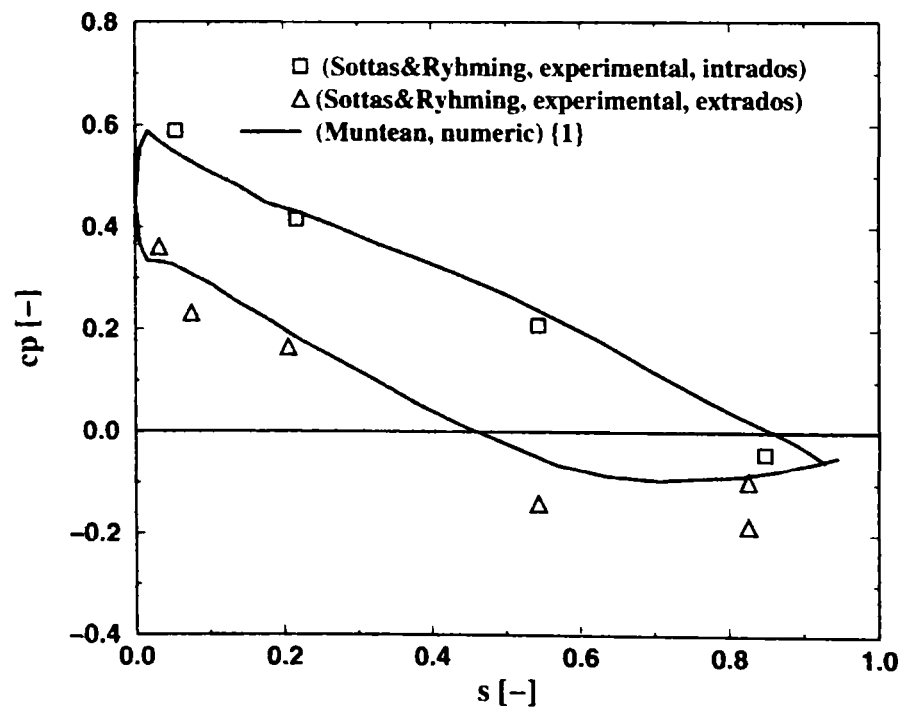


Figure 26. Pressure coefficient on the S9 section of the runner blade. Comparison between the experimental data Sottas & Ryhming (1993) and computed results, Muntean {1} (———).

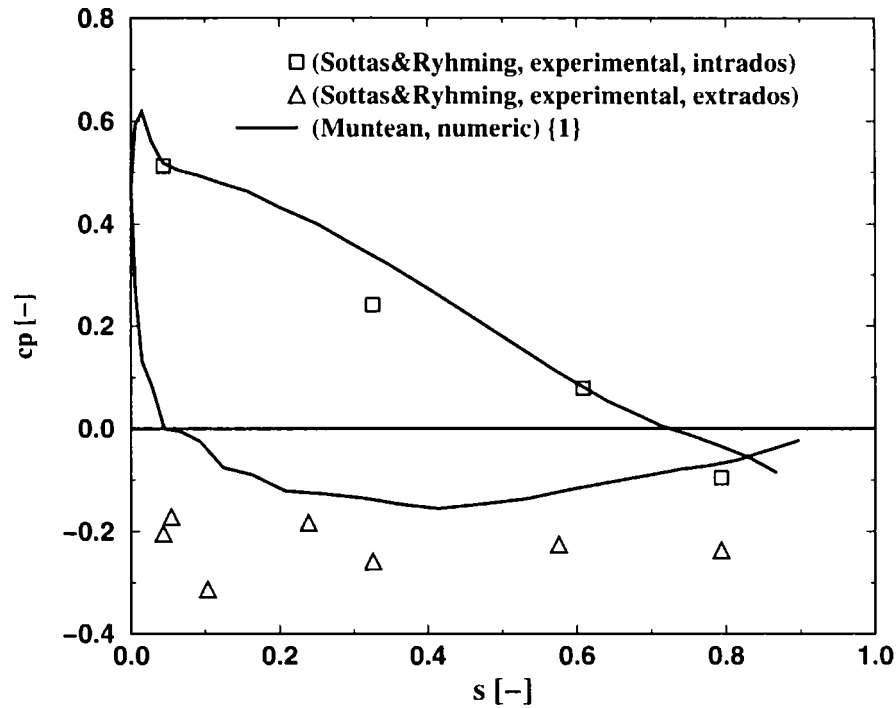


Figure 27. Pressure coefficient on the S15 section of the runner blade. Comparison between the experimental data Sottas & Ryhming (1993) and computed results, Muntean {1} (—).

Results for the section S15, near to the band, are presented in Figure 27. Here we have a good agreement on the pressure side as well, but the pressure is strongly overestimated on the whole suction side. However, this is a general observation for computations performed by various research groups, and at some point one may question the accuracy of the experimental data.

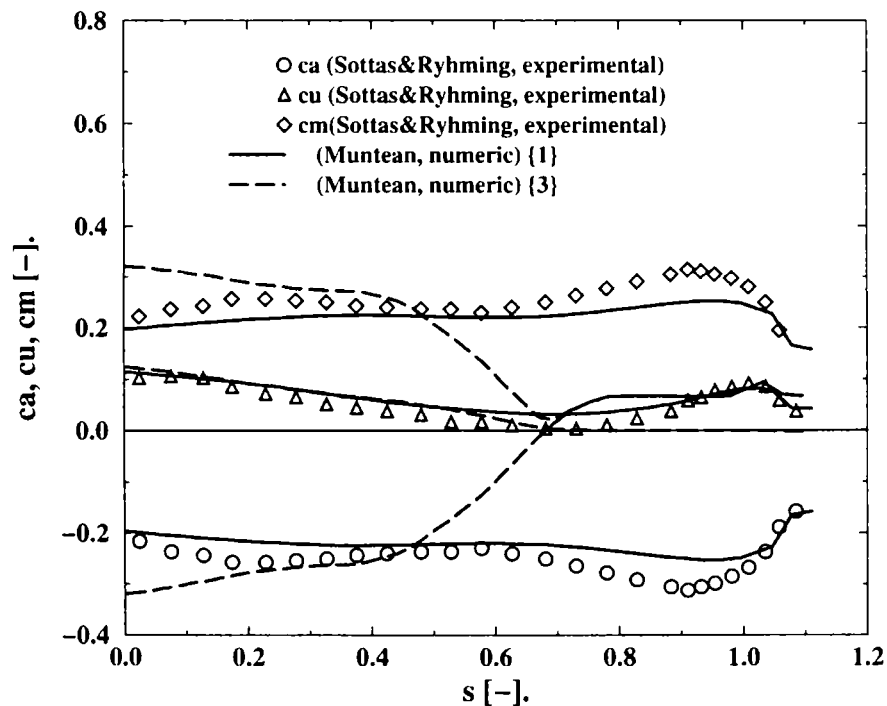


Figure 28. Velocity components on the draft tube inlet axis DD'. Comparison between the experimental data Sottas & Ryhming (1993) and computed results, Muntean {1} (—) and Muntean {3} (---).

Numerical experiments shows that enforcing a measured pressure distribution at the draft tube inlet produces spurious recirculation after the flow leaves the blades, in disagreement with the measured velocity field, Muntean {3}, while imposing the *radial equilibrium condition* on the draft tube inlet predicts the correct velocity field, Muntean {1}.

The results presented above correspond to the radial equilibrium condition on the outflow section, which we strongly advocate for the runner computations. Imposing the measured pressure distribution as boundary condition in this section produces very poor results, as shown with dashed lines in Figure 28. The numerical results obtained by imposing the measured pressure distribution Muntean {3} (---) indicate a spurious recirculation after the flow leaves the blades in disagreement with the measurements, Sottas & Ryhming (1993). Moreover, since no pressure distribution needs to be prescribed, a new perspective is opened to perform numerical simulation at off-design operating points.

Our best numerical results Muntean {1} (—) (velocity, angles and pressure fields on the survey axes as well as pressure coefficient on the sections of the runner blade) are also compared with other numerical results reported by other groups at the “3D-computation of incompressible internal flows” workshop held in 1989 at Lausanne: Billdal et al. (1993), Bottaro et al. (1993), Eliasson (1993), Goede (1993), Grimbert et al. (1993) and Nagafuji et al. (1993). This comparison allows us to infer that the present methodology is very accurate and efficient.

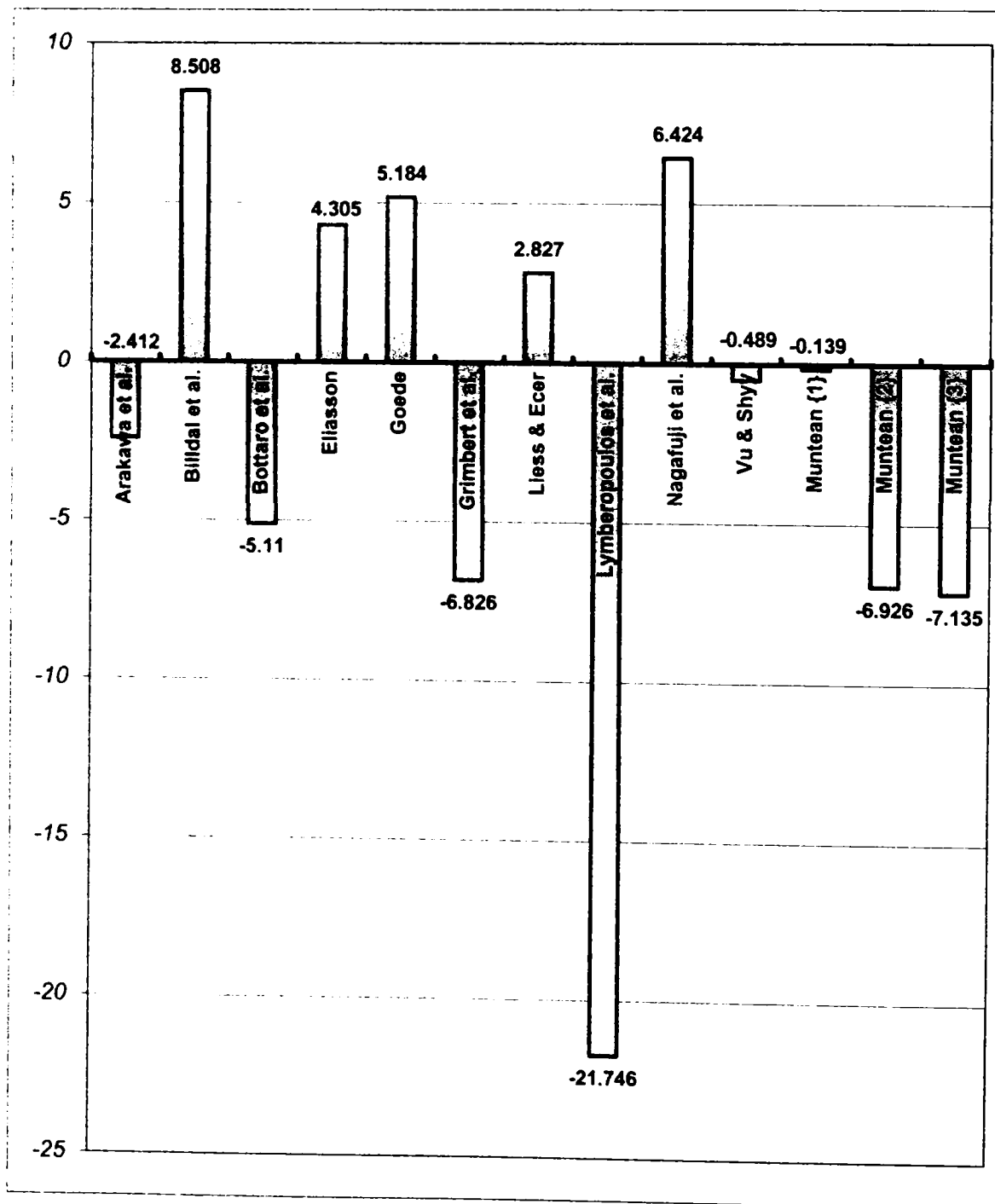


Figure 29. Relative error of the Francis runner torque coefficient.

In the last analysis of this chapter, the relative error for the hydraulic torque coefficient between our numerical results Muntean {1} -0.14%, Muntean {2} -6.93% and Muntean {3} -7.14%, the numerical results for all groups from the “3D-computation of incompressible internal flows” workshop and the experimental values are compared. In our case Muntean {1}, the torque coefficient is underestimated by



0.14%. This result can be mainly attributed to the correct (measured) discharge value obtained by correcting the inflow velocity component, as well as to the correct prediction of the flow turning angle.

In conclusion, this chapter presents a methodology for computing the three-dimensional inviscid, incompressible flow in the Francis turbine runner at the best efficiency operating point. The computational domain corresponds to the actual turbine geometry. A methodology is developed for generating the 3D GAMM Francis runner computational domain. The complicated shape of the runner computational domain is generated using an original and efficient technique. An unstructured discretization (tetrahedral) of the 3D computational domain is employed. Next, the investigation is focused on the inflow/outflow boundary conditions. It is shown that accurate numerical results require a correct value for the prescribed discharge. It is shown that by imposing the pressure distribution on the draft tube inlet section a spurious recirculation is numerically generated after the flow leaves the runner blades, in disagreement with the measured velocity field. Taking into account the actual velocity field on the draft tube conical section we introduce the radial equilibrium condition. The assumptions considered when employing the radial equilibrium condition are validated by the excellent agreement of numerical results and experimental data. Imposing this boundary condition on the draft tube inlet section will eliminate the need for experiments and opens new perspectives for simulating off-design operating points.

After computing the velocity and pressure fields in the Francis turbine runner we evaluate runner torque coefficient. Our value is only 0.14% smaller than the experimental value, thus demonstrating the ability of this methodology to predict the turbine performances. Moreover, knowledge of the pressure field on the runner allows the prediction of the cavitation behavior of the Francis turbine. As a result, the method presented in this chapter is a reliable and efficient design and/or optimization tool for the Francis turbine runner.



## Chapter 6

## 6. Euler Numerical Simulation of the 3D Incompressible Flow through GAMM Francis Turbine Distributor at Off-Design Operating Conditions

This chapter is devoted to the numerical analysis of the 3D distributor flow for variable discharge, corresponding to several values of the opening angle. First, using the turbine hill chart we establish the dependence of discharge versus guide vane opening for the whole range of opening angles. Second, using the numerical methodology developed in Chapter IV, the distributor flow at several guide vane angles is computed. As a result, the guide vane torque versus guide vane angle is computed.

Using this methodology we define an optimization procedure for the guide vane axis position. When changing this axis position we practically define a new radial cascade, even if the blade geometry is unchanged. As a result, a new numerical technique for hydrodynamic equivalence of the radial cascades is developed. This technique is applied to three equivalent radial cascades. Accordingly, the guide vane torque versus guide vane opening angle at different gate shaft positions is obtained. The optimum axis position is then chosen such that the maximum torque modulus is minimized. This optimum position is slightly shifted toward the guide vane trailing edge compared to the actual position. The methodology can be employed for the current engineering design and optimization of the guide vane regulating apparatus in order to minimize the mechanical loading requirements for all machine parts used to move the guide vanes (guide vane servomotors, regulating ring and guide vane linkage).

Figure 30 presents the discharge versus guide vane angle at the optimum constant energy. The points are read on the GAMM Francis turbine hill chart at the different guide vane angle and constant energy, as follow: those marked  $\bullet$  are for the hill chart without the draft tube (see Figure 4 down), and the other, noted  $\circ$ , for the hill chart with the draft tube (see Figure 4 up). Taking the discharge values at several guide vane angles and constant energy on the GAMM Francis turbine hill chart *without* the draft tube, a parabolic regression is accurate enough to represent the correlation  $Q = f(\alpha)$ .

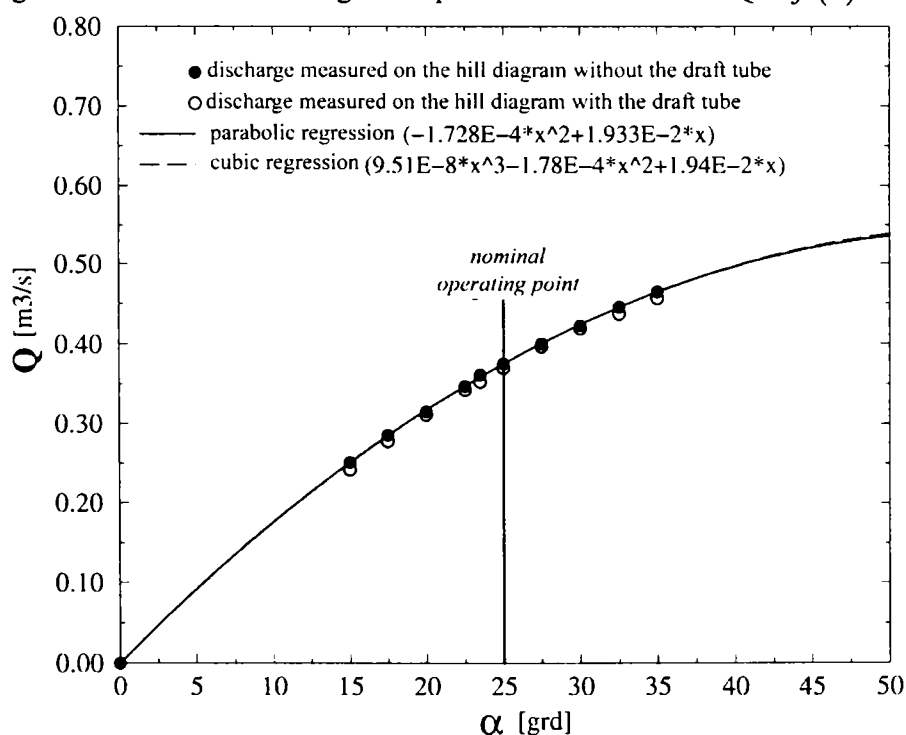


Figure 30. Discharge versus guide vane angle for GAMM Francis turbine. The experimental data was reading on the hill chart at the constant hydraulic energy.

Using the numerical methodology developed in chapter IV, the distributor flow at eleven guide vane angles is computed. The three-dimensional computational domain of the turbine distributor at each guide vane angles together with its unstructured mesh is generated. In all cases, the numerical simulation

has the same boundary conditions like D1 set (see chapter IV). Consequently, the following assumptions are made:

- **uniform velocity distribution on the inlet boundary condition** is prescribed. The advantage of imposing the boundary conditions at the stay vane inlet is that it can easily be derived from the global data corresponding to flow rate of the water. As a result, using the parabolic function  $Q = f(\alpha)$  computed above, the radial velocity component  $c_r$  results at variable discharge. The flow direction at the different guide vane angles is assumed to be constant over the whole cylindrical distributor inlet section, corresponding to an ideal spiral casing. This assumption in conjunction with zero incidence flow angle ( $\gamma^{sv}=34^\circ$ ) on the stay vane allows us to compute the tangential velocity component  $c_u$  at variable discharge. Due to the ideal spiral case hypothesis, the flow is plane parallel on the distributor inlet section and the axial velocity component is set to zero,  $c_a = 0$ ;
- since, **the pressure distribution on the outflow surface** is a priori unknown, the constant mean pressure is considered on the outflow section.

The computational domain and boundary conditions at various guide vane angles are presented in Figure 31.

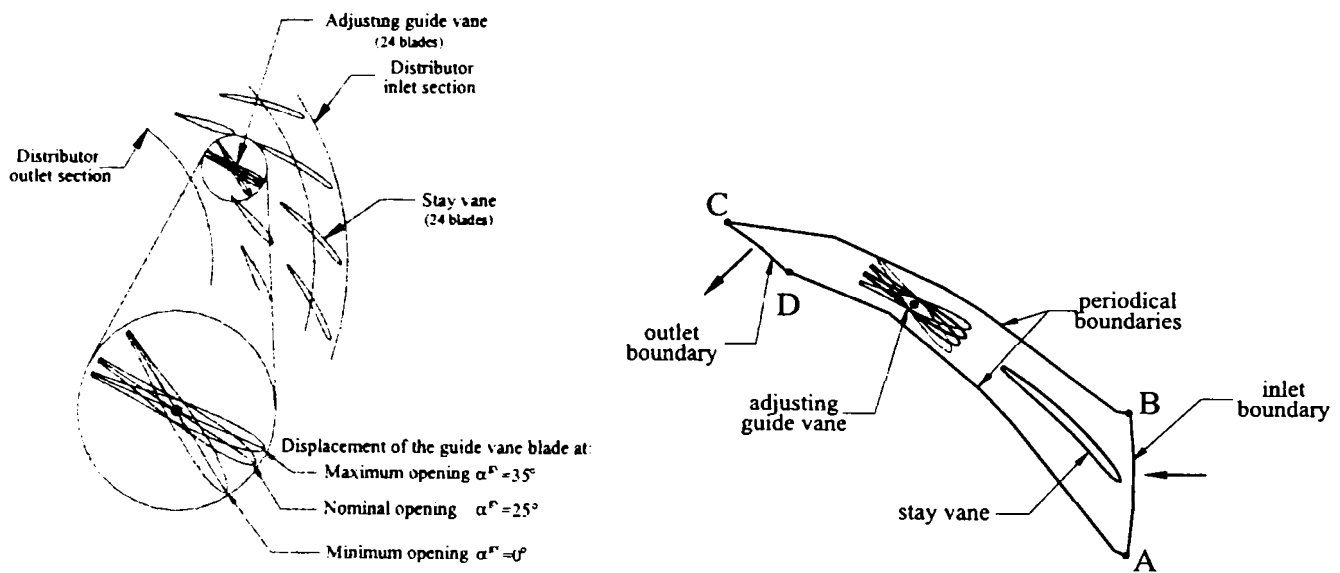


Figure 31. Computational domain of the GAMM Francis distributor and boundary conditions for various guide vane angles.

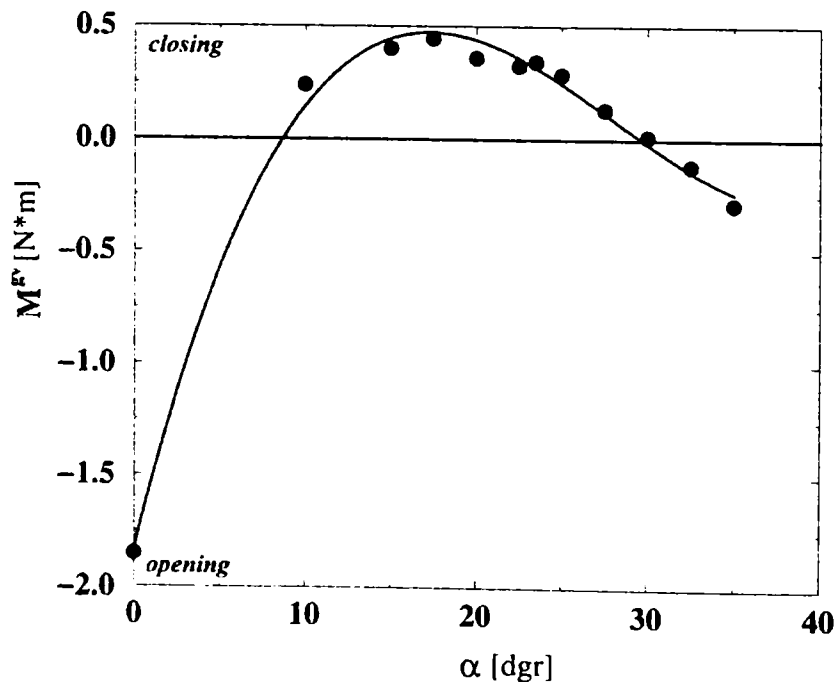


Figure 32. Guide vane torque versus guide vane angle for the GAMM distributor at  $n_0=0.07208$  ( $e=0$ , i.e. actual GAMM Francis turbine design).

Once the numerical simulations are performed at the eleven angles of the guide vane, the guide vane torque ( $M^{GV}$ ) is obtained. Figure 32 shows the numerical values, marked •, for the guide vane torque versus guide vane angles for actual GAMM Distributor, at  $n_0=0.07208$  ( $e=0$ ). The solid line is a least squares fit with a cubic function. One can observe that the absolute maximum value of the guide vane torque appears at the closing position. This value is four times larger (absolute values) than the other maximum value. As a result, one can ask *which would be the axis position for a smallest torque extreme*. The rest of this chapter is devoted to answering this practical engineering question.

One should recognize that a new position of the guide vane axis leads to a new geometry for the guide vane cascade. As a result, the previous  $Q = f(\alpha)$  dependence is no longer valid. Therefore, a method for finding the new  $Q = f(\alpha)$  is required. Traditionally, this is done using geometrical considerations. However, we consider that hydrodynamic considerations are more appropriate. Using the previous numerical simulations we can compute the distributor pressure drop versus guide vane angle  $\Delta p = f(\alpha)$  for the original GAMM distributor, Figure 33.

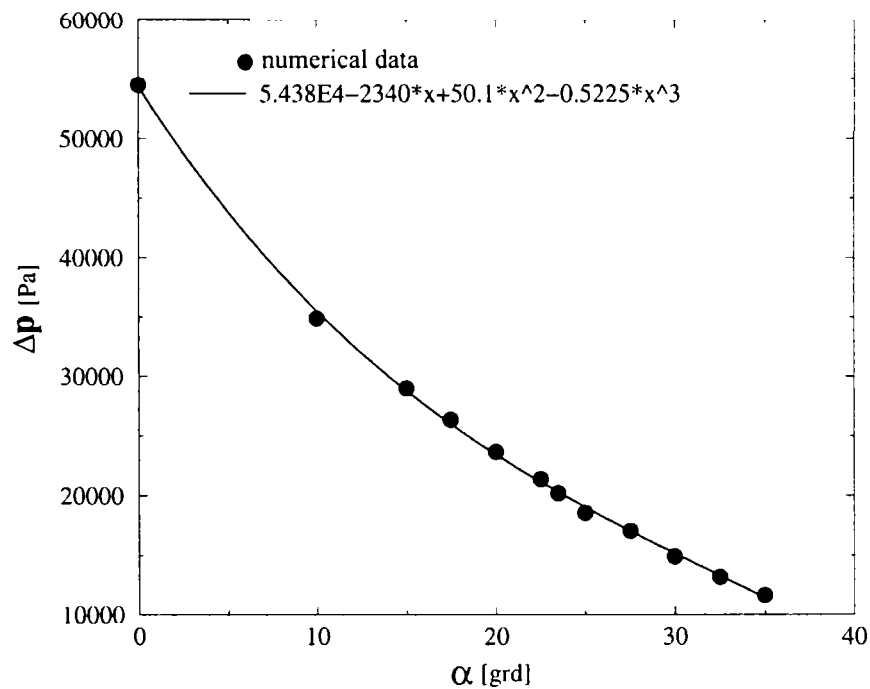


Figure 33. Pressure drop versus guide vane angle for the GAMM distributor.

Now we eliminate the guide vane angle ( $\alpha$ ) from the discharge versus guide vane angle ( $Q = f(\alpha)$  Figure 30) and the distributor pressure drop versus guide vane angle ( $\Delta p = f(\alpha)$  Figure 33). The result is a distributor pressure drop versus discharge  $\Delta p = f(Q)$  curve, as shown in Figure 34. We call this dependence the “*distributor regulation curve*”. Now we can state the following hydrodynamic equivalence rule: *two different radial cascades are said to be equivalent if at the same discharge value produce the same distributor pressure drop*. Obviously, the guide vane angular position will not necessarily be the same for two equivalent cascades operating at the same point on the distributor regulation curve. However, the above equivalence criterion insures identical runner inlet flow for a given discharge, no matter the radial guide vane cascade geometry.

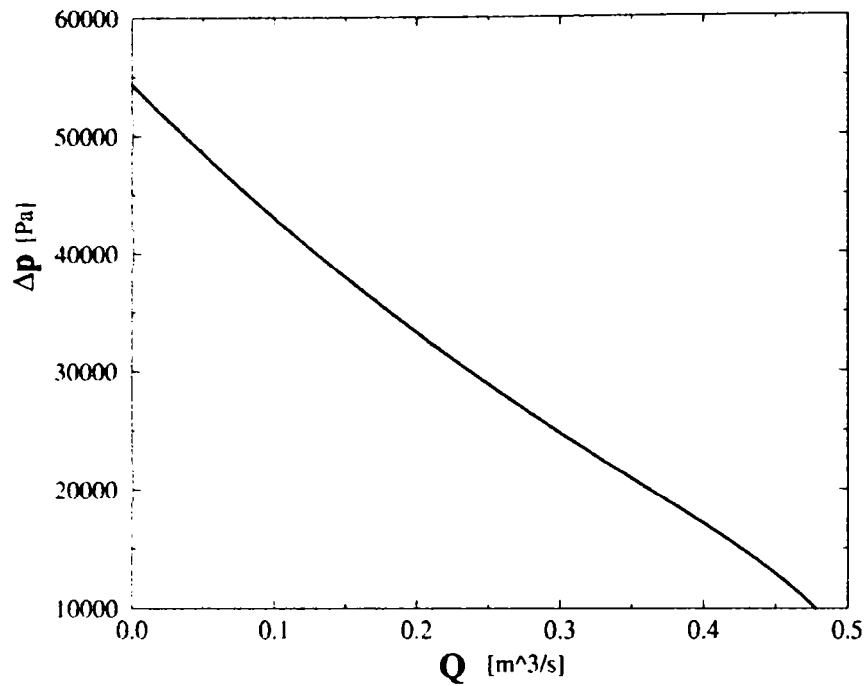


Figure 34. Pressure drop versus discharge for the GAMM distributor at  $n_0=0.07208$  ( $e=0$ ). This curve is called “distributor regulation curve”.

Each new radial cascade is identified by a geometrical parameter, namely the eccentricity  $e$  [mm] or the dimensionless eccentricity  $n_0$ ,

$$n_0 = \frac{l_{01} - l_{02}}{2 \cdot l_0},$$

where the lengths  $e$ ,  $l_0$ ,  $l_{01}$  and  $l_{02}$  are defined in Figure 35.

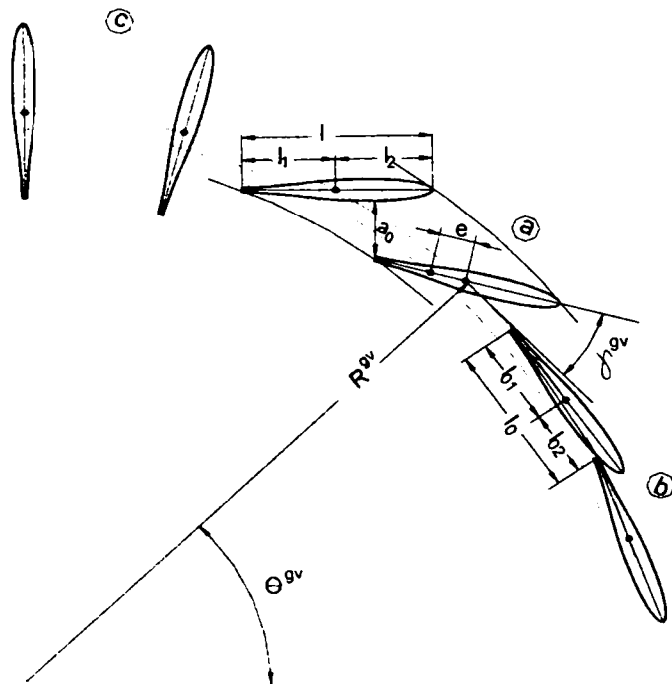


Figure 35. Guide vane geometrical parameters.

By employing the above hydrodynamic equivalence technique, we compute the guide vane torque for the whole range of the guide vane angles and three positions of the guide vane shaft:  $n_0=-0.00247$  ( $e=-5$  mm),  $n_0=0.14508$  ( $e=+5$  mm) and  $n_0=0.21656$  ( $e=+10$  mm). Positive values for the eccentricity mean that the guide vane shaft is moved toward the leading edge of the guide vane blade.

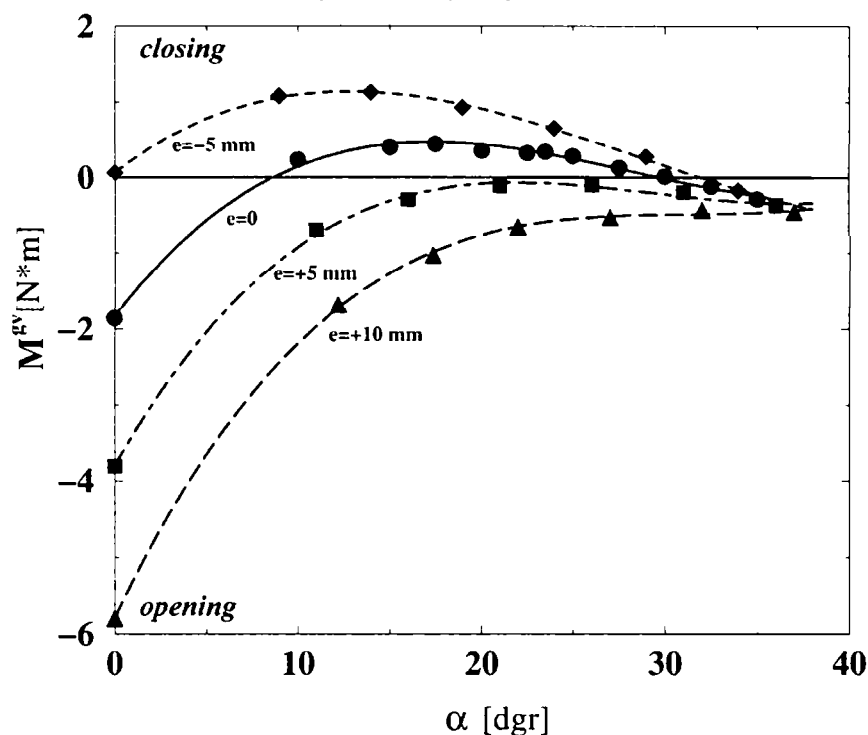


Figure 36. Guide vane torque versus guide vane angle at four positions of the guide vane shaft  $n_0 = -0.00247$  ( $e = -5$  mm),  $n_0 = 0.07208$  ( $e = 0$ ),  $n_0 = 0.14508$  ( $e = +5$  mm) and  $n_0 = 0.21656$  ( $e = +10$  mm). The solid line corresponds to the actual GAMM distributor  $n_0 = 0.07208$  ( $e = 0$ ), see Figure 32.

Figure 36 presents the guide vane torque versus guide vane angle at four position of the guide vane shaft. The numerical data obtained at several constant guide vane and the four positions of the guide vane shaft angles are marked as follows:  $\blacklozenge$  for  $n_0 = -0.00247$  ( $e = -5$  mm),  $\bullet$  for  $n_0 = 0.07208$  ( $e = 0$ ),  $\blacksquare$  for  $n_0 = 0.14508$  ( $e = +5$  mm) and  $\blacktriangle$  for  $n_0 = 0.21656$  ( $e = +10$  mm). The solid line corresponds to the original GAMM distributor  $n_0 = 0.07208$  ( $e = 0$ ), see Figure 32. A least square fit with a cubic polynomial is obtained for each new position of the guide vane shaft: the dashed line for  $n_0 = -0.00247$  ( $e = -5$  mm), the dot-dashed line for  $n_0 = 0.14508$  ( $e = +5$  mm) and the long dashed line for  $n_0 = 0.21656$  ( $e = +10$  mm).

We define the optimum position of the guide vane shaft that one which equals (in magnitude) the two extreme values of the guide vane torque. As a result, this situation leads to the minimum load on the guide vane regulating apparatus thus obtaining an optimum guide vane regulating apparatus is design.

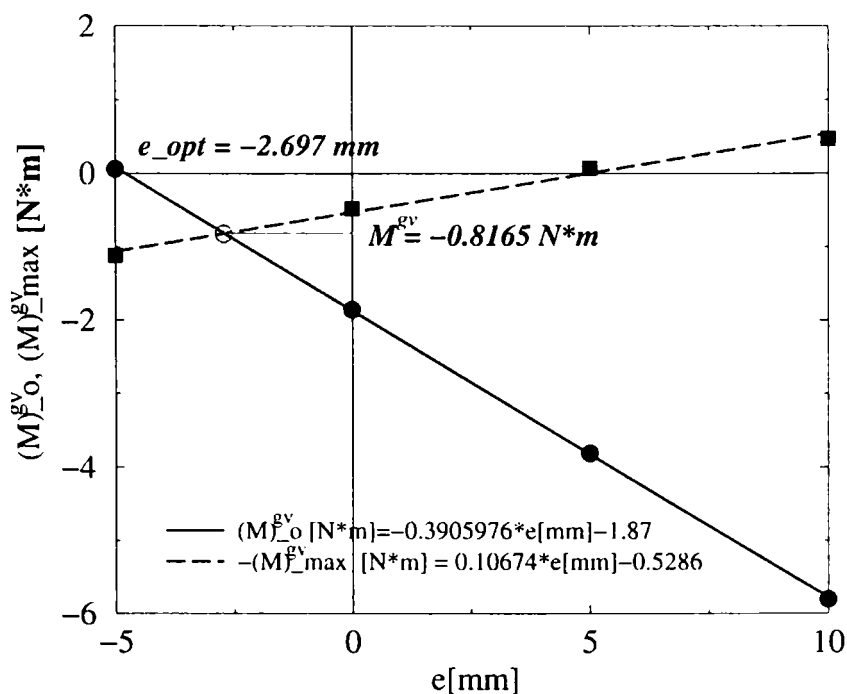


Figure 37. Extreme values of the guide vane torque  $(M)_{\max}^{\text{gv}}$  and  $(M)_o^{\text{gv}}$  versus eccentricity.

The optimum position according to the above criterion is shown in Figure 37. The optimum position represents the intersection of the extreme values of the guide vane torque, the maximum value  $(M)_{\max}^{\text{gv}}$  and the value at the closing position of the guide vane  $(M)_0^{\text{gv}}$ . According to the criterion defined above the optimum eccentricity for GAMM distributor is  $e_{\text{opt}} = -2.697$  mm. In other words, the minimum guide vane torque  $(M)_{\min}^{\text{gv}} = 0.8165$  Nm is obtained by moving the guide vane shaft by 2.697 mm toward the trailing edge of the guide vane blade from its actual position.

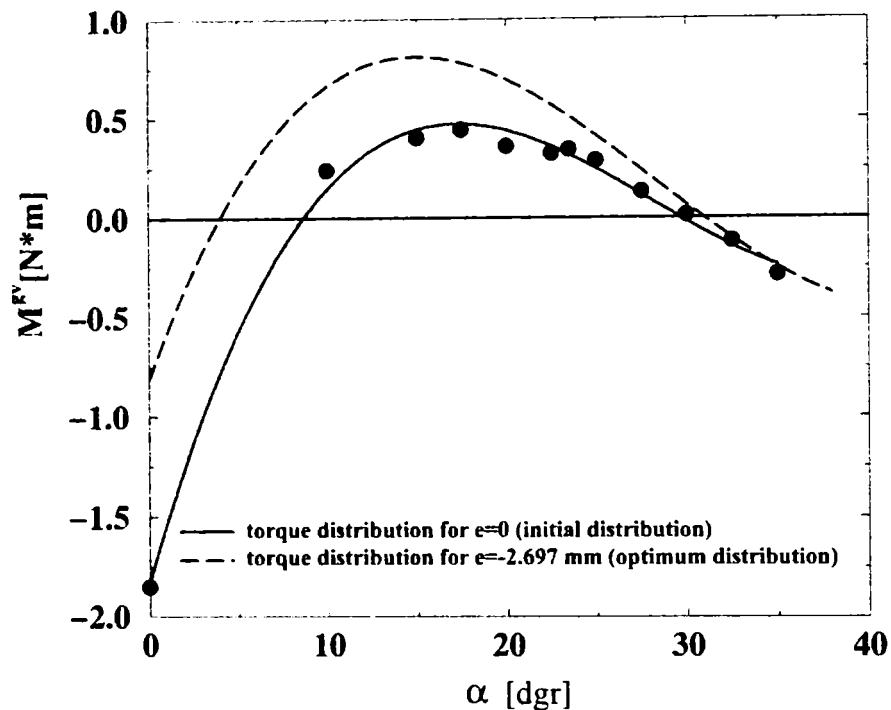


Figure 38. The original (solid line) and optimum (dashed line) torque versus guide vane angle for GAMM distributor.

Figure 38 presents the original (solid line) and optimum (dashed line) torque distribution for the whole angle range of the GAMM guide vane.

According to the dimensionless eccentricity definition  $n_0$ , the optimum position of the guide vane shaft is obtained at  $n_0=0.032$ . The literature recommends for the guide vane that contains 24 blades and symmetric profile  $n_0=0.040$ , Kovalev (1961) p. 233, Anton (1979) p. 324.

In conclusion, a numerical analysis of the three-dimensional distributor flow for variable discharge was performed. Based on the numerical results, an original numerical methodology for optimizing the guide vane axis position for the whole range of the guide vane openings and constant energy was developed. This numerical methodology is based on an original hydrodynamic equivalence criterion, and is exemplified for the GAMM distributor. As a result, the minimum guide vane torque is obtained. The methodology can be employed for the current engineering design and optimization of the guide vane regulating apparatus in order to minimize the mechanical loading requirements for all machine parts used to move the guide vanes (guide vane servomotors, regulating ring and guide vane linkage).



## 7. Euler Numerical Simulation of the 3D Incompressible Flow through GAMM Francis Turbine Runner at Off-Design Operating Conditions

In this chapter we develop a methodology for computing the three-dimensional flow through the Francis turbine runner at variable operating point. Since the runner inflow conditions originate from the distributor flow, a distributor-runner flow coupling technique is developed. This technique is applied for the best efficiency operating point as well as at eight off-design operating points (four points corresponding to a constant optimum guide vane opening and other four points at constant optimum energy). The pressure coefficient distribution on the runner blade is computed for all operating points under investigation. This is a prerequisite for the cavitation behavior analysis to be presented in the next chapter. Also, the hydrodynamic field corresponding to off-design operating points is checked against available experimental data.

Our method for computing the distributor-runner flow is designed by assuming steady absolute flow through the distributor and a steady relative runner flow. The absolute flow equations are the natural choice for the distributor, but for the runner one may choose to solve either the absolute or the relative flow. Since our method is to develop an iterative technique to couple the distributor and runner hydrodynamic fields, it is convenient to use absolute velocity conditions at the runner inlet section.

In order to compute the 3D flow through the Francis turbine (i.e. distributor and runner for our work), computational domains have been defined separately for the distributor, Figure 6 (chapter IV), and for the runner, Figure 18 (chapter V). For each domain, the flow is computed separately and an iterative technique is used to match the pressure and velocity fields at the distributor-runner interface generated by the BB' axis. The boundary conditions for computing the flow within computational domains are as follows:

- velocity field is prescribed on the inflow section for both distributor and runner domains;
- pressure distribution is imposed on the distributor outlet section;
- radial equilibrium condition is prescribed on the runner outlet section;
- periodic conditions are imposed on the periodic boundaries;
- wall conditions (i.e. normal velocity) are imposed on the stay, guide, and runner blades, as well as on the distributor upper/lower rings and runner band and crown, respectively.

Since the flow computation is performed separately for the distributor and runner domains, a coupling technique is required in order to obtain a continuous velocity and pressure fields across the conical surface generated by BB'. Accordingly, an iterative coupling method is employed, with the algorithm outlined in Figure 39.

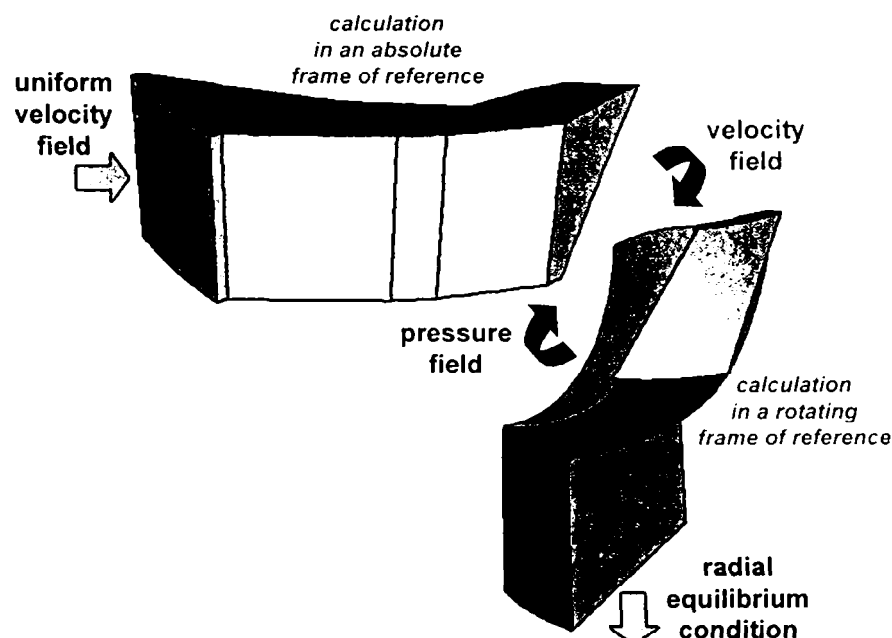


Figure 39. Boundary conditions for the coupled algorithm.

First, the distributor flow is computed, using the inlet velocity from Figure 40, and an arbitrary (e.g. constant, or experimental when available) outlet pressure distribution. Next, iterations are performed as follows:

- compute the runner flow, using the inlet velocity distribution obtained at the distributor outlet, and the radial equilibrium outlet condition for outlet pressure;
- compute the distributor flow, keeping the inlet velocity constant and using the outlet pressure distribution obtained at the runner inlet.

The stopping criterion is that the pressure distribution on the distributor-runner interface is practically unchanged from one iteration to another.

The distributor inlet velocity coefficients are scaled down/up for variable discharge, while the inlet angle remains at the same value shown in Figure 41 no matter the flow rate (ideal spiral case). Note that the radial equilibrium condition at the runner outlet is a key ingredient here, allowing us to solve for various operating points without computing the draft tube flow.

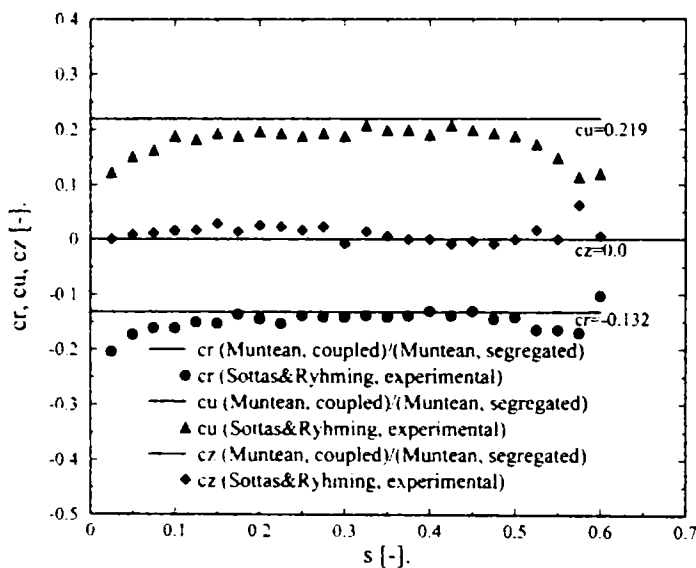


Figure 40. Velocity components on the distributor inlet axis AA' at best efficiency operating conditions P1. Imposed values and comparison with the experimental data.

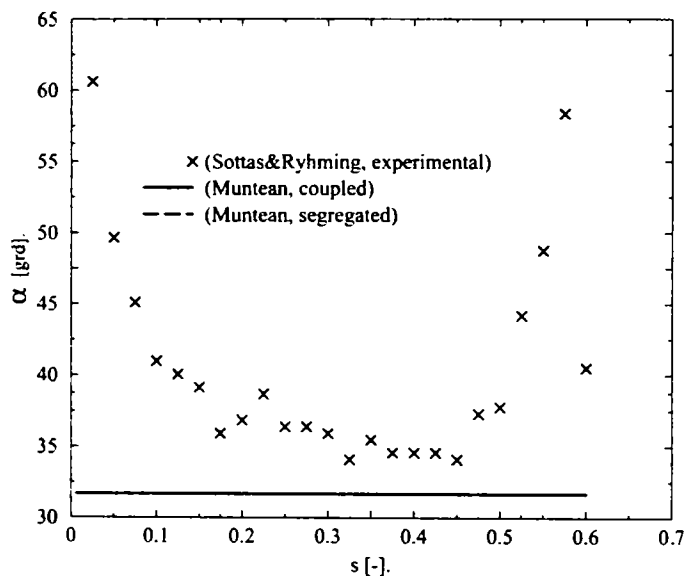


Figure 41. Flow angle on the distributor inlet axis AA' at best efficiency operating conditions P1. Imposed value and comparison with experimental data.

The chief difficulty in using the above algorithm is in transferring data from distributor to runner and vice versa. When looking at the Figure 6 and Figure 18 one can easily observe that the distributor outlet surface does not match the runner inlet surface, although both lie on the same cone segment. Moreover, the distributor has 24 blades, while the runner has only 13. The problem is even more complicated by the use of an unstructured mesh.

Assuming a steady relative runner flow implies that there is no circumferential variation in both velocity and pressure. This assumption actually neglects the unsteady interaction between guide vane wake and runner blades. However, for basic turbomachinery design this is a secondary issue.

As far as the algorithm implementation is concerned, the FLUENT code requires that a so-called *radial profile* should be provided in cylindrical coordinate system. This is a set of ordered points (e.g.  $(r_i, p_i)$ ,  $i=1...n$ ) with radius values starting at  $r_B$  and ending at  $r_B$  for the BB' axis. The above considerations led to the following procedure for processing the interface data:

- first, the numerical values (for velocity components or pressure) are plotted against the radius (measured from the turbine axis) for all mesh points on the distributor outlet or runner inlet surface;
- second, a fifth degree polynomial regression is performed, such that a best average value is obtained at each radius;
- third, for the velocity components a correction is performed such that the prescribed discharge is preserved, while the flow direction is not altered.

This approach which performs a circumferential averaging, is equivalent to the full mixing of the wakes (or any other circumferential non-uniformities), and it is known as the "*mixing interface method*". In order to implement the above algorithm, we have developed a FORTRAN code, using the IMSL library. The procedure is called at each iteration step, performing the "mixing", discharge correction, and relaxation

when transferring the velocity field from the distributor outlet to the runner inlet. When transferring the pressure field from the runner inlet to the distributor outlet, only pressure averaging is performed.

We have investigated the convergence rate for the above mixing interface algorithm. It was found that rapid convergence (within engineering requirements, i.e. less than 1% variation on average for two successive iterations) can be achieved only by employing under-relaxation,

$$p_{out\ dist}^i = (\text{relax})p_{in\ runner}^{i-1} + (1 - \text{relax}) p_{out\ dist}^{i-1}, \text{ and}$$

$$V_{in\ runner}^i = (\text{relax})V_{out\ dist}^{i-1} + (1 - \text{relax}) V_{in\ runner}^{i-1},$$

respectively. The relaxation parameter value was relax=0.3. Numerical investigations have shown that 5...7 iterations lead to an engineering acceptable convergence, provided that a good pressure distribution is used for the first distributor computation.

This *mixing interface approach* is applied first at the best efficiency operating point. The present results are compared with previous individual distributor and runner computations, as well as with the experimental results. For comparison the both distributor results D2 case (Chapter IV) and individual runner numerical results {2} case (Chapter V) are considered. Note that for all following figures, "segregated" means separate computations for either distributor or runner, while "coupled" denotes results obtained with the *mixing interface approach*. In order to avoid confusion we mention that the same appellation is used by the FLUENT code to denote two different approaches to solve the flow equations, and there is no connection at all with our approach.

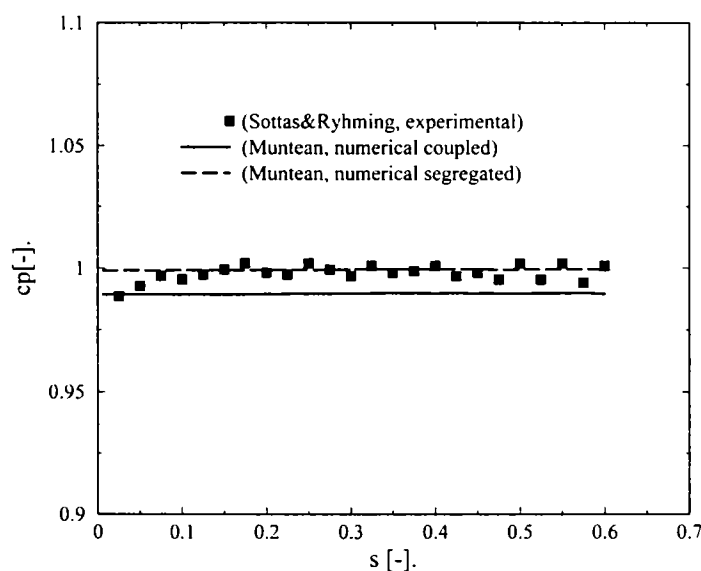


Figure 42. Pressure coefficient at the distributor inlet axis AA' at best efficiency operating conditions P1. Comparison between the experimental data and the computed results at best efficiency operating conditions P1.

Figure 42 presents the pressure coefficient on the distributor inlet axis AA'. The pressure distribution is practically constant, but the pressure level is slightly lower for the coupled approach. Since the fluid is inviscid, one should expect that the computed pressure should be lower than the measured value because the hydraulic losses are neglected. The dashed line was obtained by imposing the measured pressure distribution on the distributor outlet surface, according to the points from Figure 45. We mention once again that these data are not currently available in engineering practice.

Moreover, when computing separately the runner flow, the pressure obtained at the runner inlet is significantly different from what we have imposed at the distributor outlet. Thus, in order to obtain a continuous pressure field the above iterative coupling technique should be employed.

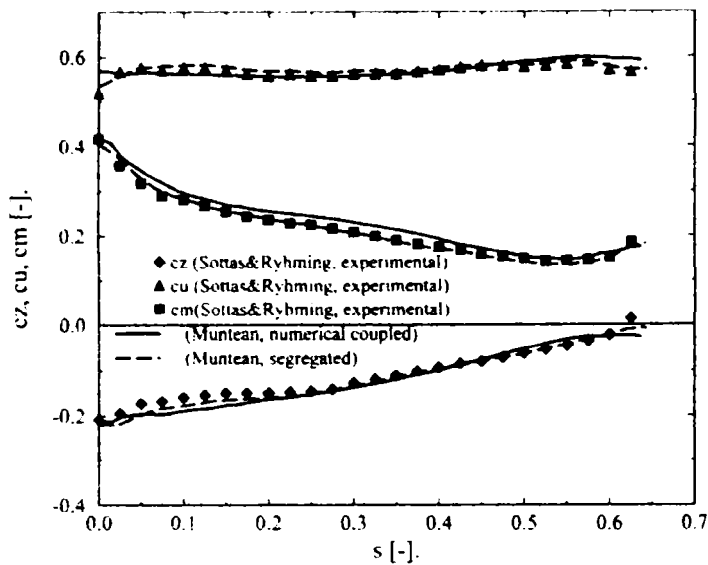


Figure 43. Velocity components at the runner inlet axis BB' at best efficiency operating conditions P1. Comparison between the experimental data, the computed results and imposed conditions.

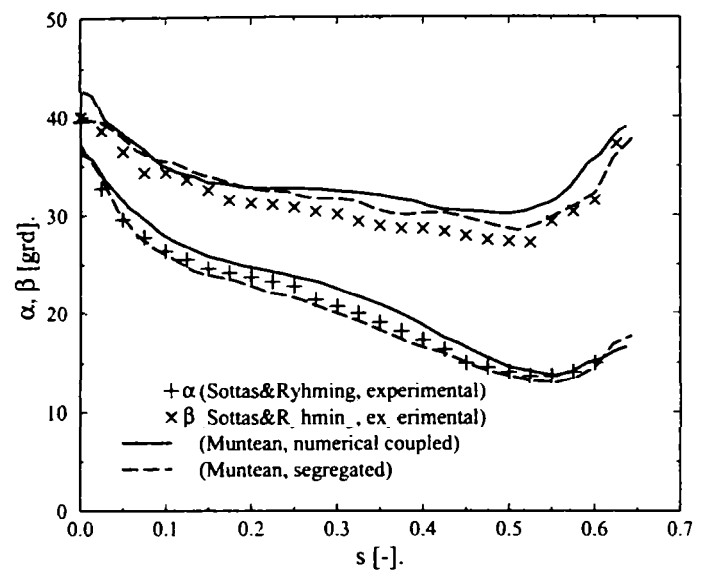


Figure 44. Flow angles at the runner inlet axis BB' at best efficiency operating conditions P1. Comparison between the experimental data, the computed results and the imposed conditions.

Figure 43 shows the velocity profile on the mixing interface BB', corresponding to the distributor outlet and runner inlet. Note here that the dashed lines are *imposed* velocity profiles (in agreement with the experiment) for the separate runner calculation. The actual computed results are presented with solid lines, and an excellent agreement with experimental data is observed. The same conclusion can be drawn from Figure 44, where the absolute and relative flow angles are correctly predicted. This is important, since correct runner results heavily rely on accurate inflow conditions.

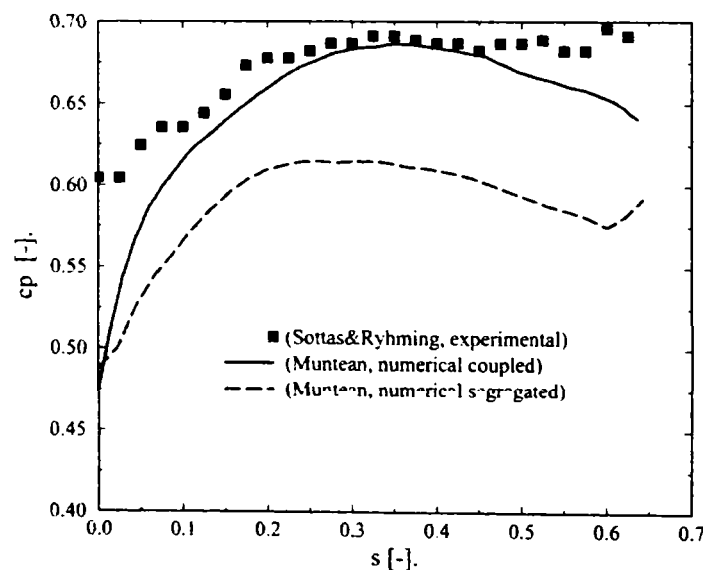


Figure 45. Pressure coefficient on the runner inlet axis BB' at best efficiency operating conditions P1. Comparison between the experimental data and the computed results.

Figure 45 presents the pressure distribution on the mixing interface. The numerical results are taken from the runner inlet, since the pressure is a prescribed boundary condition at distributor outlet. One can easily observe that a separate runner computation, even with a relatively good inlet velocity field, leads to 20% error in pressure level. The coupled computation, solid line, not only eliminates the pressure discontinuity at the mixing interface, but also produces much better results in agreement with experimental data.

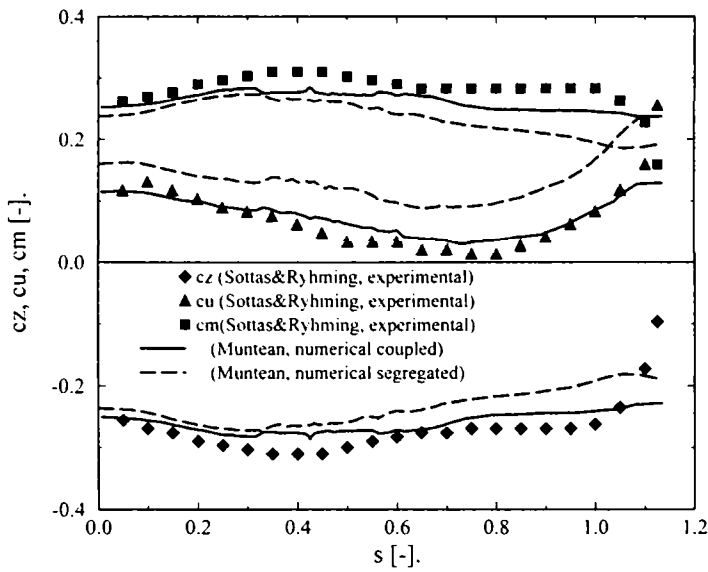


Figure 46. Velocity components at the runner outlet axis CC' at best efficiency operating conditions P1. Comparison between the experimental data and the computed results.

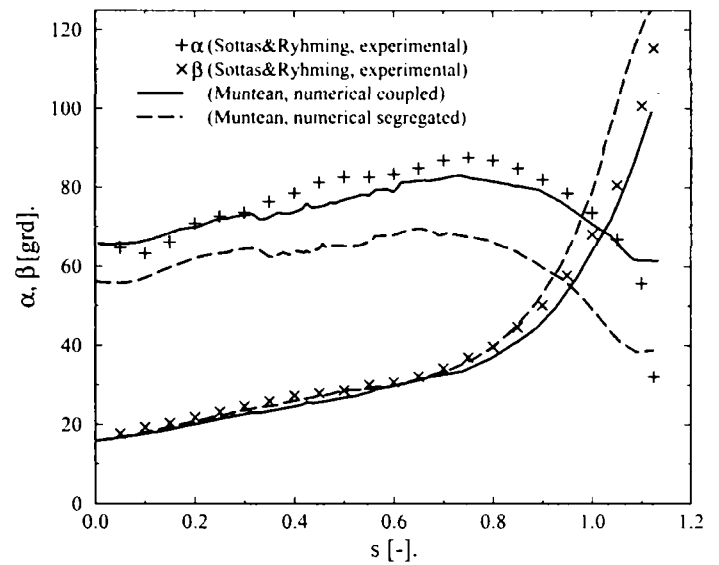


Figure 47. Flow angles at the runner outlet axis CC' at best efficiency operating conditions P1. Comparison between the experimental data and the computed results.

Figure 46 shows the velocity field right after the runner blades, on the survey axis CC'. One can see that the coupling iterative method leads to an excellent agreement with experimental data. The separate runner computation does not predict correctly the level of tangential velocity, thus the swirl after the runner blades is larger and the energy taken by the runner from the flow is under-predicted.

The flow direction, in terms of absolute ( $\alpha$ ) and relative,  $\beta$ , flow angles the runner blades is presented in Figure 47. Both absolute and relative flow directions are correctly predicted by the coupled computation. In contrast, the separate runner computation significantly underestimates the absolute flow angle, especially in the crown neighborhood. This region is particularly important when partial discharge operating points are investigated, since this is where reverse flows are initiated.

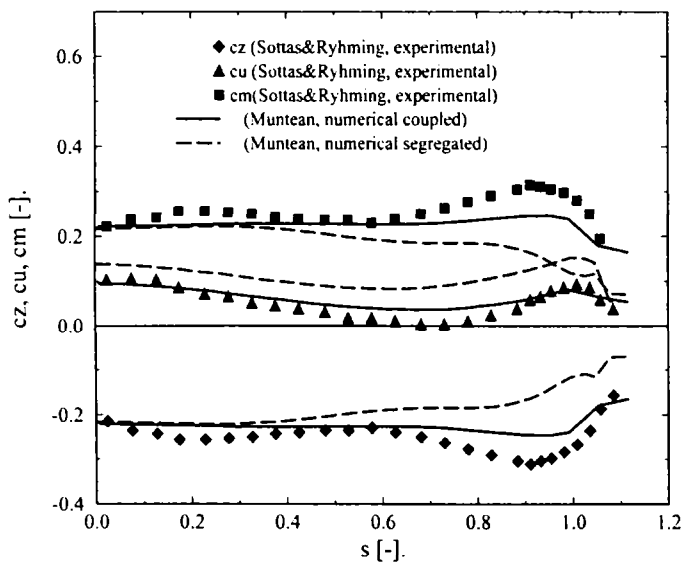


Figure 48. Velocity components at the draft tube inlet axis DD' at best efficiency operating conditions P1. Comparison between the experimental data and the computed results.

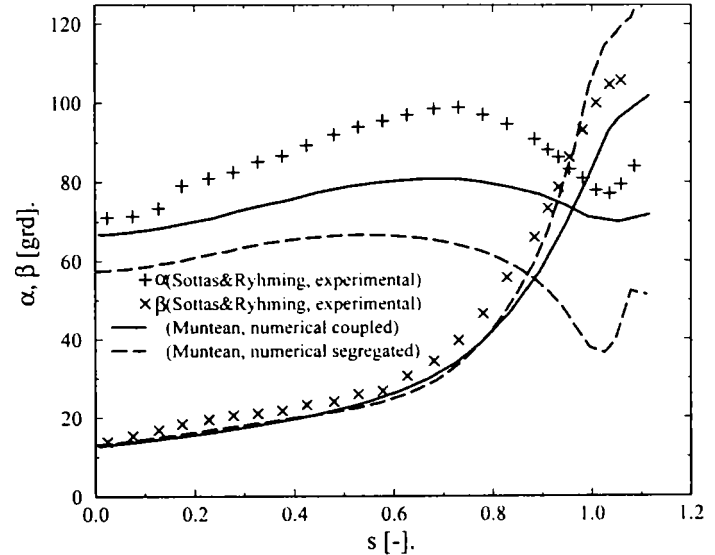


Figure 49. Flow angles at the draft tube inlet axis DD' at best efficiency operating conditions P1. Comparison between the experimental data and the computed results.

The velocity field on the draft tube inlet is presented in Figure 48. All velocity components are better predicted by the coupled computation, especially near the turbine axis. Once again, the separate runner computation predicts a large swirl, in disagreement with the experiment. The coupled computation correctly predicts the tangential velocity, and produces a significant improvement in axial and meridian velocity components near the turbine axis. This is clearly shown in the flow direction, presented in Figure 49. Since the draft tube flow, and ultimately the pressure recovery coefficient, depends on the amount of swirl after the runner, one can see that the coupled computation significantly improves the absolute flow



direction predictions. Note that these good results are also due to the radial equilibrium outlet condition employed on the runner domain outlet. The pressure distribution on the DD' axis is shown in Figure 50. The coupled results are in excellent agreement with the experiment, while the separate computation predicts a much larger pressure drop near the turbine axis, despite using the same boundary condition.

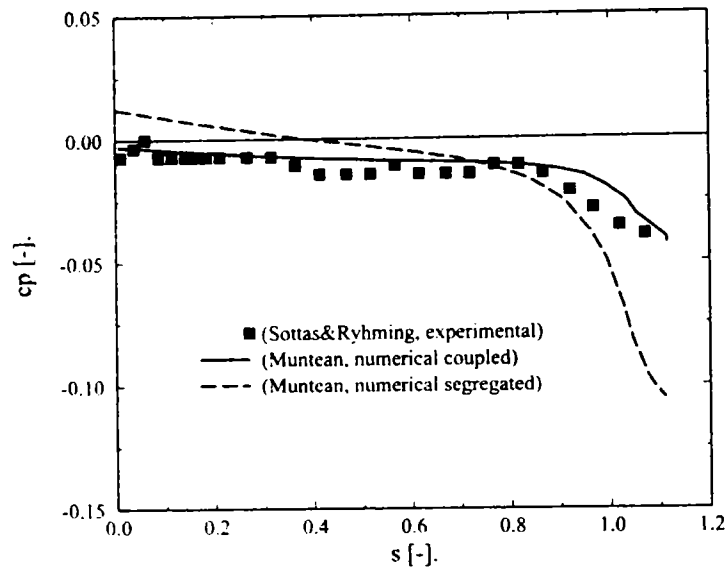


Figure 50. Pressure coefficient at the draft tube inlet axis DD' at best efficiency operating conditions P1. Comparison between the experimental data and the computed results.

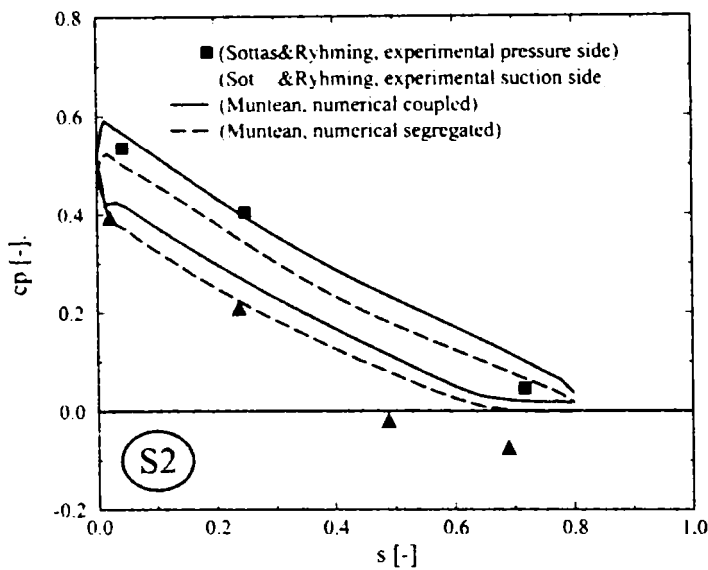


Figure 51. Pressure distribution on the S2 section of the runner blade at best efficiency operating conditions P1. Comparison between the experimental data and the computed results.

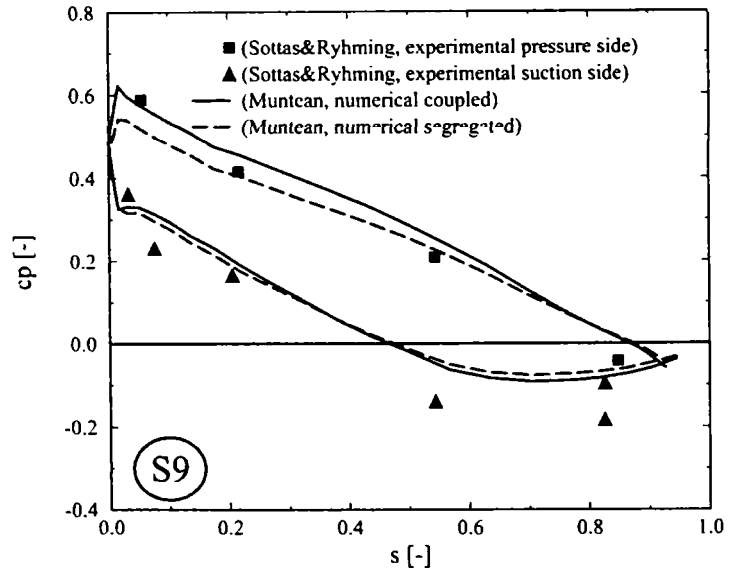


Figure 52. Pressure distribution on the S9 section of the runner blade at best efficiency operating conditions P1. Comparison between the experimental data and the computed results.

To conclude the study at best efficiency operating point, we investigate the pressure distribution on the runner blade. Near the crown, S2 section from Figure 2, one can see in Figure 51 that both methods give reasonable results on the pressure side, while failing to predict the minimum pressure on the suction side, near the trailing edge. However, the coupled approach predicts a slightly higher level on the S2 than the separate runner computation. Figure 52 presents the pressure on the mid section S9. There are no differences between the two methods on the suction side, while the coupled method gives better results on the pressure side, near the trailing edge.

Results for the section, near the band, are presented in Figure 53. The coupled method is closer to the experiment on the suction side, but still fails to reach the measured minimum pressure level. However, this is a general observation for computations performed by various research groups, and at some point one may question here the accuracy of the experimental data.

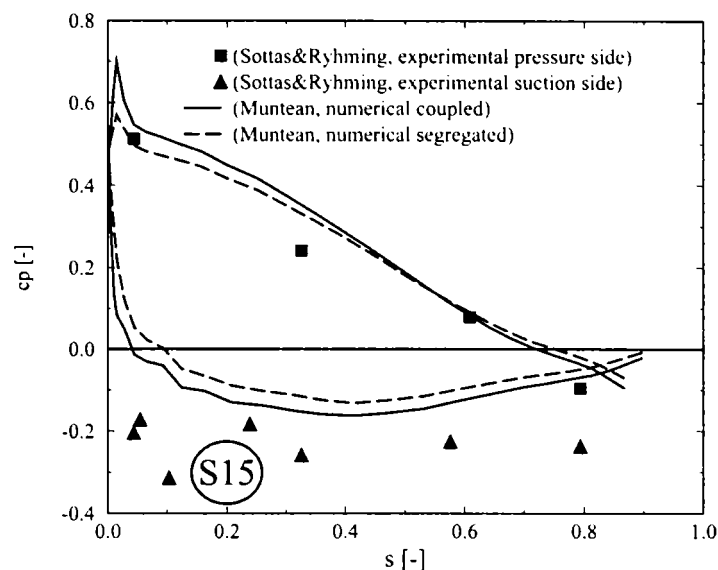


Figure 53. Pressure distribution on the S15 section of the runner blade at best efficiency operating conditions P1. Comparison between the experimental data and the computed results.

In conclusion, the above analysis at best efficiency operating point shows that coupling the distributor and runner hydrodynamic fields leads to more accurate numerical results, i.e. in better agreement with measurements. Moreover, although the *mixing interface approach* introduces additional simplifications in the flow model, the numerical results are quite satisfactory from a practical engineering viewpoint.

We investigate next the Francis turbine flow at off-design operating conditions, and we assess the capability of our numerical methodology to make correct predictions in this situation. In conjunction with the best efficiency point measurements made for the GAMM workshop, some off-design measurements were done. These measurements were not available at the workshop but were used in work by Gros et al. (1998) to compare the computational results of the TASCFlow and N3S commercial codes with measurements. These computational results and experimental data are used for comparison with our numerical results. We consider here the same off-design operating points as did Gros et al. (1998) (off-design operating conditions marked P2, P3, P4 and P5). Moreover, the GAMM Francis runner is also used for the ERCOFTAC workshop, where the measurements are made at somewhat different operating conditions. Therefore, the computational results in conjunction with the experimental data are available from the GAMM workshop in the paper by Cobut et al. (1996) (off-design operating conditions indicated by P6 and P7). In addition, we considered other two off-design operating points denoted by P8 and P9. All off-design operating points are presented on the GAMM Francis turbine hill chart, Figure 54.

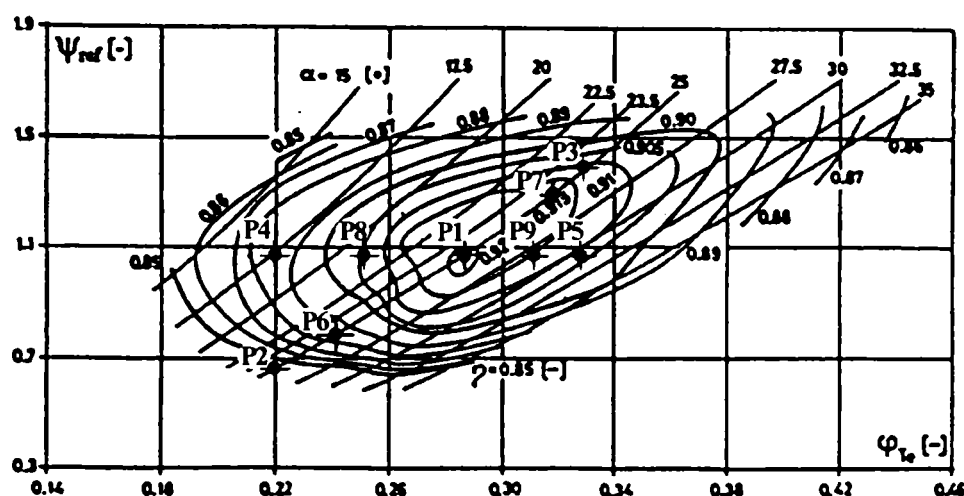


Figure 54. Off-design operating points for the GAMM Francis turbine. P4, P8, P1, P9, and P5 correspond to the optimum constant energy and variable discharge, while P2, P6, P1, P7, and P3 correspond to constant guide vane opening and variable discharge.

The numerical results for each off-design operating conditions at constant guide vane opening will be presented here, while the numerical results for off-design operating conditions at constant energy are not present here (see the PhD thesis).

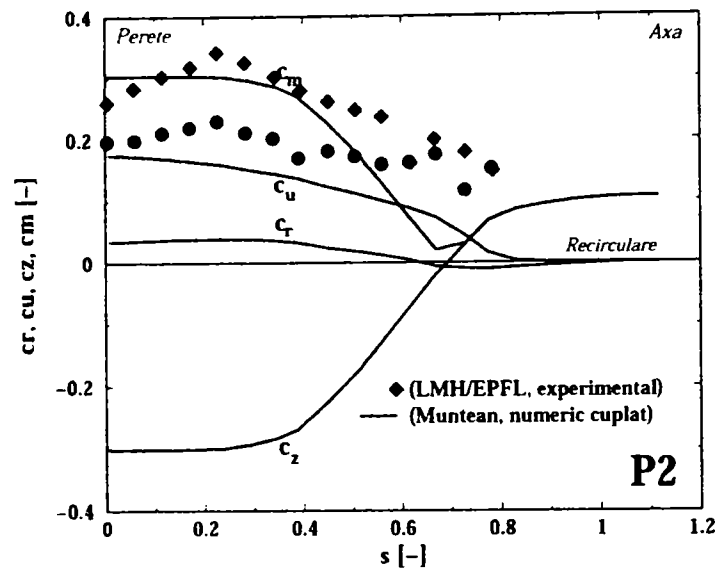


Figure 55. Velocity coefficients (radial  $c_r$ , tangential  $c_u$ , axial  $c_z$ , meridian  $c_m$ ) on the draft tube inlet section at P2 off-design operation point. Comparison between the experimental data (LMH/EPFL  $c_m$   $\blacklozenge$ ,  $c_u$   $\bullet$ ) and coupled numerical results (Muntean).

Let us examine the flow velocity field on the draft tube inlet, where a drop in the flow rate (partial discharge) produces a recirculation zone near the machine axis. We therefore test the ability of our methodology (and particularly the radial equilibrium boundary condition) to predict recirculating flows.

The velocity components on the draft tube inlet section at P2 off-design operation conditions are presented in Figure 55. The velocity components are reasonable predicted near to the wall. We imposed the radial equilibrium boundary condition on this section and the axial component of the velocity predicts a recirculation region. Moreover, both velocity components (the radial and tangential components) are zero in that region. Actually, the flow beneath the crown, close to the axis of rotation, presents a recirculation zone where there are no measurements available. Because of the recirculation, the flow is strongly transient in this region and stationary computations should fail to predict the flow since no steady solution exists. This phenomenon was experimentally visualized as a cavitating vortex rope.

Comparison between our computed results and the numerical results obtained by Gros et al. (1998) on the draft tube inlet section are presented in Figure 56 and Figure 57. One can observed that a reasonable concordance between our numerical results and the numerical results computed by Gros et al. (1998) with TASCFlow code against experimental data, especially the outer part of the draft tube inlet axis. The numerical results computed by Gros et al. (1998) with N3S code fail to predict the flow recirculation.



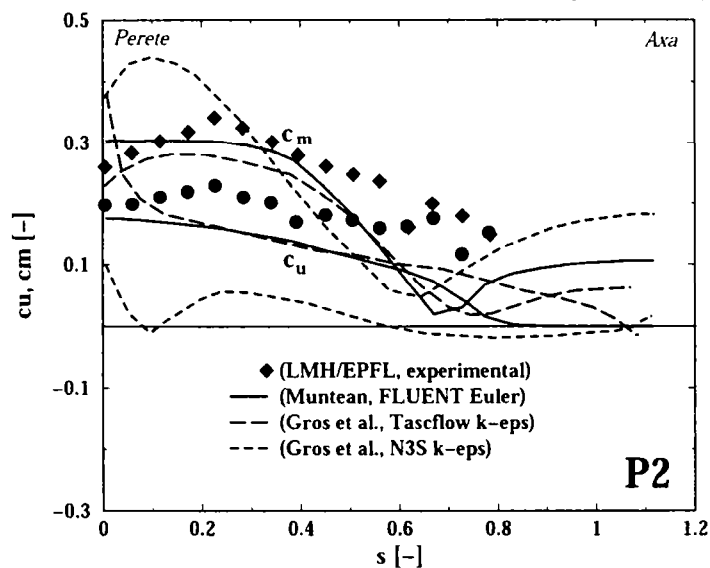


Figure 56. Velocity coefficients (tangential  $c_u$ , meridian  $c_m$ ) on the draft tube inlet section at P2 off-design operation point. Comparison between the experimental data from LMH/EPFL ( $\diamond$ ,  $\bullet$ ), coupled numerical results (Muntean) and other numerical results Gros et al. (1998).

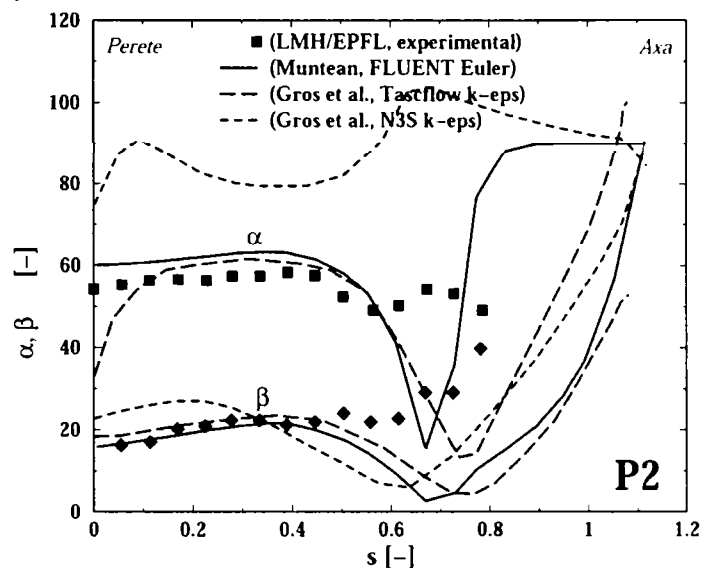


Figure 57. Absolute ( $\alpha$ ) and relative ( $\beta$ ) flow angles on the draft tube inlet section at P2 off-design operation point. Comparison between the experimental data from LMH/EPFL ( $\square$ ,  $\diamond$ ), the coupled numerical results (Muntean) and other numerical results Gros et al. (1998).

The same conclusions can be drawn from Figure 58 and Figure 59, where the velocity components and flow angles are computed on the draft tube inlet at P6 operating condition. Because the discharge is increased but still remains under the optimum value ( $0.85Q_{opt}$ ) the recirculation region is smaller. Consequently, our numerical results present a very good agreement against experimental data, except the recirculation region. The numerical results obtained by Cobut et al. (1996) with Sagarmatha code correspond with our results.

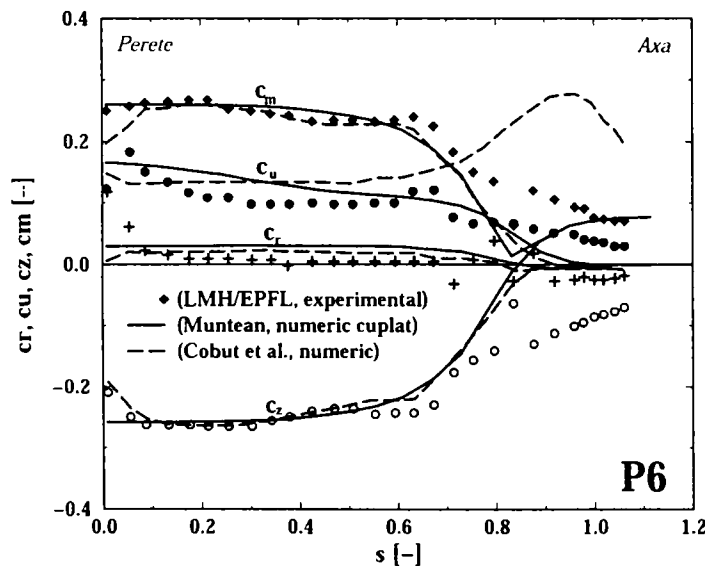


Figure 58. Velocity coefficients (radial  $c_r$ , tangential  $c_u$ , axial  $c_z$ , meridian  $c_m$ ) on the draft tube inlet section at P6 off-design operation point. Comparison between the experimental data from LMH/EPFL ( $+$ ,  $\bullet$ ,  $\circ$ ,  $\diamond$ ) and coupled numerical results (Muntean) and other numerical results Cobut et al. (1996).

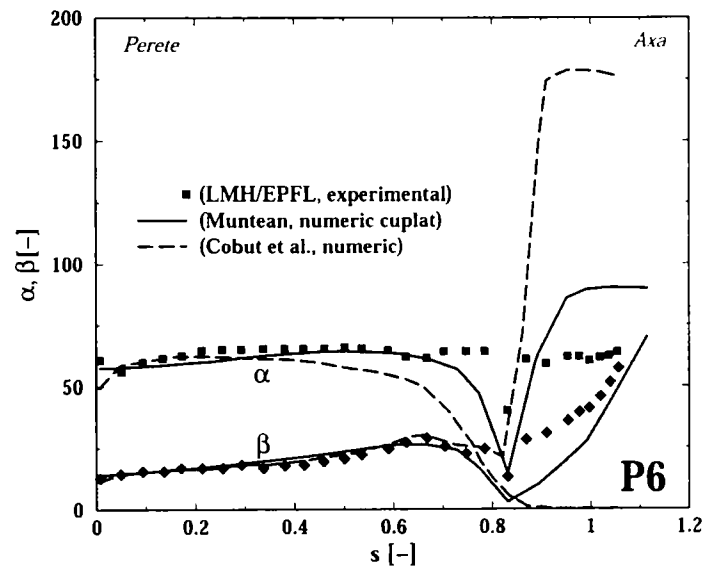


Figure 59. Absolute ( $\alpha$ ) and relative ( $\beta$ ) flow angles on the draft tube inlet section at P6 off-design operation point. Comparison between the experimental data from LMH/EPFL ( $\square$ ,  $\diamond$ ), the coupled numerical results (Muntean) and other numerical results Cobut et al. (1996).

Increasing the flow rate above the nominal value eliminates the recirculation on the draft tube inlet. As a result, the numerical results obtained for full load operating conditions show a good agreement with measurements. This conclusion is supported by Figure 60 and Figure 61 at P7 operating conditions and Figure 62 and Figure 63 at P3 operating conditions.

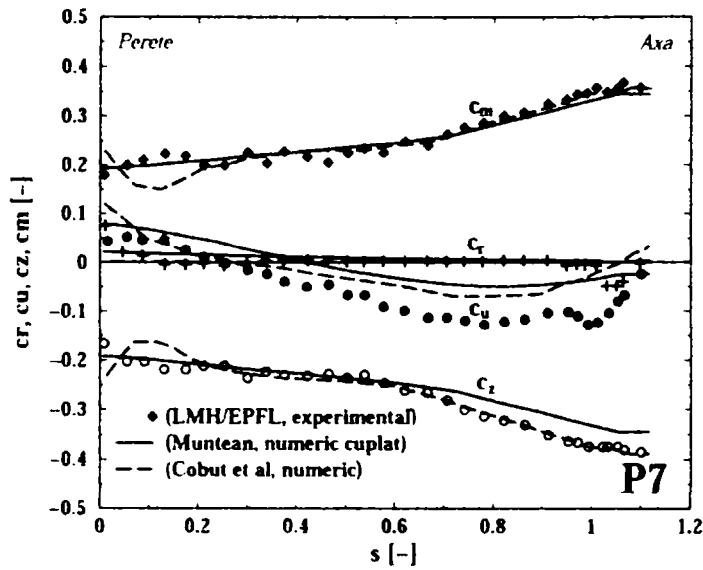


Figure 60. Velocity coefficients (radial  $c_r$ , tangential  $c_u$ , axial  $c_z$ , meridian  $c_m$ ) on the runner inlet section at P7 off-design operation point. Comparison between the experimental data from LMH/EPFL (+, ●, ○, ◆) and coupled numerical results (Muntean) and other numerical results Cobut et al. (1996).

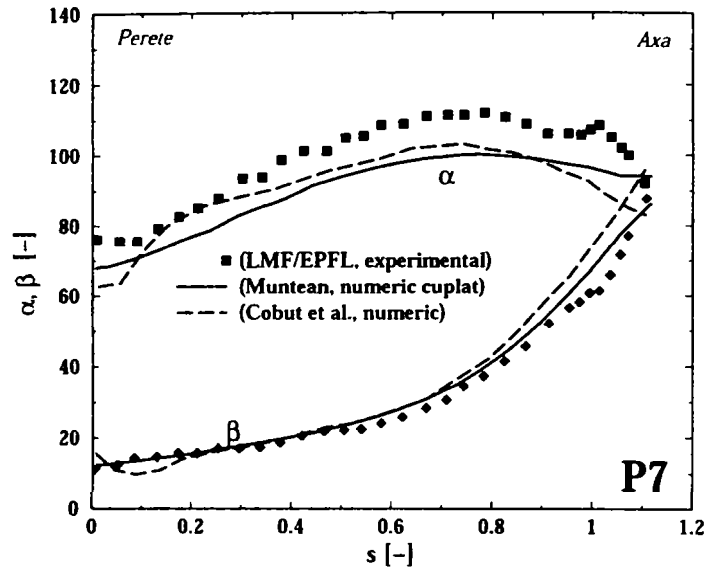


Figure 61. Absolute ( $\alpha$ ) and relative ( $\beta$ ) flow angles on the draft tube inlet section at P7 off-design operation point. Comparison between the experimental data from LMH/EPFL (■, ◆), coupled numerical results (Muntean) and other numerical results Cobut et al. (1996).

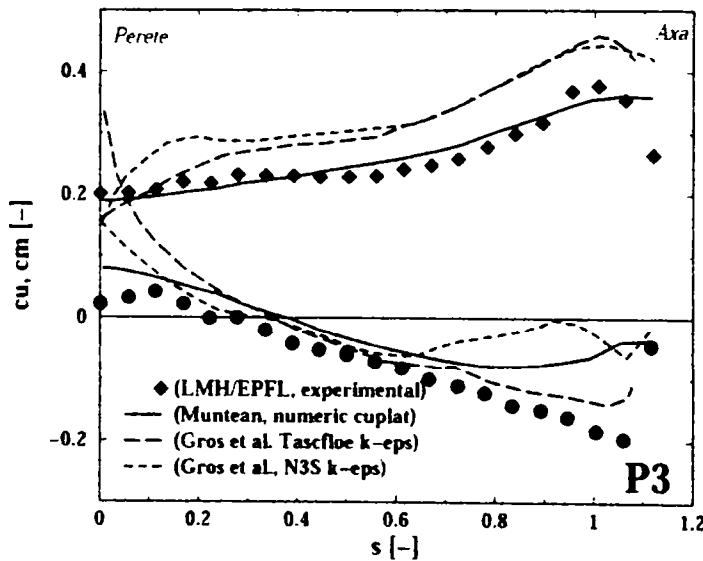


Figure 62. Velocity coefficients (tangential  $c_u$ , meridian  $c_m$ ) on the draft tube inlet section at P2 off-design operation point. Comparison between the experimental data from LMH/EPFL (◆, ●), coupled numerical results (Muntean) and other numerical results Gros et al. (1998).

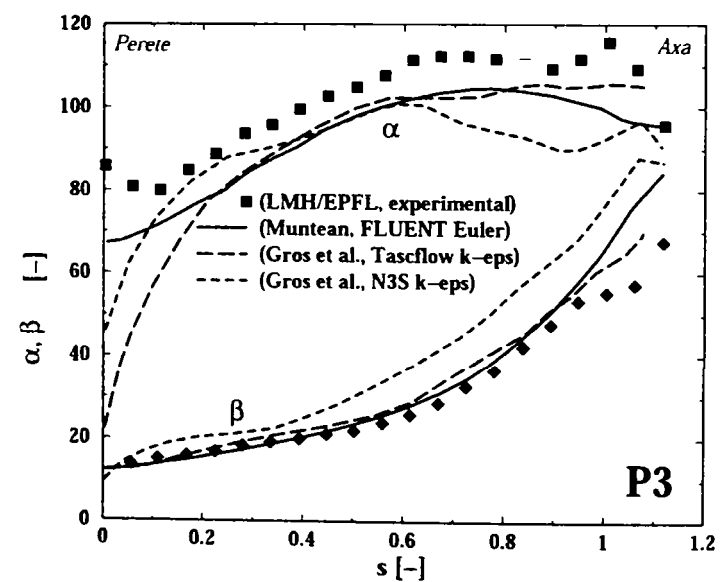


Figure 63. Absolute ( $\alpha$ ) and relative ( $\beta$ ) flow angles on the draft tube inlet section at P2 off-design operation point. Comparison between the experimental data from LMH/EPFL (■, ◆), coupled numerical results (Muntean) and other numerical results Gros et al. (1998).

We have restricted the above argument to the velocity field on the draft tube inlet section, since this is the Achilles' heel of the numerical simulation due to the occurrence of recirculation for smaller discharge than the nominal value. The lack of suitable "traditional" boundary conditions is solved by employing the radial equilibrium condition, which proved to be able to deal with recirculating flows. However, the velocity field is not itself the primary concern for the engineer. A more useful analysis is concerned with the pressure distribution on the runner blade.

The pressure coefficient distribution on the S2, S9, S15 sections (Figure 2) of the Francis runner blade at five constant guide vane openings (P2 -  $0.77Q_{opt}$ , P6 -  $0.85Q_{opt}$ , P1 -  $Q_{opt}$ , P7 -  $1.12Q_{opt}$ , P3 -  $1.17Q_{opt}$ ) is investigated. These distributions show the behavior of the flow around the runner blade for several off-design operating conditions. Moreover, the stagnation point and acceleration/deceleration of the flow around the runner blade is examined.

Figure 64 presents pressure coefficient on the S2 section of the runner blade for five operating conditions at constant guide vane opening ( $P2 - 0.77Q_{opt}$ ,  $P6 - 0.85Q_{opt}$ ,  $P1 - Q_{opt}$ ,  $P7 - 1.12Q_{opt}$  and  $P3 - 1.17Q_{opt}$ ). At P2 operating point (blue solid line), the leading edge stagnation point is located on the suction side of the runner blade. Consequently, the flow accelerates as the flow particle goes around the leading edge. At P6 operating point (black dashed line), the stagnation point is practically located at the leading edge of the runner blade. Accordingly, a smooth flow on the both sides (the pressure and suction side) is observed. The other operating points, P1 (red solid line), P7 (long dashed line) and P3 (green solid line), have the stagnation point on the pressure side of the blade. The migration of the stagnation point from the suction side to the pressure side as the flow rate increases is consistent with the relative flow angle of attack variation as the discharge is modified. Large angle of attack values results in flow detachment (and possible reattachment) on the runner blade suction side. This secondary flow region grows up as the discharge gets larger.

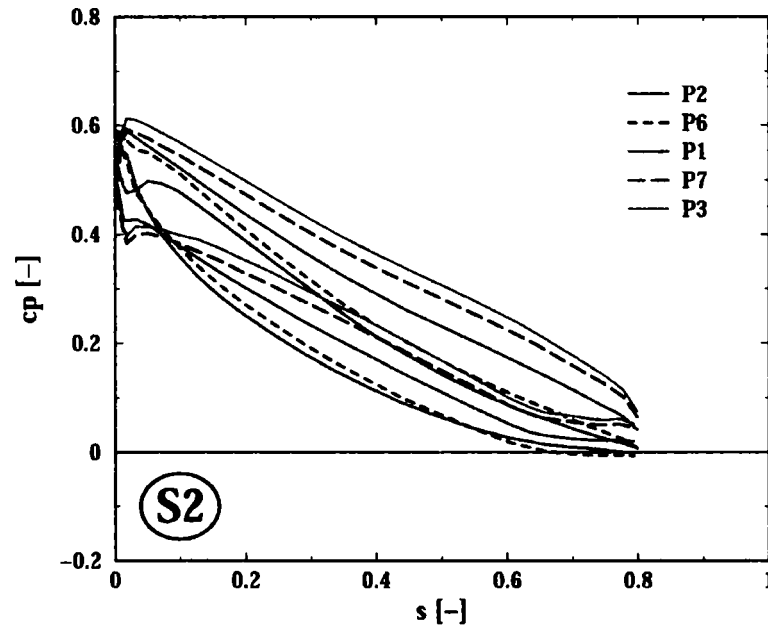


Figure 64. Pressure coefficient distribution on the S2 runner blade section at five constant guide vane openings ( $P2 - 0.77Q_{opt}$ ,  $P6 - 0.85Q_{opt}$ ,  $P1 - Q_{opt}$ ,  $P7 - 1.12Q_{opt}$ ,  $P3 - 1.17Q_{opt}$ ).

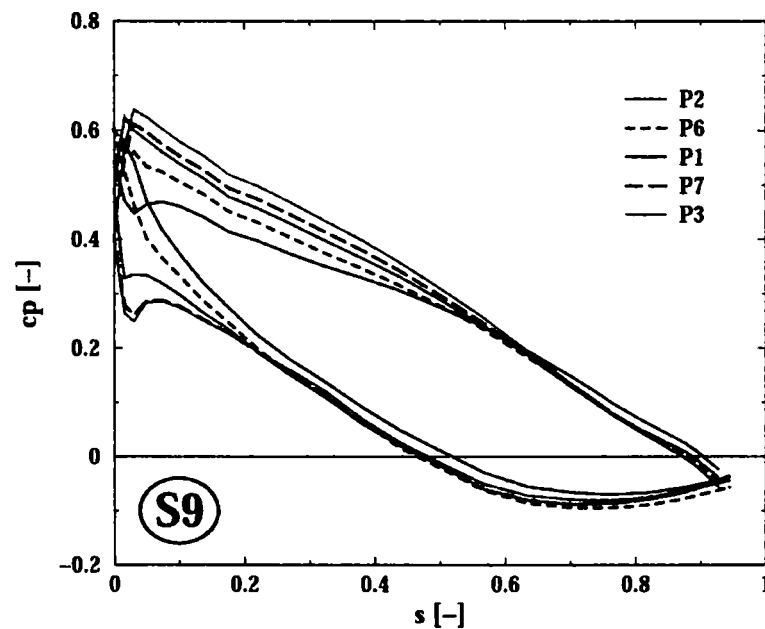


Figure 65. Pressure coefficient distribution on the S9 runner blade section at five constant guide vane openings ( $P2 - 0.77Q_{opt}$ ,  $P6 - 0.85Q_{opt}$ ,  $P1 - Q_{opt}$ ,  $P7 - 1.12Q_{opt}$ ,  $P3 - 1.17Q_{opt}$ ).

The same conclusions can be drawn from Figure 65, where the pressure coefficient is computed on the S9 section of the runner blade for the five constant guide vane opening ( $P2 - 0.77Q_{opt}$ ,  $P6 - 0.85Q_{opt}$ ,  $P1 - Q_{opt}$ ,  $P7 - 1.12Q_{opt}$ ,  $P3 - 1.17Q_{opt}$ ). However, the pressure coefficient becomes negative on the second half of the suction side (near the trailing edge).

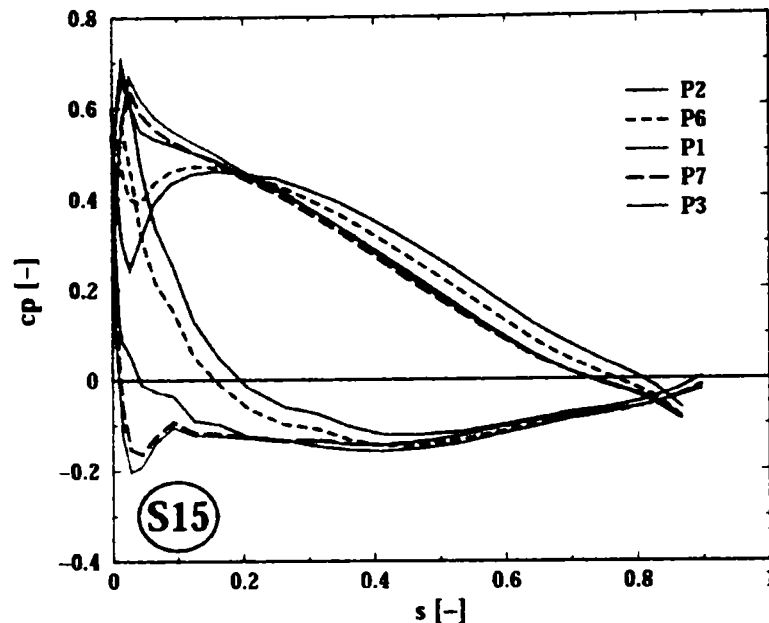


Figure 66. Pressure coefficient distribution on the S15 runner blade section at five constant guide vane openings (P2 -  $0.77Q_{opt}$ , P6 -  $0.85Q_{opt}$ , P1 -  $Q_{opt}$ , P7 -  $1.12Q_{opt}$ , P3 -  $1.17Q_{opt}$ ).

The pressure coefficient distribution on the S15 section of the runner blade at five constant guide vane openings (P2 -  $0.77Q_{opt}$ , P6 -  $0.85Q_{opt}$ , P1 -  $Q_{opt}$ , P7 -  $1.12Q_{opt}$ , P3 -  $1.17Q_{opt}$ ), Figure 66 displays a significant change relative to S2 and S9 sections. Negative pressure coefficients are present on three quarters of the suction side for partial discharge, but for larger discharge the pressure coefficient becomes negative on the whole suction side. As a result, S15 section (near the runner band) is the most susceptible for cavitation inception and development.

In conclusion, a methodology for computing the three-dimensional flow through the Francis turbine runner at variable operating point is presented. Due to the current limitations in computer hardware the 3D flow computation is performed in two domains, corresponding to the distributor and runner channels. Consequently, a distributor-runner flow coupling technique based on *mixing interface method* is developed. On the domains interface, a special technique is employed to eliminate the circumferential variation in both velocity and pressure fields, thus the name of the method. The iterative coupling technique takes successively the distributor outlet velocity as inflow condition for the runner, and the computed runner inlet pressure as outlet pressure condition for the distributor. The stopping criterion is chosen for the pressure on the mixing interface.

The main advantage of computing the flow through the distributor-runner turbine is that only the velocity distribution at the distributor inlet (usually taken as a constant velocity profile corresponding to the spiral case outlet) needs to be known. This is particularly important for practical engineering applications since no velocity and/or pressure measurements are usually performed for turbine models.

The radial equilibrium condition employed at the runner outlet /draft tube inlet section is found to be the best choice in order to avoid spurious back flow after the runner. In addition, this condition performs very well for variable discharge, being able to deal with recirculating flows as well.

Extensive comparison of our numerical results with experimental data is performed, in order to validate and assess the accuracy of the numerical method. As a first conclusion, it seems that the inviscid flow model is suitable for computing the 3D hydraulic turbine flow at and around the best efficiency operating point. Comparison with velocity and pressure profiles on the four surveys axes show an excellent agreement of the coupled computations with experiments. On the other hand, computing separately the flow in the distributor / runner not only requires experimental data which are not currently available but also lead to poor predictions especially after the runner blades and at the draft tube inlet.

We can firmly state that the numerical methodology developed in this chapter is a reliable and efficient way to compute 3D turbomachinery flows. It can be easily employed for design and optimization investigation, once a 3D inviscid flow solver (e.g. the FLUENT commercial CFD code) is available.

## 8. Theoretical Determination of the Energetic and Cavitation Characteristics for Francis Turbines

This chapter employs the methodology developed in this work for computing the 3D flow in Francis turbines to evaluate both the efficiency and cavitation inception characteristics. Although the present results are obtained for an inviscid fluid, the turbine efficiency can be defined such that we obtain a good agreement with measured values. As far as the cavitation inception is concerned, the inviscid flow calculation correctly predicts both the corresponding cavitation coefficient and the location where the relevant cavitation occurs. Our computations take into account only the turbine distributor and runner, thus the draft tube hydrodynamic characteristics are taken into account using available experimental data, Kubota et al. (1996).

### Hydraulic efficiency

The turbine efficiency  $(\eta^*)_x$ , defined according to the IEC standards, is computed using the following relationship:

$$(\eta^*)_x = \frac{(M_h)_x \cdot \omega}{\rho Q_x (E)_x} [-],$$

where  $M_h$  is the hydraulic torque,  $\omega$  is the angular velocity,  $Q$  is the discharge and  $E$  is the specific turbine energy between the inlet of the turbine and the draft tube outlet section. The index  $( )_x$  denotes variable operating points.

In order to evaluate the efficiency and compare it with experimental data from Figure 4 (up), we first evaluate the hydraulic torque. Using the numerical methodology presented in the previous chapter, the three-dimensional pressure distribution on one runner blade is obtained. Using a numerical integration procedure, we obtain for one blade,

$$(M'_h)_x = \left[ \left( \sum_i p_i r_i \times n_i \Delta s_i \right) \cdot i_z \right]_x \text{ [Nm]}$$

where  $p$  is the static pressure,  $\mathbf{n}$  the normal vector to the runner blade,  $r$  the position vector,  $\Delta s$  the elementary area and  $( )_i$  is the index for a node on the blade surface. The runner hydraulic torque is found by multiplying  $(M'_h)_x$  with the number of blades  $Z$  (for the GAMM Francis runner  $Z=13$ ).

$$(M_h)_x = Z \cdot (M'_h)_x \text{ [N.m]}$$

Since we have employed an inviscid flow model it is useful to check the accuracy of the computed hydraulic torque. The comparison numerical-experimental is performed by using the runner torque coefficient  $(c_M)_x$ ,

$$(c_M)_x = \frac{2 \cdot (M_h)_x}{\rho \pi \omega^2 R_{ref}^5} [-]$$

Figure 68 presents the torque coefficient  $(c_M)_x$  versus discharge coefficient  $(\phi)$  at constant guide vane opening for the GAMM Francis runner. The experimental data are obtained at LMH-EPFL and are marked by points • Sottas & Ryhming (1993), ■ Cobut et al. (1996). Our numerical results are computed using coupled technique presented in Chapter VII and are labeled by *(Muntean, numeric cuplat)*. One can observe a very good agreement between our numerical results and experimental data. Consequently, the coupled technique accurately predicts the global parameters of the Francis runner (i.e. torque coefficient) for a whole range of the operating conditions, provided that the correct discharge value is used in computations.



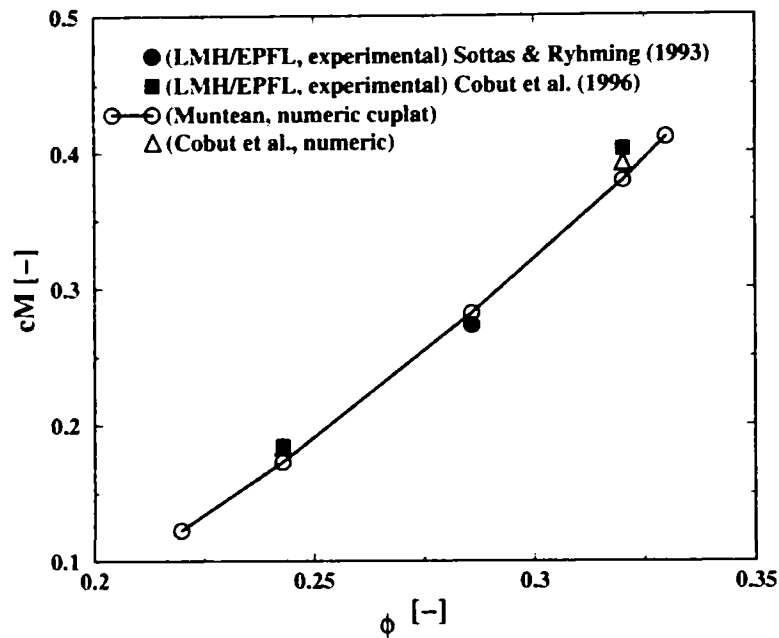


Figure 67 Runner torque coefficient  $(c_M)_x$  versus discharge coefficient  $(\phi)$  at constant guide vane opening ( $\alpha \approx 25^\circ$ ) for GAMM Francis turbine. Comparison between the experimental data from Sottas & Ryhming (1993), Cobut et al. (1996) (LMH/EPFL  $\bullet, \blacksquare$ ), coupled numerical results (Muntean) and other numerical results Cobut et al. (1996).

Once the hydraulic torque computed, one should evaluate the turbine specific energy  $E$ . This is the chief difficulty here, for two main reasons. First, we compute the flow only through the distributor and runner. Second, the flow is considered inviscid. Let us address these two issues separately.

When considering the energy between distributor inlet and draft tube inlet sections  $E_{ref}$ , one can define a *special* efficiency,

$$(\eta)_x = \frac{(M_h)_x \cdot \omega}{\rho Q_x (E_{ref})_x} [-].$$

This definition was used for the special hill chart from Figure 4 (down). However, one would expect this efficiency to be 100% since an inviscid flow is computed and there are no hydraulic losses. An ingenious trick can be employed (although not completely rigorous) to define less than 100% efficiency. Theoretically, the energy should be defined by considering two flow sections with uniform velocity and pressure fields. The distributor inlet section agrees with this requirement, but the draft tube inlet does not. After the flow leaves the runner there is a certain amount of swirl, as well as a radial distribution for both axial velocity and pressure. Conventionally we consider for the energy evaluation the average velocity (discharge / draft tube inlet area) and the pressure value at the wall. As a result, the above definition for the special efficiency produces values smaller than 100% since the extra kinetic energy due to the swirl and axial velocity non-uniformity is not taken into account. This special efficiency can be evaluated using our methodology for computing the distributor-runner 3D flow.

The energy  $E_{ref}$  does not take into consideration the spiral case and the draft tube. Generally, the spiral case has an accelerated flow with small hydraulic losses compared to the draft tube where the flow is decelerated and the hydraulic losses are very important. As a result, we take into account only the draft tube efficiency in order to relate the special efficiency with the whole turbine efficiency (as defined by the IEC standard),

$$(\eta^*)_x = \frac{(c_M)_x}{\phi_x (\psi_{ref} + \zeta_D \phi^2 - corr)_x},$$

where  $\zeta_D$  represents the draft tube hydraulic losses coefficient introduced by Kubota et al. (1996) and presented in Figure 68, and *corr* is defined by Kubota as a correction which accounts for the swirl energy and wall pressure rise on the draft tube inlet section. In a nutshell, given the discharge coefficient  $\phi$  and the guide vane opening, we compute  $\psi_{ref}$  and  $c_M$ , then using  $\zeta_D$  as well we evaluate the turbine efficiency.

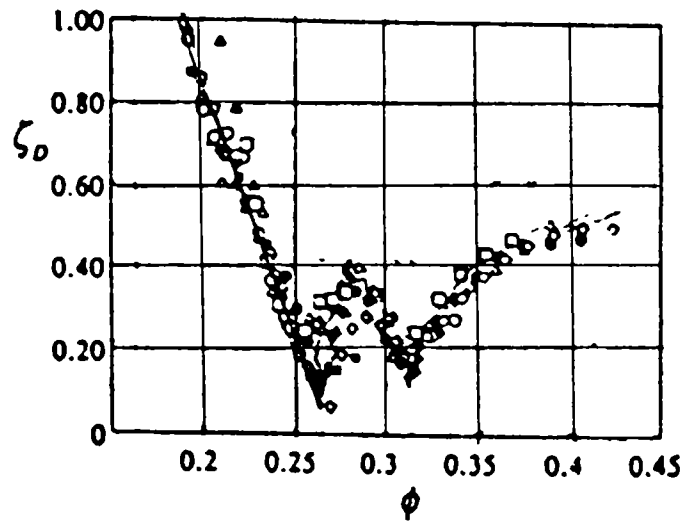


Figure 68 Hydraulic loss coefficient  $\zeta_D$  on the GAMM Francis turbine draft tube, Kubota et al. (1996).

Figure 69 shows a comparison between the GAMM Francis turbine efficiency computed with the above formula (including  $\zeta_D$  from Figure 68) and experimental values. An excellent agreement is obtained, taking into account the approximations employed. However, we mention once again that the computed results include here experimental data for the draft tube since the draft tube flow was not computed.

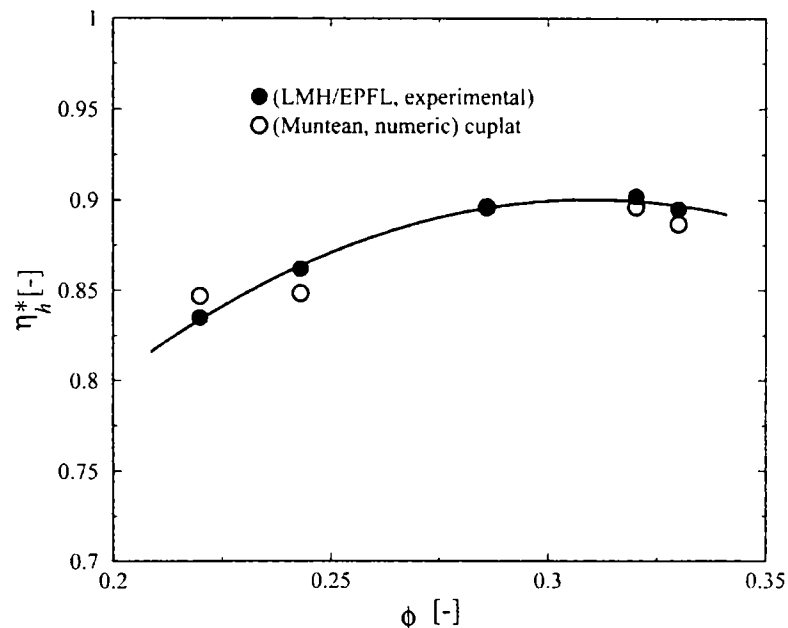


Figure 69 IEC efficiency  $(\eta^*)_h$  versus discharge coefficient  $(\phi)$  at constant guide vane opening ( $\alpha \approx 25^\circ$ ) for GAMM Francis runner. Comparison between the experimental data from Sottas & Ryhming (1993), (LMH/EPFL  $\bullet$ ) and numerical results (Muntean).

### Cavitation inception

Among all the aspects of machine operation, cavitation development plays a fundamental role with respect to the possible alteration of the efficiency and to the erosion risk. Indeed, it is economically preferable to have a cavitation free operation as long as the efficiency is unaffected and the erosion is limited. This explains why the cavitation inception problem receives greater attention in the case of hydraulic machines. Standard cavitation tests consist of investigating the influence of cavitation development on the hydraulic machine and in evaluating the erosion risk. These investigations are very important for the evaluation of the setting level of the machine to the tail-water level. These tests are performed for different operating points by investigating the influence of the Thoma number on the efficiency for variable discharge.

The Thoma number (the plant cavitation coefficient)  $\sigma_{pl}$  depends on the power station parameters (the physical proprieties of the water and the ambient, the suction head and the head of the turbine) while the turbine cavitation coefficient  $\sigma_T$  depends on the turbine geometry and its kinematics and dynamics conditions. Moreover, the turbine and plant cavitation coefficients have different physical meanings, and they are numerically equal only at the inception of cavitation, Anton (1985). To predict – or better to avoid – cavitation is therefore one of the main goals when designing hydraulic machines. As a result, the evaluation of the cavitation performance for the Francis turbines involves computing the turbine cavitation coefficient for variable discharge. Therefore, we defined and developed a numerical methodology for computing the **turbine cavitation coefficient**.

The IEC standards defines the *plant cavitation coefficient*  $(\sigma_{pl})_x$  or *Thoma number*:

$$\sigma_{pl} = \frac{p_{at} - p_{va} \pm \rho g H_s}{\rho g H} = \frac{A - A_t \pm H_s}{H}$$

where  $p_{at}$  corresponds to the atmospheric pressure,  $p_{va}$  vapour pressure,  $p_{min}$  minimum pressure,  $H_s$  suction head, and  $H$  turbine head.

The presence of cavitation inside the turbine can be evaluated by computing the *reserve cavitation coefficient*  $(\sigma_{rez})_x$ :

$$\sigma_{rez} = \frac{p_{min} - p_{va}}{\rho E} = \sigma_{pl} - \sigma_T$$

where  $p_{min}$  is the minimum pressure value inside the machine and  $\sigma_T$  is turbine cavitation coefficient. Cavitation development occurs in all the zones where the local pressure is equal or less than the vapour pressure. Therefore, the reserve cavitation coefficient allows to detect the incipient cavitation points as well as the cavitation and supercavitation regimes, as follows:

$p_{min} > p_{va}$	$\sigma_{rez} > 0$	$\sigma_T < \sigma_{pl}$	<b>without cavitation</b>
$p_{min} = p_{va}$	$\sigma_{rez} = 0$	$\sigma_T = \sigma_{pl}$	<b>incipient of cavitation</b>
$p_{min} < p_{va}$	$\sigma_{rez} < 0$	$\sigma_T > \sigma_{pl}$	<b>cavitation</b>
$p_{min} \ll p_{va}$	$\sigma_{rez} \ll 0$	$\sigma_T \gg \sigma_{pl}$	<b>super-cavitation</b>

Replacing the Thoma number into the reserve cavitation coefficient we compute the turbine cavitation coefficient:

$$\sigma_T = -\left(c_{p\ min}^*\right) + \eta_{ta} \left(c_{ref}^*\right)^2 - \frac{g \cdot (z_r - z_{ref})}{E}$$

where the following notations are used:

- $c_{p\ min}^*$  is the minimum pressure coefficient relative to the turbine specific energy  $E$ ,

$$\left(c_{p\ min}^*\right) = \frac{p_{min} - p_{ref}}{\rho E}$$

For numerical simulation we defined and computed the minimum pressure coefficient

$$\left(c_{p\ min}\right) = \frac{p_{min} - p_{ref}}{\rho E_{ref}}$$
 relative to the energy between distributor inlet and draft tube inlet

sections  $E_{ref}$ . Therefore, the relationship between two minimum pressure coefficients is obviously

$$\left(c_{p\ min}^*\right) = \left(c_{p\ min}\right) \frac{E_{ref}}{E}$$

The  $p_{ref}$  value corresponds to the static pressure on the draft tube wall. We obtain the reference pressure from experimental data employed at LMH-EPFL, Kubota et al. (1996) as follows:

$$\begin{aligned} (p_{ref})_x &= p_{\bar{i}} + \rho g(z_{ref} - z_{\bar{i}}) + \frac{\rho}{2} \frac{Q_x^2}{S_{ref}^2} \left[ \left( \frac{S_{ref}}{S_{\bar{i}}} \right)^2 - 1 \right] + (\zeta_D)_x \frac{\rho}{2} \left( \frac{Q_x}{S_{ref}} \right)^2 = \\ &= p_{\bar{i}} + \rho g(z_{ref} - z_{\bar{i}}) - \eta_{ta} \frac{\rho}{2} \frac{Q_x^2}{S_{ref}^2} \end{aligned}$$



where  $p_I$  corresponds to the static pressure at the outlet of the draft tube,  $z_{ref} - z_I$  the inlet/outlet level difference for the draft tube,  $Q$  the discharge of the current operating point,  $\rho$  the density of the water,  $R_{ref}$  and  $S_{ref}$  the radius and area, respectively, for the reference section (the draft tube inlet section),  $S_I/S_{ref} = 3.23$  the area ratio of the outlet and reference sections,  $\omega$  angular velocity and  $(\zeta_D)_x$  the draft tube energy losses coefficient from Kubota et al. (1996) (Figure 68).

- $c_{ref}^*$  is the normalized absolute velocity,

$$c_{ref}^* = \frac{V_{ref}}{\sqrt{2E}}$$

conventionally, the average velocity (discharge / draft tube inlet area) is considered

$$c_{ref}^* = \frac{V_{ref}}{\sqrt{2E}} = \frac{1}{\sqrt{2E}} \cdot \frac{Q}{S_{ref}} = \frac{1}{\sqrt{2E}} \cdot \frac{Q}{\pi R_{ref}^2}$$

- $\eta_{ta}$  is defined to be the draft tube efficiency which takes in account the draft tube hydraulic losses coefficient and the ratio of the inlet and the outlet velocity Anton (1985), Anton (2001),

$$\eta_{ta} = 1 - \left( \frac{V_{ref}}{V_I} \right)^2 - \zeta_D = 1 - \left( \frac{S_I}{S_{ref}} \right)^2 - \zeta_D.$$

Anton defines the turbine cavitation coefficient Anton (1964), Anton (1985) using velocity coefficients, by using the Bernoulli equation.

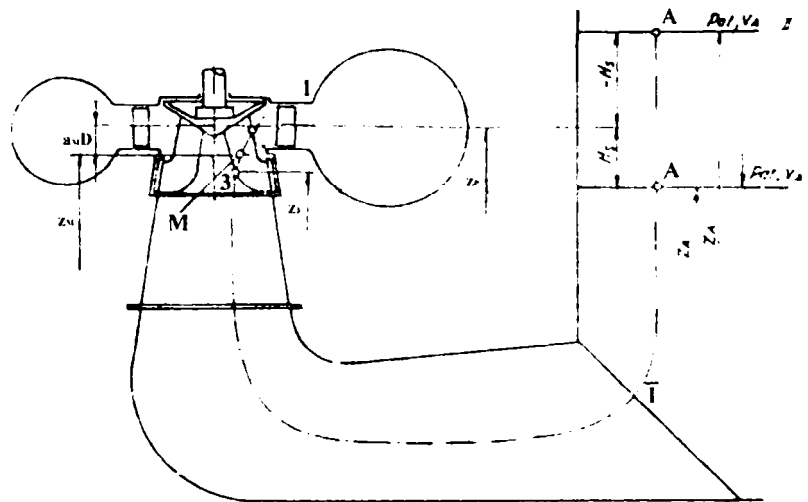


Figure 70 Notations for the Francis turbine sections, Anton (1985).

According to Figure 70, he first uses the Bernoulli equation for relative flow ( $M \rightarrow 3$ )

$$\frac{p_M}{\gamma} + \frac{W_M^2 - U_M^2}{2g} + z_M = \frac{p_3}{\gamma} + \frac{W_3^2 - U_3^2}{2g} + z_3 + hp_{M3}$$

then he uses the Bernoulli equation for absolute flow ( $3 \rightarrow A$ )

$$\frac{p_3}{\gamma} + \frac{V_3^2}{2g} + z_3 = \frac{p_A}{\gamma} + \frac{V_A^2}{2g} + z_A + hp_{3A},$$

The indices correspond to:  $3$  the runner blade outlet,  $M$  point belongs to the three-dimensional interblade channel of the runner and  $A$  to the tailrace section.

According to Anton, the turbine cavitation coefficient will have the expression,

$$\sigma_T = \frac{W_{max}^2 - W_3^2}{2gH} - \frac{U_M^2 - U_3^2}{2gH} + \frac{V_3^2 - V_A^2}{2gH} - \frac{hp_{M3}}{H} - \frac{hp_{3A}}{H} + \frac{a_M D}{H}$$

where  $W$  correspond to the relative velocity,  $V$  absolute velocity,  $U$  transport velocity,  $H$  head of the turbine,  $p$  static pressure,  $hp$  hydraulic losses between the specified points and  $a_M D$  is the distance indicated in Figure 70.

The above formula is then written using the dimensionless velocity coefficients,

$$c_3^* = \frac{V_3}{\sqrt{2E}}, u_3^* = \frac{U_3}{\sqrt{2E}} = \frac{\omega R_3}{\sqrt{2E}}, cw_3^* = \frac{W_3}{\sqrt{2E}}$$

and

$$kp_{\max 3} = \left[ \left( \frac{W_{\max}}{W_3} \right)^2 - 1 \right], ku_M = \left[ \left( \frac{U_M}{U_3} \right)^2 - 1 \right],$$

to obtain

$$\sigma_T = kp_{\max 3} (cw_3^*)^2 - ku_M (u_3^*)^2 + (c_3^*)^2 - (c_A^*)^2 - \frac{hp_{M3}}{H} - \frac{hp_{3A}}{H} + \frac{a_M D}{H}.$$

Here  $kp_{\max 3}$  is the dimensionless maximum velocity coefficient and  $ku_M$  is the dimensionless transport velocity coefficient at M. Next, by assuming that the hydraulic losses  $hp_{M3}$  are negligible, Anton (1985), and the draft tube losses can be written by using the draft tube efficiency  $\eta_{ta}$ , the following formula is obtained:

$$\sigma_T = kp_{\max 3} (cw_3^*)^2 - ku_M (u_3^*)^2 + \eta_{ta} (c_3^*)^2 + \frac{a_M D}{H}$$

One can easily recognize that this velocity coefficient formulation is equivalent to the following pressure formulation

$$\sigma_T = -(c_{p,\min})^* + \eta_{ta} (c_3^*)^2 - \frac{(z_r - z_3)}{H},$$

thus in order to compare numerical results obtained with both formulations for the turbine cavitation coefficient we have used in this work the point 3 to correspond to the reference section.

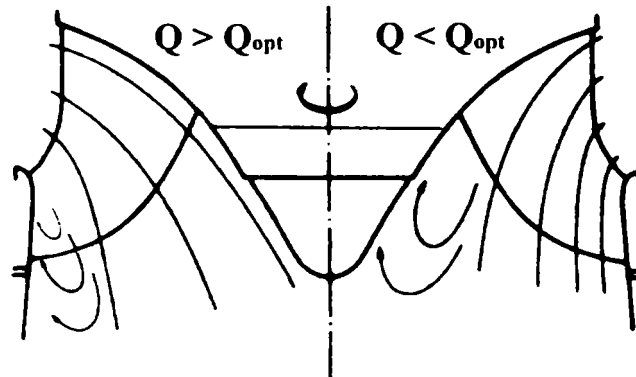


Figure 71 Generation the secondary flow in a Francis turbine at the overload ( $Q > Q_{opt}$ ) (left) and partial points ( $Q < Q_{opt}$ ) (right).

The velocity coefficients formulation of the turbine cavitation coefficient is correct as long as one can identify a relative flow streamline along which the relative flow Bernoulli equation is valid. However, as shown in Figure 71 for some turbine operating points the minimum pressure is present within a recirculation region, i.e. within a region with closed streamline. In this case, one cannot relate via the Bernoulli equation the minimum pressure point with a point downstream.

Figure 72 presents the turbine cavitation coefficient computed with minimum pressure coefficient (triangles), and using the velocity coefficients (squares), respectively. For discharge smaller than the optimum value, the two formulae give approximately the same numerical values, while for larger discharge (when recirculation occurs on the runner blade), the results are quite different. In order to do justice among the two formulae for the turbine cavitation coefficient, we also plot in Figure 72 the experimental plant cavitation coefficient measured by visually observing the cavitation onset. At cavitation inception, the turbine cavitation coefficient should be numerically equal to the plant cavitation coefficient.

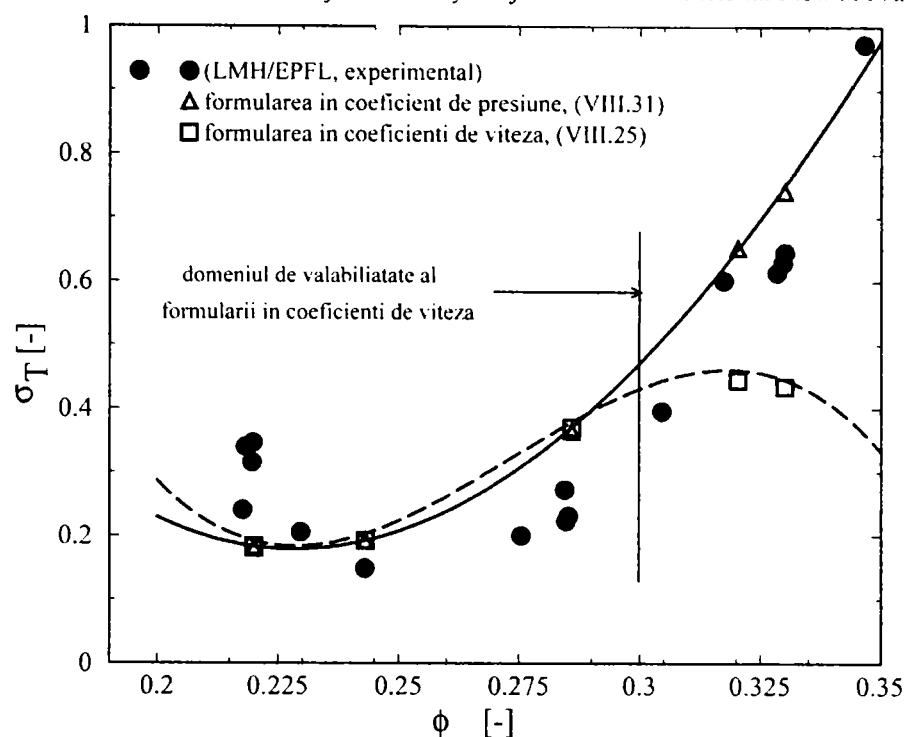


Figure 72 Turbine cavitation coefficient  $(\sigma_T)_x$  versus discharge coefficient  $(\phi)$  at constant guide vane opening ( $\alpha \approx 25^\circ$ ) for GAMM Francis runner. Comparison between the experimental data from (LMH/EPFL ●) and numerical results (Muntean  $\Delta$  with pressure coefficient formulation,  $\square$  with velocities coefficients formulation).

In conclusion, Figure 72 shows that the pressure formulation for the turbine cavitation coefficient is in good agreement with experimental data for the whole discharge interval under investigation, while the velocity formulation for the turbine cavitation coefficient is valid mainly for discharge smaller than the optimum value. However, the velocity coefficient formulation is useful for tackling the issue of scale effects, Anton (1999).

Finally, the qualitative comparison between numerical visualization of the cavitation region (Figure 73) and the photography of the experimental visualization (Figure 74) at best efficiency point and  $\sigma_{pi}=0.2$  is presented. Because a single-phase model was used in computations, Figure 73 presents the region with static pressure under the absolute vapour pressure of the water. It can be seen that the cavitation region appears on the suction side of the Francis runner blade, in the neighbourhood of the leading edge and near to the band. The light green spot indicates the lowest pressure. Actually, in the same region the cavitation bubbles are developed and migrate due to the water flow.

In conclusion, this chapter presents a numerical methodology for computing the global parameters of the Francis turbine (i.e. runner torque coefficient, turbine efficiency and turbine cavitation coefficient) for the whole range of operating conditions. Based on the three-dimensional numerical results obtained at best efficiency point and off-design operating points (Chapter VII) we compute the Francis runner torque coefficient for various discharge  $c_M=f(\phi)$ . Conventionally, we defined a special efficiency which does not take into account the extra kinetic energy due to the swirl and axial velocity non-uniformity on the draft tube inlet section. Energetically, a good agreement between our runner torque coefficient and experimental data is obtained as long as the theoretical efficiency is well predicted around the best efficiency point and reasonable to the rest. For the cavitation performance we used the pressure distribution on the Francis runner blade obtained with coupled technique from Chapter VII in conjunction with the reference pressure. The reference pressure is computed from experimental data, Kubota et al. (1996). Therefore, the turbine cavitation coefficient  $\sigma_T=f(\phi)$  is obtained. As a result, it is established the validity domain of the cavitation coefficient in the velocities coefficients formulation derived by Anton (1964) as well as a new cavitation coefficient formula is developed. This new formulation, called “*pressure coefficient formulation of the cavitation coefficient*” is validated by numerical data against experiments for whole range of operating conditions. The pressure coefficient formulation of the cavitation coefficient opens the new perspectives towards computing the cavitation scale effect for whole range of operating conditions.

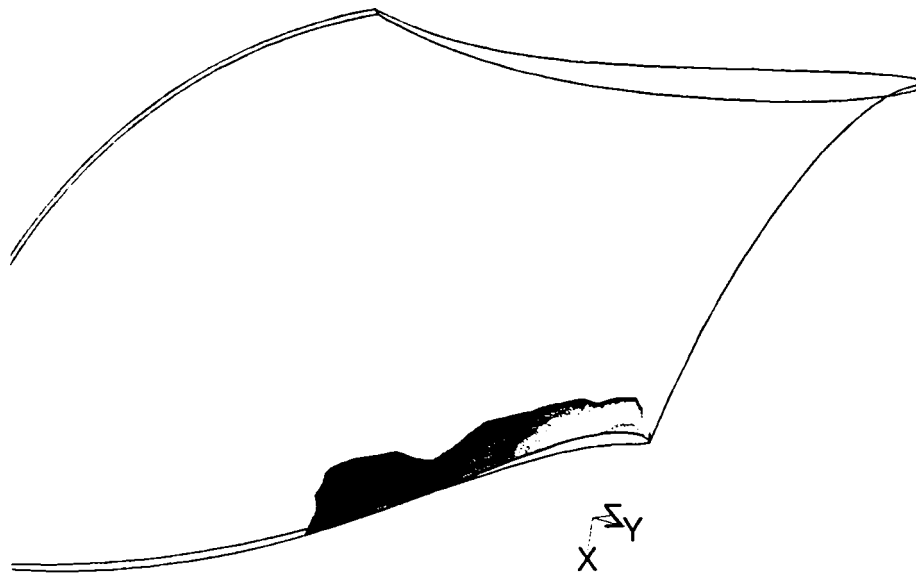


Figure 73 Computed cavitation zone ( $p < p_{va}$ ) development for GAMM Francis turbine at the best efficiency operating point and  $\sigma_{pl}=0.2$ .



Figure 74 Photography of the inlet edge cavitation development for GAMM Francis turbine at the best efficiency operating point and  $\sigma_{pl}=0.2$ , Avellan et al. (1993).

## 9. Conclusions

The main topic of this work is the computation the energetic and cavitation performances of the Francis turbine for the whole range operating conditions. This goal was achieved by developing numerical methodologies and applying them for the Francis turbine. These numerical methodologies were validated against available experimental data.

The **second** chapter contains fundamental concepts and development of computational schemes for computing the fluid flow in hydraulic machines. This theoretical background supports the work developed in the following chapters.

Chapter **three** presents the GAMM Francis turbine model, designed at the *Institut de Machines Hydrauliques et de Mécanique des Fluides* (IMHEF) at the *École Polytechnique Fédérale de Lausanne* (EPFL). The test model corresponds to a Francis turbine of medium/high specific speed  $v=0.5$  ( $n_q=76$ ). The model was used as a test case back in 1989 GAMM Workshop, where all the geometrical information, including stay vanes, guide vanes, runner and draft tube, and measurements for the best efficiency operating point were available. The runner was also used as a test case in the annual ERCOFTAC Seminar and Workshop on Turbomachinery Flow Predictions. Flow surveys were conducted at both inlet and outlet sections of the runner for various operating conditions, as well as on the distributor inlet section and draft tube inlet section. Pressure transducers installed on both pressure and suction sides of the runner blades provide the pressure distribution on the blade. Flow measurements were obtained with a 5-hole pressure probe. Runner static pressure was measured at three different blade sections. These experimental data are used in the following chapters for comparison with our numerical results, Avellan et al. (1990), Avellan et al. (1993).

In chapter **four** a methodology for computing the three-dimensional inviscid, incompressible flow in the Francis turbine distributor corresponding to the best efficiency operating point was presented. The computational domain corresponds to the actual turbine geometry. The investigation is focused on the inflow/outflow boundary conditions of the distributor. Three sets of boundary conditions were considered in computations. The best results are obtained for the uniform velocity profile imposed on the distributor inlet section and measured pressure distribution on the distributor outlet section. As a result, even when the flow is considered inviscid, the computed velocity and pressure fields agree reasonable well with experimental data.

In the **fifth** chapter a methodology for computing the three-dimensional inviscid, incompressible flow in the Francis turbine runner at the best efficiency operating point was developed. The computational domain corresponds to the actual turbine geometry. A methodology was developed for generating the 3D GAMM Francis runner computational domain. The complicated shape of the runner computational domain was generated using an original and efficient technique together with its unstructured meshes. Next, the investigation is focused on the inflow/outflow boundary conditions. Three sets of boundary conditions were considered in computations. In comparison with experiments, the best results are obtained for the corrected velocity profile to ensure the measured discharge imposed on the distributor inlet section in conjunction with a new boundary condition on the draft tube inlet section called *radial equilibrium condition*. Based on the actual velocity field on the draft tube conical section we introduce the radial equilibrium condition. This new boundary condition eliminates the spurious recirculation which is numerically generated after the flow leaves the runner blades when pressure distribution is prescribed on the draft tube inlet section. Moreover, imposing this boundary condition on the draft tube inlet section will eliminate the need for experimental data and opens new perspectives for simulating off-design operating points.

After computing the velocity and pressure fields in the Francis turbine runner we evaluate the runner torque coefficient. Our value is only 0.14% smaller than the experimental value, thus demonstrating the ability of this methodology to predict the turbine performances. As a result, the method developed in this chapter is a reliable and efficient design and/or optimization tool for the Francis turbine runner at the best efficiency operating point.



In chapter **six** a numerical analysis of the three-dimensional distributor flow for variable discharge was performed. Based on the numerical results, an original numerical methodology for optimizing the guide vane axis position for the whole range of the guide vane openings and constant energy was developed. This numerical methodology is based on an original hydrodynamic equivalence criterion, and is exemplified for the GAMM distributor. As a result, the minimum guide vane torque is obtained. The methodology can be employed for the current engineering design and optimization of the guide vane regulating apparatus in order to minimize the mechanical loading requirements for all machine parts used to move the guide vanes (guide vane servomotors, regulating ring and guide vane linkage).

In the **seventh** chapter a methodology for computing the three-dimensional flow through the Francis turbine runner at variable operating points was presented. Due to the lack of the boundary conditions on the runner inlet section and the current limitations in computer hardware the 3D flow computation is performed in two domains, corresponding to the distributor and runner channels. Consequently, a distributor-runner flow coupling technique based on *mixing interface method* is developed. On the domains interface, a special technique is employed to eliminate the circumferential variation in both velocity and pressure fields, thus the name of the method. The iterative coupling technique takes successively the distributor outlet velocity as inflow condition for the runner, and the computed runner inlet pressure as outlet pressure condition for the distributor. The stopping criterion is chosen for the pressure on the mixing interface.

The main advantage when computing the flow through the distributor-runner turbine is that only the velocity distribution at the distributor inlet (usually taken as a constant velocity profile corresponding to the spiral case outlet) needs to be known. This is particularly important for practical engineering applications since no velocity and/or pressure measurements are usually performed for turbine models.

The radial equilibrium condition employed at the runner outlet /draft tube inlet section is found to be the best choice in order to avoid spurious back flow after the runner. In addition, this condition performs very well for variable discharge, being able to deal with recirculation flows as well.

Extensive comparison of our numerical results with experimental data is performed, in order to validate and assess the accuracy of the numerical method, Avellan et al. (1990). As a first conclusion, it seems that the inviscid flow model is suitable for computing the 3D hydraulic turbine flow at and around the best efficiency operating point. Comparison with velocity and pressure profiles on the four surveys axes show an excellent agreement of the coupled computations with experiments. On the other hand, computing separately the flow in the distributor / runner not only requires experimental data which are not currently available but also lead to poor predictions especially after the runner blades and at the draft tube inlet.

In the **last** chapter a numerical methodology for computing the global parameters of the Francis runner (i.e. torque coefficient, hydraulic efficiency, turbine cavitation coefficient) for whole range of the operating conditions was developed. Based on the three-dimensional numerical results obtained at best efficiency point and off-design operating points (Chapter VII) we compute the Francis runner torque coefficient for various discharge  $c_M=f(\phi)$ . Conventionally, we defined a special efficiency which does not take into account the extra kinetic energy due to the swirl and axial velocity non-uniformity. Energetically, a good agreement between our runner torque coefficient and experimental data is obtained as long as the theoretical efficiency is good predicted around the best efficiency point and reasonable to the rest. Cavitationally, the turbine cavitation coefficient  $\sigma_T=f(\phi)$  is defined and computed. As a result, it is established the validity domain of the cavitation coefficient in the velocities coefficients formulation developed by Anton (1964) and a new cavitation coefficient formula is given. This new formulation, called "*pressure coefficient formulation of the cavitation coefficient*" is validated by numerical data against experiments employed from LMH-EPFL by Kubota et al. (1996) for whole range of operating conditions. The pressure coefficient formulation of the cavitation coefficient opens the new perspectives towards computing the cavitation scale effect for whole range of operating conditions.

We can firmly state that the numerical methodologies developed in this work are a reliable and efficient way to compute 3D turbomachinery performances. It can be easily employed for design and optimization investigation, even that a 3D inviscid flow solver (e.g. the FLUENT commercial CFD code) is used.

## 10. Bibliography

(Partial)

1. Anton I., *Curbe caracteristice de cavitație la pompele centrifuge cu turație specifică joasă*, Institutul Politehnic "Traian Vuia" Timișoara, PhD Thesis, 1961.
2. Anton I., *Curbe caracteristice de cavitație la mașinile hidraulice (turbine și pompe)*, Conferința de Mașini Hidraulice, Timișoara, 1964.
3. Anton I., *Turbine Hidraulice*, Ed. Facla, Timișoara, 1979.
4. Anton I., *Cavitația*, Editura Academiei R.S.R., București, Vol. I, 1984.
5. Anton I., *Cavitația*, Editura Academiei R.S.R., București, Vol. II, 1985.
6. Anton I., Campian V., și Carte I., *Hidrodinamica Turbinelor Bulb și a Turbinelor - Pompe Bulb*, Editura Tehnică, București, 1988.
7. Anton I. (eds.), *Conferința de Mașini Hidraulice și Hidrodinamică*, Timișoara, Romania, Octombrie 18-19, 1985.
8. Anton I., Popoviciu M., Fitero I., Preda I., Bărglăzan M., (eds.), *Conferința de Mașini Hidraulice și Hidrodinamică*, Timișoara, Romania, November 15-17, 1990.
9. Anton I., Popoviciu M., Ancușa V., Bărglăzan M., (eds.), *Proceedings of the 4<sup>th</sup> Conference on Hydraulic Machinery and Hydrodynamics*, Timișoara, România, September 26-30, 1994.
10. Anton I.M., *Efectele de scară energetice și cavitaționale la turbinele Francis și Kaplan*, Buletinul Științific al Universității "Politehnica" din Timișoara, Tom 44(58), seria Mecanica, 7-36, 1999.
11. Anton I.M., *Stadiul aplicării metodelor CFD la calculul randamentului difuzorului turbinelor Francis și Kaplan*, Zilele Academice Timișene, 2001. (în curs de apariție)
12. Avellan F., Dupont P., Farhat M., Gindroz B., Henry P., Hussain M., Parkinson E., Santal O., *Flow survey and blade pressure measurements in a Francis turbine model*. Proceedings of the XV IAHR Symposium, Belgrade, Yugoslavia, Vol. 2, I5, pp. 1-14, 1990.
13. Avellan F., Dupont P., Farhat M., Gindroz B., Henry P., Hussain M., *Experimental flow study of the GAMM turbine model*. In Sottas G. and Ryhming I.L., (eds.), *3D-computation of incompressible internal flows*, NNFM 39, pp. 33-53, Vieweg Verlag, Braunschweig, 1993.
14. Billdal J.T., Jacobsen Ø., Bratsberg K., Andersson H.I., Brekke H., *Numerical Inviscid Flow Analysis of the GAMM Francis Runner*. In Sottas G. and Ryhming I.L., (eds.), *3D-computation of incompressible internal flows*, NNFM 39, pp. 71-76, Vieweg Verlag, Braunschweig, 1993.
15. Borresen B. Jr., *Development and Validation of a Sub-Domain Method for the Calculation of Incompressible Three-Dimensional Flow: Application to Hydraulic Turbomachines*, École Polytechnique Fédérale de Lausanne, Elveția, PhD. Thesis, 1995.
16. Bottaro A., Drotz A., Gamba P., Sottas G., Neury C., *Euler Simulation of Flow in a Francis Distributor and Runner*. In Sottas G. and Ryhming I.L., (eds.), *3D-computation of incompressible internal flows*, NNFM 39, pp. 77-84, Vieweg Verlag, Braunschweig, 1993.
17. Chorin A.J., *A numerical methods for solving incompressible flow problems*, Journal of Computational Physics, 2:12-26, 1967.
18. Cobut D., Marx Y.P., Reymond J.-D., Salwey M.L., Bellet L., *A numerical study of the flow in a Francis turbine runner at off-design operating conditions*, Internal Report IMHEF T-96-14, École Polytechnique Fédérale de Lausanne, Suisse, 1996.
19. Eliasson P., *Numerical Solution of the Incompressible Euler Equations in a Water Turbine*. In Sottas G. and Ryhming I.L., (eds.), *3D-computation of incompressible internal flows*, NNFM 39, pp. 85-92, Vieweg Verlag, Braunschweig, 1993.
20. Ferziger J.H., Peric M., *Computational Methods for Fluid Dynamics*, Springer Verlag Berlin-Heidelberg-New York, 1996.
21. Fletcher C.A.J., *Computational Tehniques for Fluid Dynamics (Second Edition)*, Vol. I + II, Springer - Verlag, 1991.

22. Goede E., *A Stacking Technique for Multistage 3D Flow Computation in Hydraulic Turbomachinery*. In Sottas G. and Ryhming I.L., (eds.), *3D-computation of incompressible internal flows*, NNFM 39, Vieweg Verlag, Braunschweig, 93-100, 1993.
23. Grimbert I., Verry A., El Ghazzani E.M., *3D Euler Computation of the Flow inside the GAMM Francis Runner*. In Sottas G. and Ryhming I.L., (eds.), *3D-computation of incompressible internal flows*, NNFM 39, pp. 101-108, Vieweg Verlag, Braunschweig, 1993.
24. Gros L., Kueny J.-L., Avellan F., Bellet L., *Numerical Flow Analysis of the GAMM Turbine at Nominal and Off-Design Operating Conditions*. Proceedings of the XIX IAHR Symposium, Singapore, Republic of Singapore, vol. 1, pp. 121-128, 9-11 Sept. 1998.
25. Hirsch C., *Numerical Computation of Internal and External Flows*, vol. I + II, John Wiley & Sons Ltd., Chichester-New York-Brisbane-Toronto-Singapore, 1988.
26. Kovalev N.N., *Ghidroturbini*, Moskwa, 1961.
27. Kubota T., Han F., Avellan F., *Performance Analysis of Draft Tube for GAMM Francis Turbine* In Cabrera E. et al., (eds.), *Proceedings of XVIII IAHR Symposium on Hydraulic Machinery and Cavitation*, Valencia, Spain, September 16-19, pp. 130-139, Kluwer Academic Publishers, 1996.
28. Muntean S., Susan-Resiga R., Anton I., *Numerical Analysis of Cascade Flow. Part II: Finite Volume Analysis of the Viscous Flow*, 5<sup>th</sup> International Conference on Hydraulic Machinery and Hydrodynamics, Timisoara, 97-104, 2000.
29. Nagafuji T., Suzuki T., Kobayashi T., Taniguchi N., *3D Flow Analysis in the Runner and the Distributor of Francis Turbines*. In Sottas G. and Ryhming I.L., (eds.), *3D-computation of incompressible internal flows*, NNFM 39, pp. 135-142, Vieweg Verlag, Braunschweig, 1993.
30. Parkinson E., *Test Case 8: Francis Turbine*, Turbomachinery Workshop ERCOFTAC II, 1995.  
[http://lmhwww.epfl.ch/Research/EVA/Gamm\\_files/Gamm.pdf](http://lmhwww.epfl.ch/Research/EVA/Gamm_files/Gamm.pdf)
31. Patankar S.V., *Numerical Heat Transfer and Fluid Flow*, Hemisphere, Washington, D.C., 1980.
32. Peric M., *Finite Volume Method for Computation of Fluid Flow in Complex Geometries*, Ph.D. thesis, University of London, UK, 1985.
33. Sottas G., Ryhming I.L. (eds.), *3D - Computation of Incompressible Internal Flows*, Proceedings of the GAMM Workshop, Notes Numerical Fluid Mechanics (NNFM) 39, Vieweg Verlag, Braunschweig, 1993.
34. Susan-Resiga R., Muntean S., Anton I., *Analiza numerica a curgerii cu desprinderi în retele plane de profile*, Grant GAR Nr. 156, Contract No. 120/1999.
35. Susan-Resiga R., Muntean S., *Periodic boundary conditions implementation for the Finite Element Analysis of the cascade flows*, Buletinul Stiintific al Universitatii "Politehnica" din Timisoara, Tom 44(58), seria Mecanica, 151-160, 1999.
36. Susan-Resiga R., Muntean S., *Analiza numerică a curgerii în distribuitorul turbinelor hidraulice*, Prima Conferință a Hidroenergeticienilor din România, București, 2000, p. 469-478.
37. Susan-Resiga R., Muntean S., Anton I., *Numerical Analysis of Cascade Flow. Part I: Finite Element Analysis of the Inviscid Flow*, 5<sup>th</sup> International Conference on Hydraulic Machinery and Hydrodynamics, Timisoara, 159-166, 2000.
38. Susan-Resiga R., Muntean S., Anton I., *Analiza numerica a curgerii în retele radiale dispuse în tandem*, Grant ANSTI-C Nr. 4161, 2000.
39. Reymond J.-D., *Some experiments with an osculatory scheme for generation of structured grids*, Internal Report IMHEF T-92-6, École Polytechnique Fédérale de Lausanne, Suisse, 1992.
40. Reymond J.-D., *A Strategy for Grid Generation and HAMAC User Intoduction Guide (Release 3.5)*, Internal Report IMHEF - EPFL, Lausanne, Suisse, 1995.
41. Rizzi A., Eriksson L.-E., *Computation of flow around wings based on the Euler equations*, Journal of Fluid Mechanics, Vol 148, pp. 45-71, 1984.
42. Rizzi A., Eriksson L.-E., *Computation of inviscid incompressible flow with rotation*, Journal of Fluid Mechanics, Vol 153, pp. 275-312, 1985.
43. Soni B.K., *Two- and Three-Dimensional Grid Generation for Internal flow Applications of Computational Fluid Dynamics*, AIAA Paper 85-1526, 1985.
44. Soni B.K., *Grid Generation for Internal Flow Configurations*, Computer & Mathematics with Applications, vol. 24, no. 5/6, pp. 191-201, September 1992.
45. Soni B.K., *Grid Generation: Overview, Strategies and Algorithms*, National Science Foundation Engineering Research Center, Mississippi State University, USA, 1995.
46. Sorenson R.L., *The 3DGRAPE Book: Theory, User's Manual, Examples*, NASA TM-102224, 1989.
47. Steinbrenner J.P., Chawner J.R., Fouts C.L., *Multiple Block Grid Generation in the Interactive Environment*, AIAA Paper 90-1602, 1990.



48. Thompson J.F., *Numerical Grid Generation: Foundations and Applications*, North-Holland, New-York, 1985.
49. Thompson J.F., *A Reflection on Grid Generation in the 90s: Trends, Needs and Influences*, 5<sup>th</sup> International Conference on Numerical Grid Generation in Computational Field Simulation, Mississippi State University, pp. 1029-1110, 1996.
50. Van Doormaal J.P., Raithby G.D, *Enhancement of the SIMPLE Method for Predicting Incompressible Fluid Flow*, Numerical Heat Transfer, Vol 7, pp. 147-163, 1984.
51. Vavra M.H., *Aero - Thermodynamics and Flow in Turbomachines*, John Wiley & Sons Inc., London, New York, 1960.
52. Weatherill N.P., *Introduction and Overview of Grid Generation*, COSMASE course, IMHEF - EPFL, Lausanne, Suisse, 1996.
53. Wu C.-H., *A General Theory of Three - Dimensional Flow in Supersonic Turbomachines of Axial, Radial, and Mixed - Flow Types*, Transactions of the ASME, 1952.
54. Wu C.-H., *A Theory of the Direct and Inverse Problems of Compressible Flow Past Cascade of Arbitrary Blade Sections Lying in Arbitrary Stream Filament of Revolution in Turbomachine*, Scientia Sinica, Vol. III, Nr. 12, 1959.
55. \*\*\*, *FLUENT 5. User's Guide*, Fluent Incorporated, 1998.
56. \*\*\*, *Gambit 1. User's Guide*, Fluent Incorporated, 1998.



# Curriculum Vitae

## PERSONAL DETAILS

Family name: Muntean  
First names: Sebastian  
Date of birth: September 15, 1970  
Place of birth: Vadu-Crisului, Bihor, Romania  
Nationality: Romanian  
Address: Str. Moldovei, Nr. 86, Bl. PC-24, ap. 3  
3700 Oradea, Romania  
Telephone: +40-56-221547  
Fax: +40-56-221547  
E-mail: seby@acad-tim.utt.ro

## EDUCATION

1994 – 1995 M.Sc.  
“Politehnica” University of Timisoara  
Mechanical Engineering Faculty  
Department of Hydraulic Machinery  
1989 – 1994 B.Sc.  
“Politehnica” University of Timisoara  
Mechanical Engineering Faculty  
Department of Hydraulic Machinery  
1984 – 1988 “Emanuil Gojdu” High School Oradea, Romania

## POSTGRADUATE EDUCATION

October 31 – November 2, 2001 Tensor Srl., Engineering Software,  
Bucuresti, Romania  
**GAMBIT & FIDAP Training Courses**  
January 25 – 26, 1999 Enervac – Flutec Ltd., Software & Services for Design and  
Development, Thessaloniki, Greece  
**GAMBIT & FLUENT Training Courses**  
September 23 – 27, 1996 École Polytechnique Fédérale de Lausanne (EPFL),  
Lausanne, Switzerland  
*Computation in Sciences Methods and Algorithms on  
Supercomputing for Engineering (COSMASE):  
Grid Generation and Parallel Computing*

## PROFESSIONAL EXPERIENCE

2000 – *Senior Researcher*  
Romanian Academy – Timisoara Branch  
Center of Advanced Research in Engineering Sciences  
Laboratory of Numerical Simulation and Parallel  
Computing for Fluid Mechanics  
1997 – *Senior Researcher*  
Romanian Academy – Timisoara Branch  
Center of Advanced Research in Engineering Sciences  
Laboratory of Hydraulic Machinery  
1996 – 1997 *Researcher*  
Romanian Academy – Timisoara Branch  
Center of Advanced Research in Engineering Sciences  
Laboratory of Hydraulic Machinery  
1994 – 1996 *Assistant Researcher*  
Romanian Academy – Timisoara Branch  
Center of Advanced Research in Engineering Sciences  
Laboratory of Hydraulic Machinery